ЕЛЕКТРОЕНЕРГЕТИКА
/
POWER ENGINEERING

(EE/EEI)

Metod za inženjersku procenu proizvodnje vetroelektrane

Vladimir A. Katić, *Senior Member, IEEE*

***Abstrakt* — U ovom radu je razmatrana mogućnost brzog i jednostavnog procenjivanja proizvodnje električne energije planirane vetroelektrane na osnovu korišćenja raspoloživih podataka. Pošlo se od pretpostavke da su raspoložive usrednjene godišnje vrednosti brzine i gustine snage energije vetra. Razmatranjem različitih opcija za procenjivanje proizvodnje, predložena je jedna metoda. Radi verifikacije ona je primenjena za jednu lokaciju i četiri vrste vetrogeneratora. Metoda je verifikovana poređenjem sa izračunatom energijom na bazi stvarnih rezultata merenja brzine vetra. Postignuta je zadovoljavajuća tačnost pogodna za inženjerske procene, čime je metoda opravdala mogućnost primene.**

***Ključne reči* — Vetroenergija, Vetroelektrane, Metod procene proizvodnje.**

I. UVOD

Primena obnovljivih izvora energije danas je prihvaćena kao jedno od rešenja za zamenu fosilnih goriva, čije rezerve se ubrzano iscrpljuju. Istovremeno, time se omogućuje smanjenje emisije CO_2 i drugih gasova staklene bašte, za koje je pokazano da doprinose povećanju prosečne temperature na Zemlji i time dovode do klimatskih promena [1].

Za generisanje električne energije iz obnovljivih izvora najčešće se koriste energije vetra, vode, sunca, biomase i geotermalna. Trenutno su u svetu najveći instalisani kapaciteti u vetroelektranama sa dobrim perspektivama rasta. Na sl. 1 prikazana je struktura primene obnovljivih izvora prema planu za 2050. god., gde se vidi da će najveći deo obnovljivih izvora biti angažovan za dobijanje električne energije (58%), od čega 41% (ili 24% od ukupnog) će činiti vetroelektrane [2].

U Srbiji je utvrđen značajan potencijal za korišćenje energije vetra i već su izgrađene ili su u izgradnji vetroelektrane ukupne snage od 566 MW [3,4]. Strategijom razvoja energetike Srbije predviđeno je da se u narednom periodu (do 2030. god.) izgradi ukupno 600 MW, ali su procenjeni potencijali znatno veći (1300 MW, pa i više) [4,5]. To ukazuje na potrebu da se kontinuirano istražuju adekvatne lokacije i mogućnosti izgradnje novih vetroelektrana.

Jedan od prvih preduslova za određivanje pogodne lokacije je poznavanje energetskog potencijala. Ovaj potencijal se određuje preko brzine vetra i gustine snage vetra u određenoj oblasti ili na mikrolokaciji. U svetu je poznat veliki broj studija, naučnih radova i drugih publikacija na ovu temu. Pored toga postoji i veći broj web-sajtova, preko kojih se može dobiti procena vetro-energetskog potencijala, a jedan od takvih je i „Global Wind Atlas“ (https://globalwindatlas.info/) [6]. U Srbiji je rađeno nekoliko studija, a jedan od primera je i studija „Atlas vetrova AP Vojvodine“ [3].

Međutim, problem je što su u tim publikacijama ili na sajtovima date uprosečene godišnje vrednosti brzine i gustine energije vetra. Razlog za to je velika promenljivost energije vetra, kao i zavisnost od mnogih lokalnih faktora (mikroklime, reljefa, orografije, i dr.), što sve umanjuje praktičnu primenljivost ovih podataka. Da bi se dobile tačnije procene za odabranu lokaciju, preporučuju se dugotrajna, specijalizovana merenja parametara energije vetra u trajanju od bar godinu [7]. Na taj način postavljaju se pouzdane osnove na bazi kojih se može dovoljno tačno odrediti količina električne energije, koju bi planirana vetroelektrana proizvela na datoj lokaciji. Ipak, ovakva merenja su skupa, dugo traju i zahtevaju angažovanje specijalizovanih stručnjaka, eksperta u ovoj oblasti.

U ovom radu se razmatraja mogućnost brzog i jednostavnog procenjivanja proizvodnje električne energije planirane vetroelektrane na osnovu korišćenja raspoloživih podataka. Cilj je da se korišćenjem raspoloživih podataka srednje godišnje vrednosti brzine i gustine snage energije vetra, kao i karakteristika vetrogeneratora razvije adekvatna metoda za inženjersku procenu proizvodnje jedne vetroelektrane. Razmatranjem različitih opcija za procenjivanje proizvodnje, predložena je metoda. Radi verifikacije ona je primenjena za jednu lokaciju i četiri vrste vetrogeneratora. Metoda je verifikovana poređenjem sa izračunatom energijom na bazi stvarnih rezultata merenja brzine vetra.

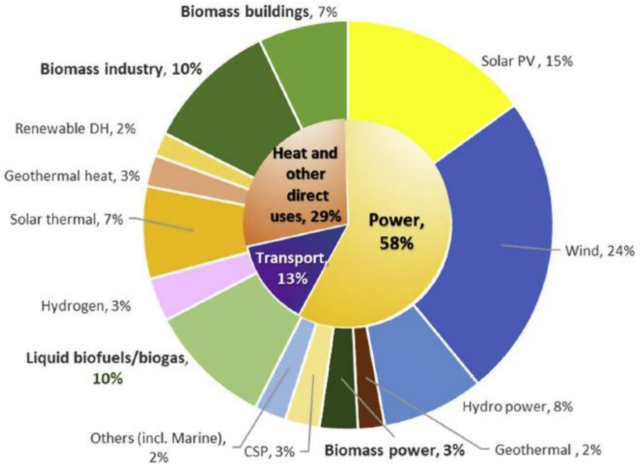

Sl. 1. Plan korišćenja obnovljivih izvora za 2050. god. [2]

II. NAČIN PRETVARANJA ENERGIJE VETRA

Energija vetra, kao linearno vazdušno kretanje pretvara se u korisnu rotacionu mehaničku energiju posredstvom trokrake

Vladimir A. Katić je sa Fakulteta tehničkih nauka, Univerziteta u Novom Sadu, Trg Dositeja Obradovića 6, 21000 Novi Sad, Srbija (e-mail: katav@uns.ac.rs).

vetroturbine. Vetroturbina je postavljena na horizontalnu osovinu na vrhu nosećeg stuba. Zbog male brzine obrtanja (20-30 min^{-1}) ova osovina se naziva „spora“. Da bi se postigna potrebna ugaona brzina za pogon električnog generatora koristi se mehanički sklop kojim se povećava brzina - multiplikator brzine. Njime se pogon prenosi na „brzu“ osovinu, koja je direktno spregnuta na električni generator. Na njoj se nalazi i mehanička kočnica, za zaustavljanje pogona u slučajevima velikih brzina vetra ili havarije. Generator pretvara mehaničku energiju prenetu sa vetroturbine u električnu energiju, koja predstavlja finalni proizvod rada vetrogeneratora. Ta električna energija se zatim prilagođava parametrima mreže putem energetskih elektronskih pretvarača (obično dvostrukih pretvarača tipa AC/DC–DC/AC), a naponski pomoću energetskih transformatora. Na sl. 2 prikazan je presek vetrogeneratora, odnosno princip vetroelektričnog agregata sa nekim od pomenutih sklopova.

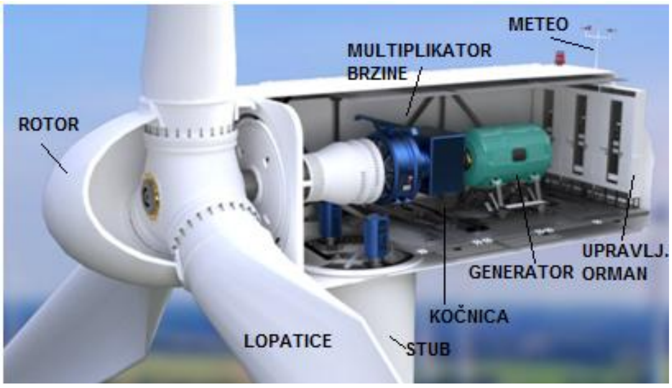

Sl. 2. *Princip konverzije energije vetra u električnu energiju [8]*

III. PRORAČUN ENERGETSKIH MOGUĆNOSTI

Generalno energija vetra se izražava preko gustine snage, kao:

$$P_v/A = \tfrac{1}{2}\,\rho \cdot v^3, \qquad (1)$$

gde je P_v snaga vetra, A površina osnove cilindra kroz koji struji vetar, ρ specifična gustina vazduha na određenoj nadmorskoj visini i v brzina vetra [1,3,7]. Vidi se da je najuticajniji parametar brzina vetra, pa je njeno precizno određivanje od ključnog značaja.

A. *Brzina vetra*

Brzina vetra dnevno se meri u široko postavljenoj mreži hidro-metoeroloških stanica, kako u Srbiji tako i u svetu. Obično se merenja vrše na 10 m visine na svakih 10 minuta, tj. sa 10-min. usrednjavanjem. Za potrebe vetroenergetike, to nije dovoljno, jer se moderne vetroturbine nalaze na visinama od 100 m ili više. Iz tog razloga, potrebno je ili vršiti merenja na visini vetroturbine ili izmerene vrednosti brzine preračunati na odgovarajuću visinu, uvažavajući i orografiju terena izraženu koeficijentom z_0.

Međutim, iz naučne literature i raspoloživih web sajtova može se dobiti vrednost prosečne godišnje brzine vetra na određenoj lokaciji i visini. Na primer, iz studije “Atlas vetrova AP Vojvodine” može se dobiti prikaz prosečne godišnje brzine vetra na visini od 100 m (sl. 3.a) sa koje se vidi da ona u jugo-istočnoj Vojvodini iznosi preko 5 m/s, odnosno preko 6 m/s [3]. Za isti deo Vojvodine, sa sajta „Global Wind Atlas”, dobija se da je prosečna godišnja brzina vetra na 100 m iznosi od 5,1 m/s do 9,2 m/s [6].

Za projektovanje novih vetroelektrana ključni podatak je mogući iznos proizvedene električne energije, pa je pitanje da li se i na osnovu ovakvih podataka može dobiti prihvatljiva procena o generisanoj energiji.

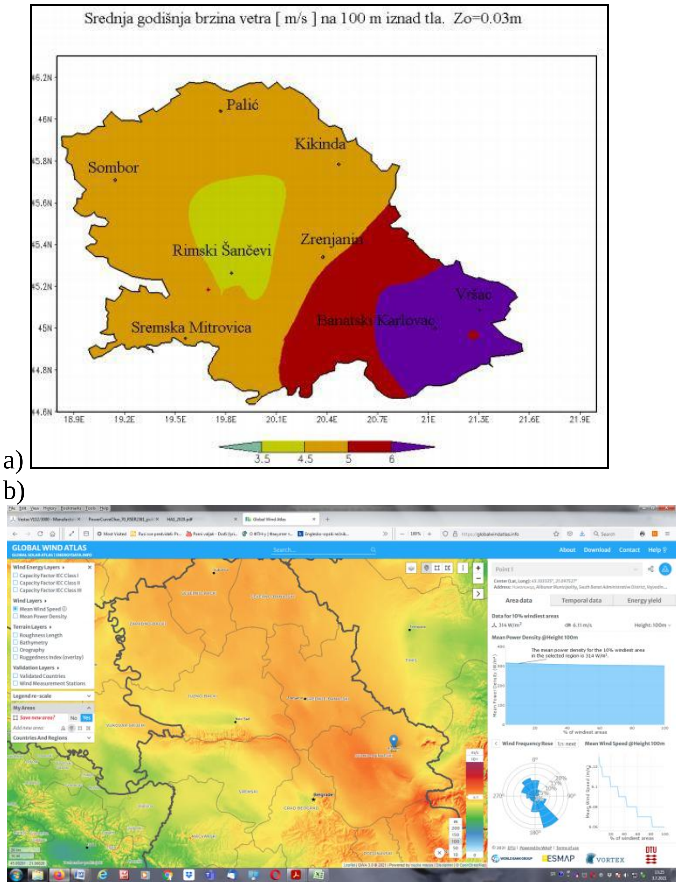

Sl. 3. P*rosečne godišnje brzine vetra u Vojvodini na 100 m iznad tla prema: a) “Atlasu vetrova APVojvodine” [3] i b) “Global Wind Atlas-u”[6]*

B. *Snaga vetra*

Za odabir snage vetroturbine u sklopu vetroelektrane potrebno je proračunati snagu vetra na zahvatu vetrogeneratora. Merenja pokazuju da raspodelu brzina najbolje prati *Weibull*-ova funkcija raspodele, koju karakterišu faktor oblika (k) i kaktor skaliranja (c) [1,3,7]. Međutim, za većinu lokacija prihvatljiva je vrednost faktora oblika k=2, kad se ova funkcija naziva *Rayleigh*–ova. Sada se srednja godišnja gustina snage može izračunati kao [7]:

$$P_{vSR}/A = 6/\pi\ \tfrac{1}{2}\ \rho \cdot (v_{SR})^3 \qquad (2)$$

gde je v_{SR} srednja vrednost brzina za određenu lokaciju, koja se dobija iz raspoloživih podataka (kao na sl. 3), a gustina vazduha obično ρ =1,225 kg/m^3 (mada pri većim nadmorskim visinama potrebno ju je posebno proračunati).

Za određen tip vetrogeneratora, može se iz podataka o vetroturbini dobiti površina zahvata, kao $A=R^2\pi$, gde je R dužina lopatica. Na primer, vetrogenerator Vestas V112-3.08 snage 3.08 MW, čije su karakteristike date u tabeli 1 [9], svojim lopaticama od 56 m prebriše površinu od 9.852 m^2, te uz prosečnu godišnju brzinu vetra od v_{SR} =6,12 m/s, prihvata srednju godišnju snagu vetra od 2,8 MW.

C. *Snaga vetrogeneratora*

Snaga vetra se koristi za pokretanje vetroturbine, čiji rad se može podeliti u četiri zone: 1 – polazna $P_{t1}=0$ ($0<v<v_{in}$), 2 – radna $P_{t2}=f(v)$ ($v_{in}<v<v_n$), 3 - nominalna $P_{t3}=Pn$ ($v_n<v<v_{out}$) i 4 – zaustavna $P_{t4}=0$ ($v>v_{out}$). Na slici 4 prikazane su krive snage nekoliko komercijalnih vetrogeneratora snaga od 2 MW do 3 MW i to REpower MM82 (2 MW), Enercon E 82/2300 (2,3 MW), Nordex N90/2500 (2,5 MW) i Vestas V112/3.08 (3.08 MW). Mogu se uočiti četiri pomenute radne zone.

Za određivanje proizvodnje vetrogeneratora interesantne su radna i nominalna zona, dok je u preostale dve zone snaga turbine jednaka nuli (u polaznoj zoni, jer nije ostvaren dovoljan momenat za pokretanje, a u zaustavnoj zoni da bi se izbegla prevelika mehanička naprezanja). U radnom delu snaga turbine definisana je koeficijentom snage C_p, pa je sada snaga zavisna od brzine vetra na kub:

$$P_{t2} = C_p\cdot P_v = \tfrac{1}{2}\cdot C_p\cdot \rho\cdot A\cdot v^3 = 3/\pi\cdot C_p\cdot \rho\cdot A\cdot (v_{SR})^3 \qquad (3)$$

Za proizvodnju najbolje je da turbina radi sa maksimalnom snagom (C_{pmax}), odnosno da je $P_t = C_{pmax}\cdot P_v$. Na primer, za pomenuti model Vestas V112/3080 podaci iz literature definišu $C_{pmax}=0{,}43$, pa bi prosečna snaga turbine na lokaciji sa sl. 3.b) bila 43% snage vetra, odnosno 1,2 MW [10].

Međutim, u realnim uslovima ovo nije ispunjeno, jer C_p nije konstantno, već funkcija koeficijenta brzohodnosti λ (*tip-speed ratio*) i ugla zakrenutosti lopatica β [7,10]. Koeficijent brzohodnosti zavisi od brzine, pa kriva snage odstupa od kubnog zakona i ima oblik istegnute „S“ krive (sl. 4). Sa sl. 4 vidi se da je moguće izvršiti linearnu aproksimaciju ovh krivih u radnoj zoni. Primer za vetroturbinu V112/3.08 predstavljen je na sl. 5. Sada se kriva snage vetroturbine može linearizovati, tj. napisati kao:

$$P_t = \begin{cases} P_{t1} = P_{t4} = 0 \quad ,0 < v < v_{in} \ \wedge \ v > v_{out} \\ P_{t2} = P_n\cdot \dfrac{v - v_{in}}{v_n - v_{in}} \quad , \qquad v_{in} < v < v_n \\ P_{t3} = P_n \quad , \qquad\qquad v_n < v < v_{out} \end{cases} \qquad (4)$$

gde je P_n nominalna snaga u [W], v_{in} upadna brina vetra (*cut-in*), v_n nominalna brzina, v_{out} zaustavna brzina (*cut-out*), a v_{max} maksimalna brzina vetra, sve u [m/s].

Brzina vetra je promenljiva i obično varira u širokim opsezima, Na primer, u jugo-istočnoj Vojvodini (sl. 3) varira u širokom opsegu sa udarima i do 38 m/s [11]. Međutim, meri se sa 10-minutnim usrednjavanjem, čime se nivelišu kratkotrajni udari, pa je mala verovatnoća brzina iznad v_{out}.

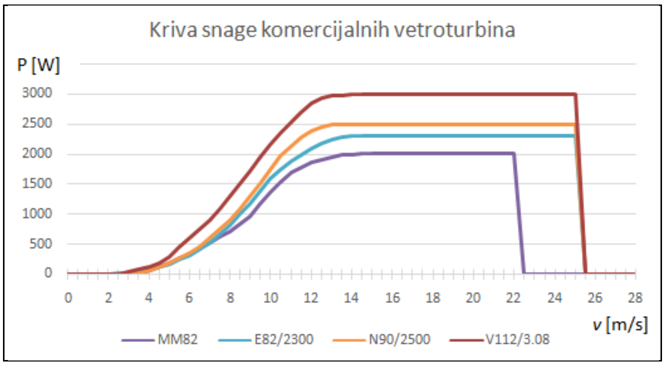

Sl. 4. Kriva snage komrcijalnih vetroturbina [9]

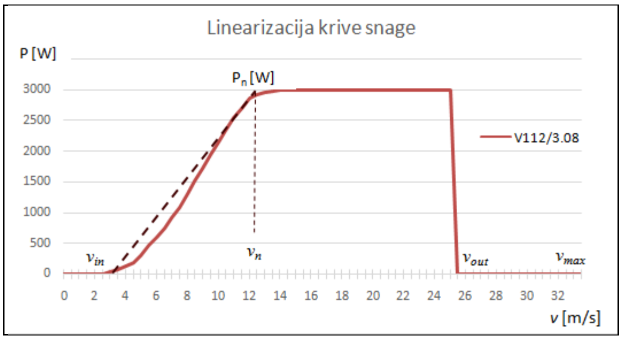

Sl. 5. Linearizacija krive snage (primer za vetroturbinu V112/3.08)

Za brze proračune ovakva linearizacija i aproksimacija maksimalne brzine je zgodna, jer se sada srednja snaga turbine u celom rasponu brzina vetra može izraziti kao:

$$P_{tSR} = P_n\cdot\left(1 - \frac{v_{in} + v_n}{2\cdot v_{out}}\right) \qquad (5)$$

Izlazna, električna snaga vetrogeneratora P_g zavisi od koeficijenta efikasnosti mehaničkog prenosa (reduktora) η_{meh} i elektro-mehaničkog pretvaranja (generatora) η_{gen}. Sada se za srednju snagu vetrogeneratora može napisati:

$$P_{gSR} = \eta_{gen}\cdot\eta_{meh}\cdot P_{tSR} \qquad (6)$$

Na primer, za vetroturbinu V112-3.08, a uz pretpostavku koeficijenata efikasnosti $\eta_{meh}=0{,}9$ i $\eta_{gen}=0{,}95$, dobija se za srednju snagu vetrogeneratora 1,03 MW.

D. *Procena proizvedene električne energije*

Najjednostavnija procena dobijene električne energije iz jednog vetrogeneratora može se dobiti, ako se iskoristi izraz (3) i pretpostavi rad sa C_{pmax}. Ona se dobija poznavanjem samo srednje brzine vetra na nekoj lokaciji (v_{SR}) i karakteristika odabranog vetrogeneratora. Sad je, na bazi (6), generisana godišnja električna energija (E_g) data sa:

$$E_g = P_g\cdot 8760 = \eta_{gen}\cdot\eta_{meh}\cdot 3/\pi\cdot C_{pmax}\cdot\rho\cdot A\cdot(v_{SR})^3\cdot 8760 \text{ [MWh]} \qquad (7)$$

Na primer, iz vetroturbine V112-3.08 i na lokaciji sa sl. 3.b), može se godišnje očekivati 8.649,23 MWh. Međutim, tu nije uvažena nelinearna priroda koeficijenta snage C_p, pa ni kriva snage vetroturbine (sl. 4), pa se ovakav metod ne može prihvatiti.

Uvažavanjem ovih faktora i uz predloženu linearizaciju krive snage, te usrednjavanje snage turbine prema (5) i uvrštavanjem u (6) za godišnju proizvodnju jednog vetrogenertora dobija se:

$$E_g = \eta_{gen}\cdot\eta_{meh}\, P_n\cdot[1-(v_{in}+v_n)/2v_{out}]\cdot 8760 \text{ [MWh]} \qquad (8)$$

Na primer, za pomenuti vetrogenerator Vestas V112-3.08 ukupna godišnja proizvodnja bila bi 16.148,01 MWh. Međutim, korišćenje izraza (5) pretpostavlja se ravnomerna raspodela brzina vetra unutar opsega usrednjavanja, što u praksi nije slučaj, pa ni ovaj metod nije prihvatljiv.

Stvarna raspodela brzina vetra prati pomenutu *Rayleigh*–ovu funkciju, pa se pomoću nje može izračunati verovatnoća pojavljivanja brzina većih od neke zadate (v_x). Kako su poznati faktori oblika i skaliranja, dobija se jednostavan izraz za ovu verovatnoću [7,12]:

$$\Psi(v \ge v_x) = e^{-\frac{\pi}{4}\left(\frac{v_x}{v_{SR}}\right)^2} \qquad (9)$$

Ovakva forma je pogodana, jer zahteva poznavanje samo srednje vrednosti brzine vetra. Uz linearizaciju krive snage, može se uzeti da je srednja snaga u radnoj zoni jednaka $P_n/2$ (srednja linija trougla), a u nominalnoj zoni P_n. Sada se za srednju godišnju snagu vetroturbine može očekivati da je:

$$P_{tSR} = [1/2 \cdot \Psi(v_{in}<v<v_n)+\Psi(v_n<v<v_{out})] \cdot P_n \qquad (10)$$

Kako je:

$$\Psi(v_{in}<v<v_n)=\Psi(v>v_{in})-\Psi(v>v_n), \qquad (11)$$

odnosno

$$\Psi(v_n<v<v_{out})=\Psi(v>v_n)-\Psi(v>v_{out}) \qquad (12)$$

izraz (10) se može napisati kao:

$$P_{tSR} = [1/2 \cdot \Psi(v>v_{in})+1/2 \cdot \Psi(v>v_n)-\Psi(v>v_{out})] \cdot P_n \qquad (13)$$

S obzirom da se verovatnoća $\Psi(v>v_{out})$ može zanemariti u odnosu na ostale, dobija se:

$$P_{tSR} = [\Psi(v>v_{in})+\Psi(v>v_n)] \cdot P_n/2 \qquad (14)$$

Sad se ukupna godišnja proizvodnja električne energije nekog vetrogeneratora može proceniti na:

$$E_g = \eta_{gen} \cdot \eta_{meh} \cdot [\Psi(v>v_{in})+\Psi(v>v_n)] \cdot P_n/2 \cdot 8760 \text{ [MWh]} \qquad (15)$$

Na primer, za srednju godišnju brzinu v_{SR}=6,12 [m/s] i vetrogenerator V112-3.08, godišnji prinos električne energije može se proceniti na 9.951,8 MWh.

IV. PROVERA TAČNOSTI METODE

Radi provere tačnosti predložene metode procene godišnje proizvodnje električne energije jednog vetrogeneratora biće iskorišćeni stvarni rezultati merenja brzine vetra na visini 60 m (sa usrednjavanjem na 10 minuta) na lokaciji u Banatu [13]. Za poređenje su odabrana četiri različita tipa vetrogeneratora snaga oko 3 MW, čije osnovne karakteristike su date u tabeli 1.

Rezultati su predstavljeni u tabeli 2. Za sva četiri odabrana vetrogeneratora izračunate su vrednosti proizvedene energije u jednogodišnjem period (E_g) prema jednačinama (7), (8) i jednačini (15) - predloženom metodu. Radi tačnog poređenja, rezultati merenja brzine vetra preračunati su na visinu stuba odabranog vetrogeneratora. Na kraju je izračunata greška predložene metode u odnosu na izmereni rezultat.

Može se uočiti da se metoda može primenjivati za brze procene generisane električne energije nekog vetrogeneratora, jer je greška procene u svim slučajevima ispod 5%. Takođe, vidi se da korišćenje jednačina (7) i (8) nije pogodno, jer je greška značajno veća, tj. neprihvatljiva.

V. ZAKLJUČAK

Korišćenje energije vetra za proizvodnju električne energije beleži sve veći porast i otkriva u sve većoj meri svoj pravi potencijal i značaj. U radu je predložena metoda, kojom se korišćenjem raspoloživih podataka o srednjoj godišnjoj vrednosti brzine i gustine snage energije vetra, kao i karakteristika vetrogeneratora može proceniti proizvodnja električne energije jedne vetroelektrane. Metoda je testirana i prikazala je zadovoljavajuću tačnost, te se može pouzdano primeniti za brze inženjerske procene rada vetroelektrane.

Tabela 1. Osnovne karakteristike odabranih vetrogeneratora [9]

Vetrogenerator	**V112-3.08**	**SWT-3.0-101**	**N131/3000**	**GE 3.2-130**
Proizvođač	Vestas	Siemens	Nordex	Gen.Electric
Snaga (MW)	3.08	3.0	3.0	3.2
v_{in} (m/s)	3,0	3,0	3,0	2,0
v_n (m/s)	12,0	12,5	11,5	12,0
v_{out} (m/s)	25,0	25,0	20,0	25,0
Lopatice, R(m)	56	50,5	65,5	65
Visina (m)	94,0	115	114	110

Tabela 2. Poređenje rezultata primenjene metode i merenja na različitim vrstama vetrogeneratorima

Vetrogenerator /Metod (v_{SR}=6,12 m/s)	**V112-3.08** E_g [MWh]	**SWT-3.0-101** E_g [MWh]	**N131/3000** E_g [MWh]	**GE 3.2-130** E_g [MWh]
Jedn. (7)	8.649,2	7.573,0	12.699,5	12.344.5
Jedn. (8)	16.148,0	15.503,9	14.324,2	17.256,5
Jedn. (15) (Predl.metod)	10.048,1	9.823,3	10.109,8	11.657,9
Merenje	9.951,8	9.619,9	10.528,4	12.085,8
Greška metode	0,97%	2,11%	3.98%	3,54%

LITERATURA

[1] L. Freris, D. Infield, *„Renewable Energy in Power Systems“*, J. Wiley & Sons, Chichester, 2008.

[2] D. Gielen et al., „The role of renewable energy in the global energy transformation“, *Energy Strategy Reviews*, Vol. 24, 2019, pp.38-50.

[3] V.A. Katić i sarad., *“Atlas vetrova AP Vojvodine“*, Studija, Pokrajinski sekretarijat za energetiku i mineralne sirovine, Fakultet tehničkih nauka, Novi Sad, 2008

[4] https://mre.gov.rs

[5] R. Putnik i sarad., *„Mogućnost korišćenja energije vetra za proizvodnju električne energije“*, Studija, Elektroprivreda Srbije, Beograd, 2002.

[6] https://globalwindatlas.info/

[7] Ž. Đurišić, *„Vjetroelektrane“*, Akademska misao, Beograd, 2019.

[8] https://www.infineon.com/cms/en/applications/industrial/wind-energy-systems/

[9] https://www.thewindpower.net

[10] C. Carrillo et al., “Review of power curve modelling for wind turbines”, *Renewable and Sustainable Energy Reviews*, Vol.21, 2013, pp.572-581.

[11] P. Katić i dr. *„Klima SAP Vojvodine“*, Poljopr. fakultet, Novi Sad, 1979.

[12] Z. Ivanović, V.A. Katić, *„Obnovljivi izvori električne energije – vežbe“*, Fakultet tehničkih nauka, Edicija Tehničke nauke - udžbenici, br.707, Novi Sad, 2018.

[13] M. Hrnjak, *“Glavne karakteristike i komponente vetroelektrane u jugoistočnom Banatu”*, Master rad, Fakultet tehničkih nauka, Novi Sad, 2021.

ABSTRACT

In this paper, the possibility of quick and simple estimation of electricity production of the planned wind power plant based on the use of available data is considered. We started from the assumption that the average annual values of wind speed and power density are available. By considering different options for estimating production, one method has been proposed. For verification, it was applied to one location and four types of wind turbines. The method was verified by comparison with the calculated energy based on the actual results of wind speed measurements. Satisfactory accuracy suitable for engineering assessments was achieved, which justified the method of application.

A Method for Engineering Assessment of Wind Farm Production

Vladimir A. Katić

Modelovanje sistema za regulaciju pobude sinhronog generatora primjenom nelinearnog ARX modela

Mihailo Micev, *Student Member, IEEE*, Martin Ćalasan i Milovan Radulović, *Member, IEEE*

***Apstrakt*—U ovom radu prikazana je primjena nelinearnog auto – regresionog modela sa spoljašnjim ulazom (ARX) u cilju modelovanja sinhronog generatora tokom rada sa opterećenjem. Ulazni signal u sinhroni generator predstavljen je naponom pobude, dok je izlazni signal ustvari napon na krajevima generatora. Stoga je za estimaciju parametara usvojenog modela neophodno koristiti samo napon pobude i izlazni napon generatora, koji predstavljaju ulazno – izlazni set podataka. Dodatno, predložena identifikaciona procedura se bazira na promjeni referentnog napona sistema za regulaciju pobude sinhronog generatora. Opisana procedura je implementirana u programskom paketu MATLAB Simulink. Rezultati dobijeni korišćenjem nelinearnog ARX modela sinhronog generatora se sa velikom tačnošću poklapaju sa rezultatima koji su dobijeni u Simulink-u.**

***Ključne reči*—nelinearni ARX model; sinhroni generator; sistem za regulaciju pobude.**

I. UVOD

ELEKTROENERGETSKI sistem je složen, dinamički sistem čija je glavna funkcija da sigurno, kvalitetno, pouzdano i ekonomično snabdijeva potrošače električnom energijom. Kompletan elektroenergetski sistem se sastoji iz podsistema proizvodnje, distribucije, prenosa i potrošnje električne energije. Proizvodnja električne energije se odvija u elektranama, u kojima se različiti oblici primarne energije, pomoću električnih generatora, transformišu u električnu energiju. Najčešće korišćeni električni generator je klasični sinhroni generator, dok se rjeđe u upotrebi mogu sresti asinhroni generator (najčešće dvostrano napajani), sinhroni generator sa stalnim magnetima, generator jednosmjerne struje itd. [1].

Brojne studije vezane za analizu elektroenergetskih sistema, kao što su studije stabilnosti, planiranja, testiranja sistema, analize dinamičkog odziva prilikom prelaznih procesa, zahtijevaju precizno i tačno modelovanje svake komponente sistema. Stoga, modelovanje sinhronog generatora, kao jednog od najvažnijih elemenata elektroenergetskog sistema, predstavlja veoma važan i zahtjevan zadatak [1], [2].

Zbog važnosti i velikog značaja modelovanja sinhronog generatora, brojne procedure za određivanje njegovih parametara su standardizovane i sublimirane u IEEE [3] i IEC standardima [4]. Osim toga, značajan broj naučnih radova je posvećen problematici modelovanja, odnosno estimacije parametara generatora. Metod baziran na naglom uklanjanju opterećenja je demonstriran u [5], dok je estimacija parametara na osnovu ogleda kratkog spoja prikazana u [6]. Procedura identifikacije parametara generatora kada se na ulaz dovode sinusoide različite frekvencije, tzv. *standstill frequency response test* (SSFR) demonstriran je u [7]. Jedan od modernijih i novijih identifikacionih metoda baziran je na podacima koji se dobijaju sa *phasor measurement unit*-a (PMU) (fazor napona, aktivna snaga, itd.) [8]. Takođe, u literaturi se mogu sresti i identifikacione procedure prilikom kojih se na namotaj pobude dovode signali različitih oblika: *chirp* signal [9], *sinc* signal [10], *pseudorandom binary sequence* (PRBS) signal [11], itd.

U ovom radu sinhroni generator se modeluje pomoću nelinearnog auto – regresionog modela sa spoljašnjim ulazom (ARX), čiji opis se može naći u [12], [13]. Kao ulazni signal u sinhroni generator koristi se napon pobude, dok je izlazni signal predstavljen preko napona na namotaju statora generatora. Ulazno – izlazni set podataka je dobijen modelovanjem sinhronog generatora, zajedno sa sistemom za automatsku regulaciju pobude generatora, u programskom paketu MATLAB Simulink. Na osnovu dobijenog seta podataka pomoću simulacionog modela, generator se modeluje pomoću pomenutog nelinearnog ARX modela, koji pokazuje izuzetno veliki stepen tačnosti. Sličan pristup se može sresti u [14], gdje se za modelovanje sinhronog generatora koristi takođe nelinearni ARX model, ali kod kojeg su nelinearnosti predstavljene stepenim funkcijama. Takođe, u pomenutom radu parametri modela su estimirani korišćenjem $H\infty$ identifikacionog metoda.

Ovaj rad je organizovan na sljedeći način: u drugom poglavlju su date osnovne informacije o modelu koji je formiran u Simulink-u u cilju dobijanja seta ulazno-izlaznih mjerenja. Treće poglavlje je posvećeno prikazu korišćenog nelinearnog modela, dok su u četvrtom prikazani dobijeni rezultati. Na kraju, u Zaključku su ukratko sumirani rezultati i dati komentari vezani za budući rad.

Mihailo Micev – Elektrotehnički fakultet, Univerzitet Crne Gore, Bulevar Džordža Vašingtona bb, 81000 Podgorica, Crna Gora (e-mail: mihailom@ ucg.ac.me).

Martin Ćalasan – Elektrotehnički fakultet, Univerzitet Crne Gore, Bulevar Džordža Vašingtona bb, 81000 Podgorica, Crna Gora (e-mail: martinc@ ucg.ac.me).

Milovan Radulović – Elektrotehnički fakultet, Univerzitet Crne Gore, Bulevar Džordža Vašingtona bb, 81000 Podgorica, Crna Gora (e-mail: milovanr@ ucg.ac.me).

II. SIMULACIONI MODEL SINHRONOG GENERATORA

Kvalitet električne energije, kao i stabilnost elektroenergetskog sistema, u velikoj mjeri zavise od dva parametra, a to su napon i frekvencija. Frekvencija se smatra globalnim parametrom, jer je njena nazivna vrijednost jednaka u cijelom elektroenergetskom sistemu. Međutim, za napon se može reći da je lokalni parametar, jer njegova nazivna vrijednost zavisi od naponskog nivoa u svakom dijelu sistema pojedinačno. Zbog važnosti ova dva parametra, veoma je bitno održavati njihove vrijednosti na vrijednostima koje su bliske nazivnim, pri čemu je za napon dozvoljeno nešto veće odstupanje nego za frekvenciju. Regulacija frekvencije, tj. njeno održavanje na konstantnoj vrijednosti (50 ili 60 Hz, zavisno od sistema), vrši se pomoću turbinskog regulatora djelovanjem na mehaničku snagu vratila rotora. Odnosno, frekvencija primarno zavisi od tokova aktivnih snaga u elektroenergetskom sistemu, čime se formira takozvana *P-f* regulaciona kontura. Sa druge strane, djelovanjem na pobudu sinhronog generatora, može se uticati na tokove reaktivnih snaga, čime se definiše i naponski profil mreže. Na ovaj način može se definisati i druga regulaciona kontura koja predstavlja vezu između napona i reaktivnih snaga, odnosno *Q-U* kontura. Osim sinhronog generatora, za regulaciju tokova reaktivnih snaga mogu se koristiti redna i otočna baterija kondenzatora, sinhroni kompenzator, regulacioni transformator, statički VAr kompenzator, reaktor, itd.

U ovom radu se razmatra sinhroni generator kao najčešće korišćeno naponsko – reaktivno regulaciono sredstvo. Sinhroni generator je glavna komponenta sistema za regulaciju pobude sinhronog generatora, čija blok šema je prikazana na Slici 1.

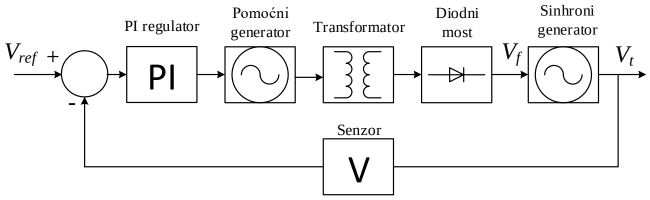

Sl. 1. Blok šema sistema za regulaciju pobude sinhronog generatora.

Prethodno prikazana šema je samo jedna od mogućih šema sistema za regulaciju pobude sinhronog generatora. Bitno je naglasiti da je prikazana struktura sistema za regulaciju pobude sinhronog generatora uprošćena u odnosu na onu koja se primjenjuje u stvarnim elektranama. Izlazni napon generatora V_t, tj. napon na namotajima statora, mjeri se pomoću senzora i upoređuje sa referentnim naponom V_{ref}. U komparatoru se, na osnovu te razlike, formira signal greške koji predstavlja ulaz u PI regulator. Dalje, regulator na svom izlazu daje upravljački signal, koji ustvari predstavlja pobudni napon za pomoćni sinhroni generator, čija snaga je značajno manja od snage glavnog sinhronog generatora. Pomoćni generator na svom izlazu daje naizmjenični napon, koji se pomoću transformatora i ispravljačkog diodnog mosta pretvara u jednosmjerni napon. Ovako dobijeni jednosmjerni napon V_f služi za napajanje pobudnog namotaja glavnog sinhronog generatora, tako da napon na izlazu što bolje prati referentni napon.

Prethodno opisana blok šema implementirana je u programskom paketu MATLAB Simulink. Podaci o korišćenim elementima su sljedeći:

- Glavni sinhroni generator: S_n=2 MVA, U_n=400 V,
- Pomoćni sinhroni generator: S_n=8.1 kVA, U_n=400 V,
- Trofazni transformator: sprega Yd1, S_n=10 kVA, U_{n1}/U_{n2}=400 V/12 V,
- Diskretni PI regulator: K_p=10, K_i=8.
- Opterećenje koje napaja generator je čisto aktivno, snage 500 kW.

U sprovedenim simulacijama referentni napon V_{ref} je najprije podešen na nazivnu vrijednost (tj. 1 pu), zatim se nakon 10 s poveća na 1.03 pu, da bi se nakon dodatnih 10 s referentni napon smanjio na 0.97 pu. Tokom ovakvog režima rada generatora, neophodno je snimiti talasne oblike napona pobude V_f i izlaznog napona V_t. Cilj ovog rada je da se, na osnovu ovako snimljenih talasnih oblika, estimiraju parametri nelinearnog matematičkog modela generatora koji će biti opisan u narednom poglavlju.

Kao što je i prethodno opisano, referentni napon generatora prikazan je na Slici 2. Nakon toga, na Slici 3 prikazan je izlazni napon generatora, dok je na Slici 4 prikazan napon pobude generatora u ovakvom režimu rada.

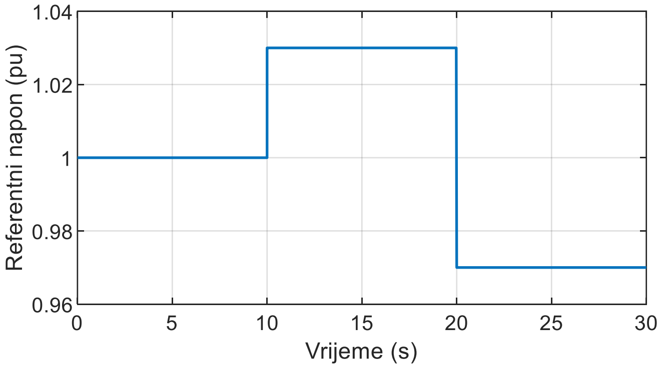

Sl. 2. Referentna vrijednost napona generatora.

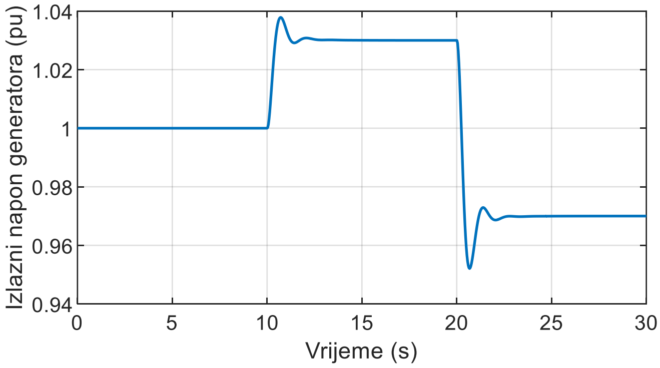

Sl. 3. Izlazni napon generatora dobijen u Simulink-u.

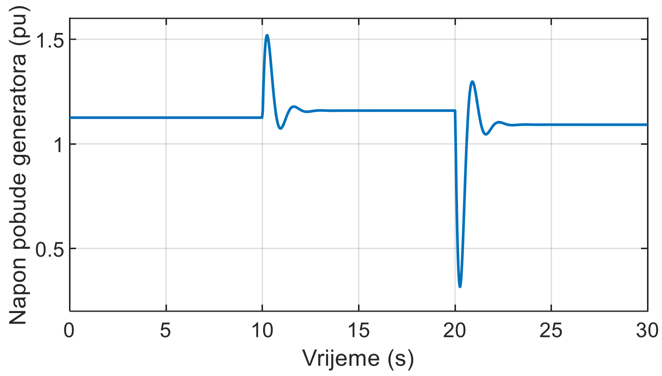

Sl. 4. Napon pobude generatora dobijen u Simulink-u.

III. NELINEARNI ARX MODEL

U ovom poglavlju prikazan je nealinearni ARX model koji je korišćen u radu u cilju modelovanja sinhronog generatora na osnovu mjerenih ulaznih i izlaznih podataka. Set ulazno – izlaznih podataka neophodan za estimaciju parametara nelinearnog ARX modela dobijen je iz simulacije rada sinhronog generatora u Simulink-u, kao što je i opisano u prethodnom poglavlju.

U cilju boljeg razumijevanja nelinearnog modela, korisno je prvo ukratko prikazati linearni ARX model. Naime, ukoliko se sa *u*(*k*) i *y*(*k*) označe diskretna ulazna i izlazna mjerenja u trneutku *k*, respektivno, veza između izlaza i ulaza data je na sljedeći način:

$$A(z)y(k)=B(z)u(k)+e(k), \qquad (1)$$

gdje *e*(*k*) predstavlja poremećaj, a *A*(*z*) i *B*(*z*) su polinomi reda n_a i n_b, respektivno, po promjenljivoj z^{-1} koja predstavlja jedinično kašnjenje:

$$A(z)=1+a_1z^{-1}+a_2z^{-2}+\ldots+a_{n_a}z^{-n_a}=1+\sum_{i=1}^{n_a}a_iz^{-i}, \qquad (2)$$

$$B(z)=b_1z^{-1}+b_2z^{-2}+\ldots+b_{n_b}z^{-n_b}=\sum_{i=1}^{n_b}b_iz^{-i}. \qquad (3)$$

Koristeći prethodne definicije polinoma *A*(*z*) i *B*(*z*), (1) se može zapisati i na sljedeći način:

$$\left[1+\sum_{i=1}^{n_a}a_iz^{-i}\right]y(k)=\sum_{i=1}^{n_b}b_iz^{-i}u(k)+e(k), \qquad (4)$$

odakle slijedi:

$$y(k)=-\sum_{i=1}^{n_a}a_iz^{-i}y(k)+\sum_{i=1}^{n_b}b_iz^{-i}u(k)+e(k), \qquad (5)$$

ili uzimajući u obzir značenje operatora kašnjenja z^{-1}:

$$y(k)=-\sum_{i=1}^{n_a}a_iy(k-i)+\sum_{i=1}^{n_b}b_iu(k-i)+e(k). \qquad (6)$$

Kao što se može zaključiti na osnovu (6), kod linearnog ARX modela izlaz *y*(*k*) predstavlja linearnu kombinaciju izlaza u prethodnim trenucima $y(k-1)$, $y(k-2)$, ..., $y(k-n_a)$, kao i ulaza $u(k-1)$, $u(k-2)$, ..., $u(k-n_b)$. Ovi članovi se jednim imenom nazivaju regresori, tako da se može reći da je kod ARX modela izlaz u trenutku *k* linearna funkcija ostalih regresora.

Za razliku od prethodno opisanog modela, kod nelinearnog ARX modela postoji nelinearna funkcija mapiranja *F* između izlaza *y*(*k*) i ostalih regresora:

$$y(k)=F\begin{bmatrix}y(k-1),y(k-2),\ldots,y(k-n_a),\\ u(k-1),u(k-2),\ldots,u(k-n_b)\end{bmatrix}. \qquad (7)$$

U ovom radu se kao nelinearna funkcija mapiranja *F* koristi tzv. *wavenet* funkcija, koja ustvari predstavlja mrežu, tj. sumu *wavelet* funkcija. Struktura ovakvog nelinearnog ARX modela ilustrovana je na Slici 5.

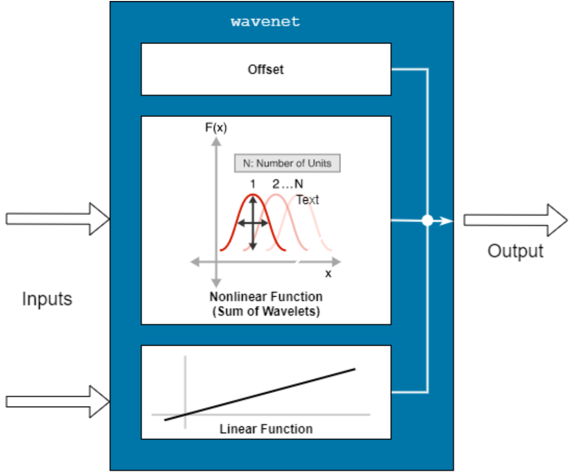

Sl. 5. Struktura nelinearnog ARX modela sa wavenet funkcijom mapiranja.

Sa matematičkog aspekta, *wavenet* mapiranje se može prikazati sljedećom relacijom:

$$y(k)=y_0+\left(X(k)-\bar{X}\right)^T PL+W\left[X(k)\right]+S\left[X(k)\right], \qquad (8)$$

gdje *X*(*k*) predstavlja vektor od ukupno *m* regresora, a $\bar{X}$ njegovu srednju vrijednost, y_0 je izlazni ofset (skalar), *P* je projekciona matrica dimenzija *mxp* (*p* – broj linearnih regresora), a *L* je vektor težinskih koeficijenata dimenzija *p*x1. Nelinearni dio *wavenet* funkcije mapiranja ogleda se u funkcijama *W*[*X*(*k*)] i *S*[*X*(*k*)]. Preciznije, funkcija *W*[*X*(*k*)] predstavlja sumu proširenih i transliranih *wavelet*-a, dok funkcija *S*[*X*(*k*)] predstavlja sumu proširenih i transliranih funkcija skaliranja, odnosno *scalelet*-a. Matematičke formulacije funkcija *W*[*X*(*k*)] i *S*[*X*(*k*)] definisane su pomoću (9) i (10):

$$W\left[X(k)\right]=\sum_{i=1}^{d_w}w_if_w\left(b_i\left(X-\bar{X}\right)^TQ-c_i\right), \qquad (9)$$

$$S\left[X(k)\right]=\sum_{i=1}^{d_s}s_if_s\left(d_i\left(X-\bar{X}\right)^TQ-e_i\right). \qquad (10)$$

Oznake koje se pojavljuju u (9) i (10) imaju sljedeća značenja:

- *Q* je projekciona matrica dimenzija *mxq* (*q* – proizvoljan parametar manji ili jednak od *m*),
- w_1 – w_{dw} su skalarni *wavelet* koeficijenti,
- s_1 – s_{ds} su skalarni *scaling* koeficijenti,
- b_1 – b_{dw} su skalari pod nazivom *wavelet* proširenja, dok su d_1 – d_{ds} skalari koji se zovu *scaling* proširenja koji množe ulaznu matricu,

- $c_1 - c_{dw}$ je vektor pod nazivom *wavelet* translacija,
- $e_1 - e_{ds}$ je vektor *scaling* translacija,
- f_w i f_s su funkcije definisane pomoću sljedećih relacija:

$$f_w(x) = e^{-xx^T/2}, \tag{11}$$

$$f_s(x) = \left(\dim(x) - xx^T\right) e^{-xx^T/2}. \tag{12}$$

Estimacija parametara nelinearnog ARX modela izvršena je korišćenjem Levenberg – Marquardt algoritma [15], [16]. Ovaj algoritam je izuzetno pogodan za rješavanje nelinearnog problema najmanjih kvadrata prilikom tzv. *curve fitting*.

IV. REZULTATI SIMULACIJA

U ovom poglavlju prikazanu su rezultati dobijeni modelovanjem sinhronog generatora pomoću nelinearnog ARX modela. Naime, blok šema opisana u drugom poglavlju implementirana je u Simulink-u i dobijeni su napon pobude i napon na izlazu generatora koji su prikazani na Slikama 3 i 4. Ovako dobijeni napon pobude i izlazni napon generatora formiraju set ulazno – izlaznih podataka pomoću kojeg se vrši estimacija parametara nelinearnog ARX modela.

Važno je ukazati da relacija (8) predstavlja najopštiju formu *wavenet* mapiranja kod nelinearnog ARX modela. U ovom radu nelinearni ARX model predstavljen je samo funkcijom $W[X(k)]$ iz relacije (8). Stoga, parametri koji su estimirani su matrica Q i vektori skalarnih *wavelet* koeficijenata w, wavelet proširenja b i wavelet translacija c. Korišćeno je m=28 regresora (n_a=14 i n_b=14), pri čemu su svi usvojeni kao nelinearni, a broj q je podešen na 19, čime je ispunjen uslov da je $q \leq m$.

Poređenje izlaznog napona generatora dobijenog u Simulink-u sa izlaznim naponom generatora koji je dobijen pomoću nelinearnog ARX modela dato je na Slici 6.

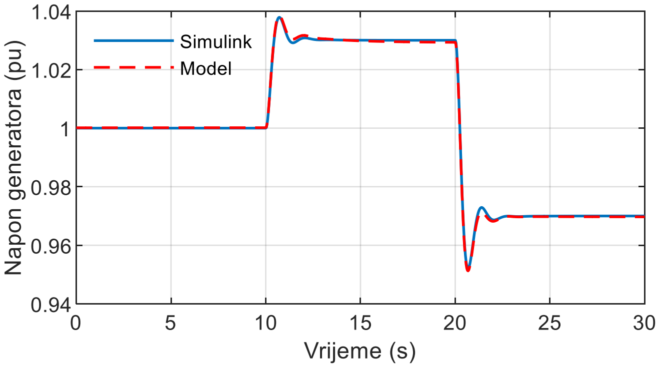

Sl. 6. Poređenje izlaznog napona generatora iz Simulink-a i izlaznog napona dobijenog primjenom nelinearnog ARX modela.

Na osnovu prethodno prikazanog grafika, jasno je da je korišćeni nelinearni ARX model izuzetno tačan i precizan jer su odstupanja od rezultata dobijenih pomoću Simulink-a veoma mala.

Nakon toga, ispitana je i mogućnost primjene nelinearnog ARX modela pri različitim uslovima u elektroenergetskom sistemu. Naime, estimacije parametara nelinearnog ARX modela izvršena je i u slučaju promjene opterećenja generatora. Razmatrana su dva slučaja: u prvom slučaju je opterećenje prepolovljeno, tj. smanjeno sa 500 kW na 250 kW, dok je u drugom slučaju opterećenje generatora udvostručeno, tj. iznosi 1000 kW. U oba slučaja izvršen je isti test: referentni napon je u početku jednak 1 pu, nakon 10 s se poveća na 1.03 pu, i nakon dodatnih 10 s se smanji na 0.97 pu. Odgovarajuća poređenja izlaznog napona iz Simulink-a sa naponom koji je dobijen primjenom nelinearnog ARX modela data su na Slikama 7 i 8. Na Slici 7 razmatran je slučaj opterećenja od 250 kW, dok je na Slici 8 analiziran slučaj kada je opterećenje generatora 1000 kW.

Kao što se može uočiti sa grafika, nelinearni ARX model omogućava odlično poklapanje rezultata sa onima dobijenim u Simulink-u i za različite uslove rada u elektroenergetskom sistemu. Time je pokazano da se ovaj model uspješno može adaptirati na promjenu uslova i da je pogodan za *online* primjenu u modelovanju sinhronog generatora.

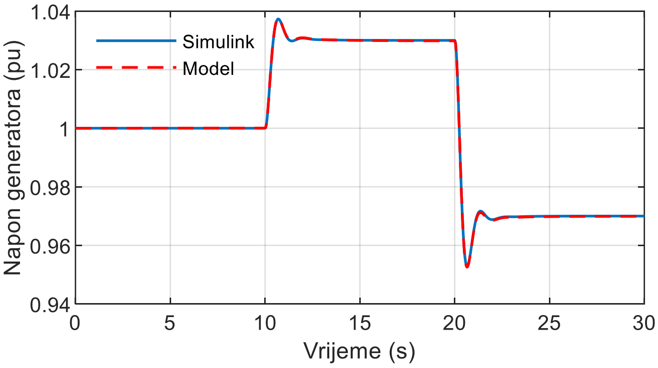

Sl. 7. Poređenje izlaznog napona generatora iz Simulink-a i izlaznog napona dobijenog primjenom nelinearnog ARX modela (za opterećenje 250 kW).

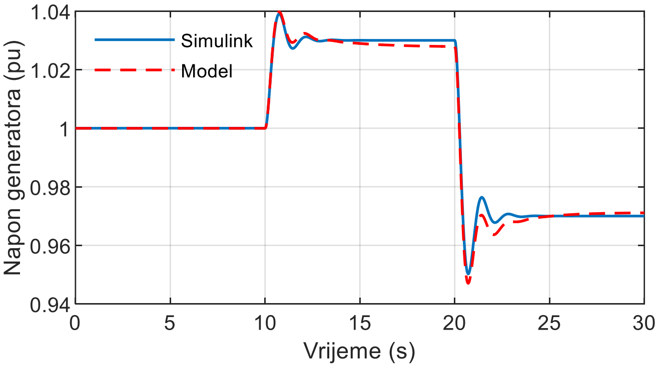

Sl. 8. Poređenje izlaznog napona generatora iz Simulink-a i izlaznog napona dobijenog primjenom nelinearnog ARX modela (za opterećenje 1000 kW).

Na ovaj način pokazano je da estimirani parametri pri određenim uslovima rada (opterećenju na krajevima generatora) daju zadovoljavajuće rezultate i kada dođe do promjene radnih uslova, odnosno promjene opterećenja. Takođe, sa prethodnih grafika uočljivo je da je stepen poklapanja rezultata tokom dinamičkih procesa u prelaznom režimu veoma veliki.

V. ZAKLJUČAK

U ovom radu razvijen je nelinearni ARX model pomoću kojeg se adekvatno može modelovati sinhroni generator.

Parametri ovog matematičkog modela estimirani su na osnovu napona pobude i napona na izlazu generatora, koji su dobijeni simulacijom sistema za regulaciju pobude sinhronog generatora u Simulink-u. Dobijeni rezultati pokazuju veliki stepen tačnosti i preciznosti korišćenog nelinearnog modela. U budućem radu biće razmotrena robusnost ovog modela u slučaju promjene parametara PI regulatora. Još jedan pravac istraživanja je primjena istog modela na eksperimentalno dobijene rezultate iz realne hidroelektrane.

LITERATURA

[1] T. A. Lipo, *Analysis of synchronous machines: Second Edition*. 2017.

[2] B. Adkins and R.G. Harley, The General Theory of Alternating Current Machines: Applications to Practical Problems, Springer-Science+Business Media, B.V.,1975.

[3] *IEEE Guide: Test Procedures for Synchronous Machines*, IEEE Standard 115-1995, 1995.

[4] *Rotating Electrical Machines—Part 4: Methods for Determining Synchronous Machine Quantities from Tests*, IEC Standard, IEC-60034-4 2008, 2008.

[5] M. Giesbrecht and L. A. E. Meneses, "Detailed derivation and experimental validation of a method for obtaining load conditions for salient pole synchronous machine quadrature axis parameters determination," *IEEE Trans. Ind. Electron.*, vol. 66, no. 7, pp. 5049–5056, 2019.

[6] V. A. D. Faria, J. V. Bernardes, and E. C. Bortoni, "Parameter estimation of synchronous machines considering field voltage variation during the sudden short-circuit test," *Int. J. Electr. Power Energy Syst.*, vol. 114, no. July 2019, p. 105421, 2020.

[7] T. L. Vandoorn, F. M. De Belie, T. J. Vyncke, J. A. Melkebeek, and P. Lataire, "Generation of multisinusoidal test signals for the identification of synchronous-machine parameters by using a voltage-source inverter," *IEEE Trans. Ind. Electron.*, vol. 57, no. 1, pp. 430–439, 2010.

[8] B. Ahmadzadeh-Shooshtari, R. Torkzadeh, M. Kordi, H. Marzooghi, and F. Eghtedarnia, "SG parameters estimation based on synchrophasor data," *IET Gener. Transm. Distrib.*, vol. 12, no. 12, pp. 2958–2967, 2018.

[9] M. Cisneros-González, C. Hernandez, R. Morales-Caporal, E. Bonilla-Huerta, and M. A. Arjona, "Parameter estimation of a synchronous-generator two-axis model based on the standstill chirp test," *IEEE Trans. Energy Convers.*, vol. 28, no. 1, pp. 44–51, 2013.

[10] M. A. Arjona, M. Cisneros-Gonzalez, and C. Hernandez, "Parameter estimation of a synchronous generator using a sine cardinal perturbation and mixed stochastic deterministic algorithms," *IEEE Trans. Ind. Electron.*, vol. 58, no. 2, pp. 486–493, 2011.

[11] M. Hasni, O. Touhami, R. Ibtiouen, M. Fadel, and S. Caux, "Estimation of synchronous machine parameters by standstill tests," *Math. Comput. Simul.*, vol. 81, no. 2, pp. 277–289, 2010, doi: 10.1016/j.matcom.2010.05.010.

[12] https://www.mathworks.com/help/ident/index.html?s_tid=CRUX_lftnav

[13] B. Kovačević and G. Kvaščev, Identifikacija procesa, Akademska misao, Beograd, 2018.

[14] M. Dehghani, M. Karrari, W. Rosehart, and O. P. Malik, "Synchronous machine model parameters estimation by a time-domain identification method," *Int. J. Electr. Power Energy Syst.*, vol. 32, no. 5, pp. 524–529, 2010, doi: 10.1016/j.ijepes.2009.07.010.

[15] K. Levenberg, "A Method for the Solution of Certain Non-Linear Problems in Least Squares," *The Quarterly of Applied Mathematics*, vol. 2, pp 164-168, 1944.

[16] D.W. Marquardt, "An algorithm for least-squares estimation of nonlinear parameters," *Journal of the Society for Industrial and Applied Mathematics*, vol. 11, no. 2, pp. 431-441, 1963.

ABSTRACT

In this paper, the application of a nonlinear auto – regression model with external input (ARX) in order to model a loaded synchronous generator is presented. The input signal to the synchronous generator is represented as the field voltage, while the output signal is actually the terminal voltage of the generator. Therefore, to estimate the parameters of the adopted model, it is necessary to use the field voltage and the terminal voltage signals, which form the input – output data set. Additionally, the proposed experiment is based on changing the reference voltage of the synchronous generator excitation control system. The described procedure is implemented in the MATLAB Simulink software package. The results obtained using the proposed model of the synchronous generator coincide with high accuracy with the results obtained in Simulink.

Modelling of synchronous generator excitation control system using nonlinear ARX model

Mihailo Micev, Martin Ćalasan, Milovan Radulović

Identifikacija parametara mašine jednosmerne struje sa nezavisnom pobudom posle remonta

Miroslav Bjekić, Vojislav Vujičić, Marko Rosić, Marko Šućurović

***Apstrakt*— U radu je opisan postupak identifikacije parametara mašine jednosmerne struje sa nezavisnom pobudom posle izvršenog remonta. Snimljene su karakteristike praznog hoda generatora i mehaničke karakteristike motora za različite vrednosti priključnog napona, pobudne struje i dodate otpornosti u kolo indukta. Takođe su određeni i gubici usled obrtanja. Eksperimentalni rezultati potvrđeni su na dva načina koristeći merač momenta i elektromagnetnu kočnicu. Dobijeni koeficijenti elektromotorne sile (EMS) i momenta su upoređeni sa ranijim nazivnim vrednostima i dato je objašnjenje dobijenih razlika.**

***Ključne reči*— Mašina jednosmerne struje, identifikacija parametara, snimanje karakteristika**

I. UVOD

U laboratoriji za Električne mašine, pogone i automatiku - EMPA [1] na FTN u Čačku studenti IV godine modula Industrijska elektroenergetika studijskog programa Elektrotehničko i računarsko inženjerstvo izvode set vežbi iz predmeta Ispitivanje električnih mašina [2]. Programom predmeta se vrši ispitivanje mašine jednosmerne struje (JSS) i asinhrone mašine. Generacija studenata školske 2020/21 je dobila zadatak da ispita mašinu JSS posle remonta i da odredi njene nove parametre. Što tačnije određivanje parametara mašine dalje određuje kvalitet strujne i brzinske petlje odnosno dinamiku regulacije pogona sa mašinom JSS [3-5].

Naznačeni podaci ispitivane mašine JSS su sledeći:

U = 21,5 - 260 V
I_a = 17 - 17,4 A
n = 50 - 2741 o/min
P = 0,07 – 3,9 kW
J_{np} = 0,6 A, U_{np}=200 V
k_{TH} = 25 (Vmin)$^{-1}$

Na osnovu navedenih naznačenih vrednosti mogu se odrediti dva bitna parametra mašine JSS sa nezavisnom pobudom: konstanta momenta – k_M i konstanta EMS – k_e. Na osnovu izraza za moment (1) i naznačenih podataka mašine JSS

$$M = c\Phi I_a = k_M I_a \qquad M = 9{,}55 P/n \tag{1}$$

može se dobiti vrednost konstante momenta koji iznose:

$$k_{M,\,P_{max}} = 9{,}55 P/(I_a n) = 9{,}55\cdot 3900/(17{,}7\cdot 2741) = 0{,}7676\,\mathrm{Nm/A}$$

$$k_{M,\,P_{min}} = 9{,}55 P/(I_a n) = 9{,}55\cdot 70/(17\cdot 50) = 0{,}786\,\mathrm{Nm/A}$$

$$\boldsymbol{k_M \approx 0{,}78\,\mathrm{Nm/A}.}$$

Iz izraza za EMS:

$$E = U - R_a I_a \quad \text{gde je} \quad E = c\Phi\omega = k_e n \tag{2}$$

dobija se vrednost konstante EMS

$$k_e = (U - R_a I_a)/n = (260 - 0{,}8\cdot 17{,}7)/2741 = 0{,}0897\,\mathrm{Vmin}$$

$$\boldsymbol{k_e \approx 0{,}09\,\mathrm{Vmin}.}$$

Može se primetiti da između izračunatim koeficijentima ne važi međusobna zavisnost da je k_M = 9,55 k_e, što je i bio dodatni razlog da se studentima postavi zadatak da se laboratorijskim ispitivanjem mašine jednosmerne struje tačno utvrde njegovi novi parametri.

Teorijske osnove studenti mogu da razumeju korišćenjem i simulacionih programa za njih posebno kreiranih u programskom paketu GEOGEBRA [6, 7]. Primeri koji su realizovani u laboratoriji i prikazani u nastavku rada su takođe realizovani u ovom programskom paketu [8].

II. KORIŠĆENA OPREMA I ELEKTRIČNA ŠEMA

Električna šema povezivanja motora JSS, elektromagnetne kočnice (EMK) i merno-akvizicione opreme je na slici 1. Na slici se može uočiti da je mašina JSS povezana na dva nezavisna izvora napajanja JSS, tj. realizovana je nezavisna pobuda pri izvođenju eksperimenta. Struja pobude je merena pomoću ampermetra. Napon napajanja indukta meren je voltmetrom, dok se struja indukta I_a merena pomoću strujnog senzora i akvizicione kartice NI 6009. Za potrebe eksperimenta, tj. za snimanje jedne od karakteristika mašine u kolu indukta redno je povezivana i promenljiva otpornost R_{dod}. Mašina JSS je mahanički povezana preko merača momenta sa EMK kojom je mašina opterećivana. Sa merača momenta se dobija vrednost momenta M čiji se naponski signal meri akvizicionom karticom. Za napajanje EMK korišćen je promenljivi izvor JSS čija struja I_k je merena pomoću šant otpornika i akvizicione kartice. Tako izmerena struja korišćena je za dobijanje vrednosti kočnog momenta EMK. Na drugoj strani vratila mašine se nalazi tahogenerator (TG) pomoću kod se tokom eksperimenta meri brzina obrtanja mašine. Naponski signal tahogeneratora U_{th} se takođe meri pomoću akvizicione kartice. Za potrebe merenja i snimanja navedenih veličina napravljena je odgovarajuća aplikacija u programu LabVIEW.

Miroslav Bjekić – Fakultet tehničkih nauka u Čačku, Univerzitet u Kragujevcu, Svetog Save 65, 32000 Čačak, Srbija (e-mail: mbjekic@gmail.com).

Vojislav Vujičić – Fakultet tehničkih nauka u Čačku, Univerzitet u Kragujevcu, Svetog Save 65, 32000 Čačak, Srbija (e-mail: vojislav.vujicic@ftn.kg.ac.rs).

Marko Rosić – Fakultet tehničkih nauka u Čačku, Univerzitet u Kragujevcu, Svetog Save 65, 32000 Čačak, Srbija (e-mail: marko.rosic@ftn.kg.ac.rs).

Marko Šućurović – Fakultet tehničkih nauka u Čačku, Univerzitet u Kragujevcu, Svetog Save 65, 32000 Čačak, Srbija (e-mail: marko.sucurovic@ftn.kg.ac.rs).

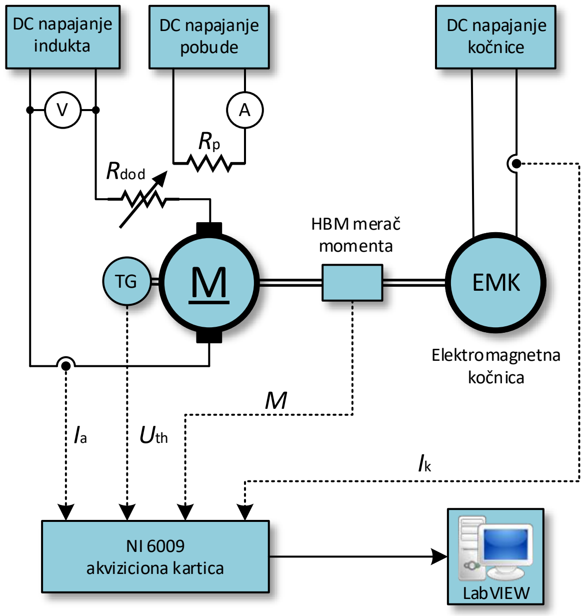

Sl. 1. Električna šema veze prilikom snimanja mehaničke karakteristike motora JSS sa nezavisnom pobudom

III. KARAKTERISTIKE GENERATORA JSS

A. *Baždarenje tahogeneratora*

Za potrebe merenja brzine obrtanja mašine korišćen je tahogenerator. Izvršeno je merenje napona na krajevima tahogeneratora za različite brzine obrtanja kako bi se dobila tačna vrednost njegove konstante (slika 2).

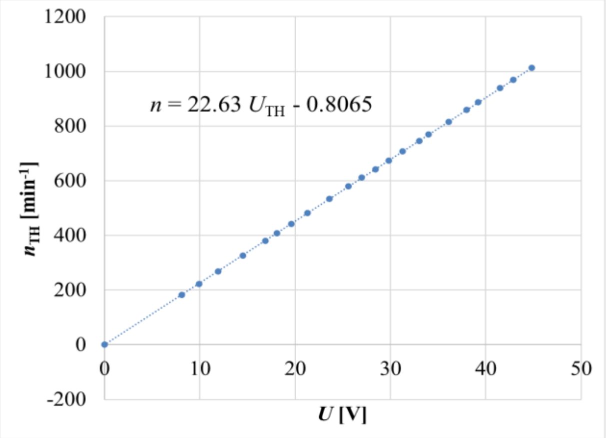

Sl. 2. Snimljena zavisnost brzine mašine JSS od napona na krajevima tahogeneratora

Dobijena je konstanta tahogeneratora od 22,63 (Vmin)$^{-1}$ koja je za 10,4% manja od naznačene vrednosti k_{TH}=25 (Vmin)$^{-1}$.

B. *Snimanje karakteristika praznog hoda*

Karakteristika praznog hoda je snimana stavljajući mašinu JSS u generatorski režim rada pokretanjem pomoću asinhrone mašine. Vršeno je snimanje karakteristike za tri brzine obrtanja: 997, 798 i 1196 o/min. Izvedena je interpolaciona funkcija zavisnosti napona praznog hoda od pobudne struje U_0= f(J) za brzinu 997 o/min. Znajući tu analitičku zavisnost moguće je pomoću proporcije dobiti je za bilo koju drugu brzinu. U ovom slučaju za brzine iznad i ispod osnovne krive polinom je množen je sa koeficijentom 0,8 i 1,2. Na slici 3 prikazane su izmerene vrednosti i interpolacione funkcije.

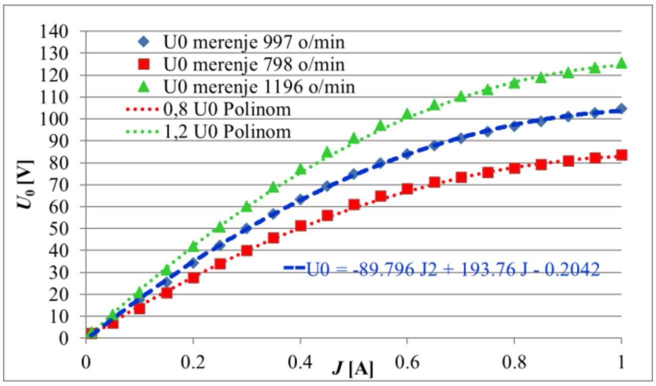

Sl. 3. Karakteristike praznog hoda generatora JSS sa nezavisnom pobudom i interpolirane funkcije za tri različite vrednosti pobudne struje

Na slici 3 se mogu uočiti odlična poklapanja krivih pa se zaključuje da se, sa dovoljnom preciznošću može usvojiti zavisnost napona praznog hoda (indukovane EMS) u funkciji pobudne stuje za konstantnu brzinu obrtanja kao:

$$U_0 = \left(-89,796J^2 + 193,76J - 0,2042\right) n \big/ 997 \tag{3}$$

odakle sledi da konstante $k_e = U_0/n$ za pobudne struje 0,6; 0,5 i 0,4 A iznose:

$$k_{\mathrm{e},\, J=0{,}6\mathrm{A}} = \left(-89,796\cdot 0,6^2 + 193,76\cdot 0,6 - 0,2042\right)\big/997 = \underline{0,084\,\mathrm{Vmin}}$$

$$k_{\mathrm{e},\, J=0{,}5\mathrm{A}} = \left(-89,796\cdot 0,5^2 + 193,76\cdot 0,5 - 0,2042\right)\big/997 = 0,075\,\mathrm{Vmin}$$

$$k_{\mathrm{e},\, J=0{,}4\mathrm{A}} = \left(-89,796\cdot 0,4^2 + 193,76\cdot 0,4 - 0,2042\right)\big/997 = 0,063\,\mathrm{Vmin}$$

Kao što je i očekivano, dobijene su tri različite vrednosti konstante EMS koja proporcionalno zavisi od jačine magnetnog fluksa koji stvara pobudni namotaj

$$E_\mathrm{a} = L_\mathrm{p}\, p' N' \big/ 60a' J\, n = k_\mathrm{e} n \tag{4}$$

gde je: L_p – induktivnost pobudnog navoja, p' – broj polova, N' – broj aktivnih provodnika navoja indukta, a' – broj paralelnih grana, J – pobudna struja i n – brzina obrtanja.

Na osnovu dobijenih koeficijenata i jednačine (4) se može odrediti veličina koja je srazmerna sa induktivnošću pobudnog namotaja C·L_p:

$$k_e \big/ J = L_p p' N' \big/ 60a' = C L_\mathrm{p} \;\Rightarrow\; C = p' N' \big/ 60a'. \tag{5}$$

Vrednosti veličine C·L_p za tri različite vrednosti pobudne struje su:

$$C L_{\mathrm{p},\, J=0{,}6\mathrm{A}} = k_{\mathrm{e},\, J=0{,}6\mathrm{A}} \big/ J = 0,084/0,6 = 0,14$$

$$C L_{\mathrm{p},\, J=0{,}5\mathrm{A}} = k_{\mathrm{e},\, J=0{,}5\mathrm{A}} \big/ J = 0,075/0,5 = 0,15$$

$$C L_{\mathrm{p},\, J=0{,}4\mathrm{A}} = k_{\mathrm{e},\, J=0{,}4\mathrm{A}} \big/ J = 0,063/0,4 = 0,1575$$

Dobijene vrednosti ukazuju na činjenicu da se sa povećanjem pobude ne dobija srazmerna vrednost magnetnog fluksa i da mašina ima nelinearnu karakteristiku magnećenja.

IV. KARAKTERISTIKE MOTORA JSS

A. *Određivanje konstante EMS motora JSS – k_e*

Prilikom snimanja mehaničke karakteristike motora JSS pomoću akvizicione opreme merene su sledeće veličine: pobudna struja – J, struja opterećenja – I, napon tahogeneratora – U_{th}, moment merenog pomoću merača momenta – M_{mer} i moment dobijen na osnovu merene vrednosti struje EMK – M_k.

Izvršena su merenja pri promeni:

a) Napona napajanja: U=100, 80 i 60 V
b) Dodate otpornosti u kolu indukta: R_{dod}=0, 15, 27 Ω
c) Pobudne struje: J=0,6, 0,5 i 0,4 A

Svi rezultati su obrađeni i prikazani grafički u nastavku rada.

a) Promena napona, pobudna struja J=0,6 A

Izmerene vrednosti brzine u funkciji struje indukta, za tri različita napona i pri konstantnoj struji pobude date su na slici 4.

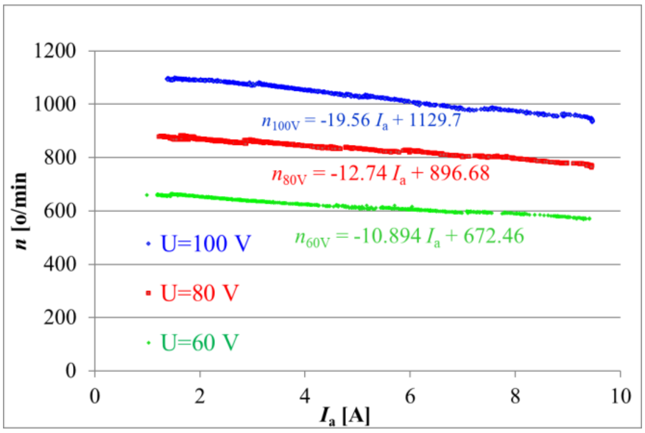

Sl. 4. Zavisnost napona motora od struje opterećenja pri različitim vrednostima priključnog napona

Analitički izraz zavisnosti brzine motora od struje opterećenja je:

$$n = \mathrm{f}(I_a) = n_0 - R_a I_a / k_e = U/k_e - R_a I_a / k_e \qquad (6)$$

odakle se na osnovu interpoliranih pravih čiji su izrazi prikazani na slici 4 dobija konstanta EMS:

$$k_{e,\,U=100\mathrm{V}} = 100/1129{,}7 = 0{,}088519 \approx \underline{0{,}089\,\mathrm{Vmin}}$$
$$k_{e,\,U=80\mathrm{V}} = 80/896{,}68 = 0{,}089218 \approx \underline{0{,}089\,\mathrm{Vmin}}$$
$$k_{e,\,U=60\mathrm{V}} = 60/672{,}46 = 0{,}089224 \approx \underline{0{,}089\,\mathrm{Vmin}}$$

b) Dodavanje otpora u kolo indukta, U=100 V, J=0,6 A

Izmerene vrednosti brzine u funkciji struje indukta, za tri različite vrednosti dodatih otpora u kolo indukta, pri konstantnom naponu i struji pobude date su na slici 5.

Iz prikazanih interpolacionih funkcija (slika 5) može se odrediti konstanta EMS:

$$k_{e,\,Rdod=0\Omega} = 100/1129{,}7 = 0{,}08852 \approx \underline{0{,}089\,\mathrm{Vmin}}$$
$$k_{e,\,Rdod=15\Omega} = 100/1107{,}8 = 0{,}09027 \approx \underline{0{,}09\,\mathrm{Vmin}}$$
$$k_{e,\,Rdod=27\Omega} = 100/1111{,}6 = 0{,}08996 \approx \underline{0{,}09\,\mathrm{Vmin}}$$

Dobijene vrednosti potvrđuju da konstanta EMS ne zavisi od dodate vrednosti otpora u kolo indukta. Ove tri podjednake vrednosti potvrđuju tačnost izvršenog merenja.

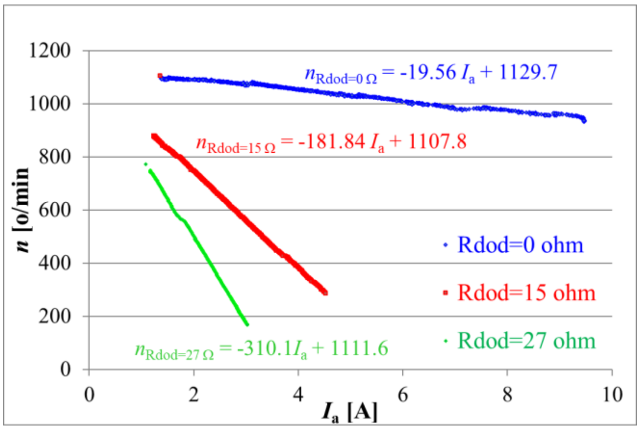

Sl. 5. Zavisnost napona motora od struje opterećenja pri različitim vrednostima dodate otpornosti u kolo indukta

c) Promena pobudne struje, U=100 V

Izmerene vrednosti brzine u funkciji struje indukta, za tri različite vrednosti struje pobude i pri konstantnom naponu date su na slici 6.

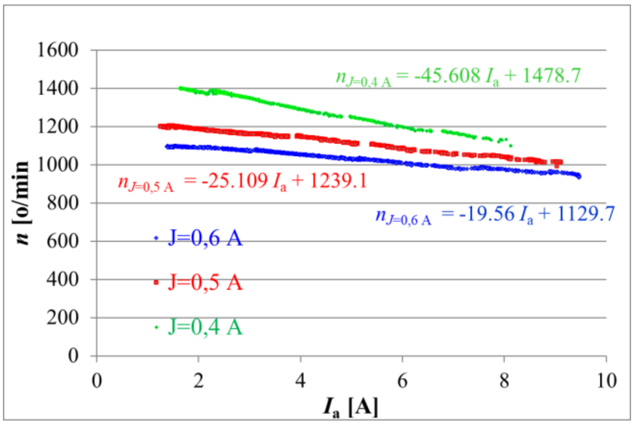

Sl. 6. Zavisnost napona motora od struje opterećenja pri različitim vrednostima pobudne struje

Na osnovu dobijenih interpolacionih pravih dobijaju se sledeće vrednosti konstante EMS:

$$k_{e,\,J=0{,}6\mathrm{A}} = 100/1129{,}7 = 0{,}088519 \approx \underline{0{,}089\,\mathrm{Vmin}}$$
$$k_{e,\,J=0{,}5\mathrm{A}} = 100/1239{,}1 = 0{,}08070 \approx 0{,}081\,\mathrm{Vmin}$$
$$k_{e,\,J=0{,}4\mathrm{A}} = 100/1478{,}7 = 0{,}06763 \approx 0{,}068\,\mathrm{Vmin}$$

Iz izračunatih vrednosti može se primetiti da sa povećanjem pobudne struje se povećava i konstantna EMS motora pošto je direktno srazmerna sa magnetnim fluksom koji stvara pobuda. Ako se ova konstantna podeli sa pobudnom strujom dobija se vrednost srazmerna sa induktivnošću pobudnog namotaja:

$$C\,L_{p,\,J=0{,}6\mathrm{A}} = k_{e,\,J=0{,}6\mathrm{A}}/J = 0{,}089/0{,}6 = 0{,}148$$
$$C\,L_{p,\,J=0{,}5\mathrm{A}} = k_{e,\,J=0{,}5\mathrm{A}}/J = 0{,}081/0{,}5 = 0{,}162$$
$$C\,L_{p,\,J=0{,}4\mathrm{A}} = k_{e,\,J=0{,}4\mathrm{A}}/J = 0{,}068/0{,}4 = 0{,}17$$

B. *Određivanje konstante momenta motora JSS – k_M*

Za određivanje konstante momenta jednosmernog motora neophodno je obezbediti što tačnije merenje momenta. Ono je izvršeno na dva načina:

- Pomoću merača momenta i
- Pomoću baždarene EMK [9].

Na slici 7 prikazana oprema korišćena za realizaciju snimanja mehaničkih karakteristika motora JSS. Motor JSS (1) je spregnut sa EMK (2) preko merača momenta HBM T22/50NM (3) pomoću kog se direktno meri moment. EMK se napaja sa izvora JSS (4) čija struja određuje kočni moment. Struja kočenja je merena pomoću šant otpornika od 10 Ω (5). Na akvizicionu karticu NI 6009 (6) povezani su merni (naponski) signali sa tahogeneratora (7) za merenje brzine, zatim sa senzora Ametes CS10A-02 (8) za merenje struje indukta, sa priključne kutije merača momenta (9) za vrednost momenta, i sa šant otpornika za merenje struje kočenja (5). Od ostale opreme, na slici 7 prikazani su: promenljivi otpornik dodavan u kolo indukta (10), voltmetar za merenje napona napajanja motora JSS (11), ampermetar (12) za merenje struje pobude i ispravljačko kolo (13) za napajanje kola indukta.

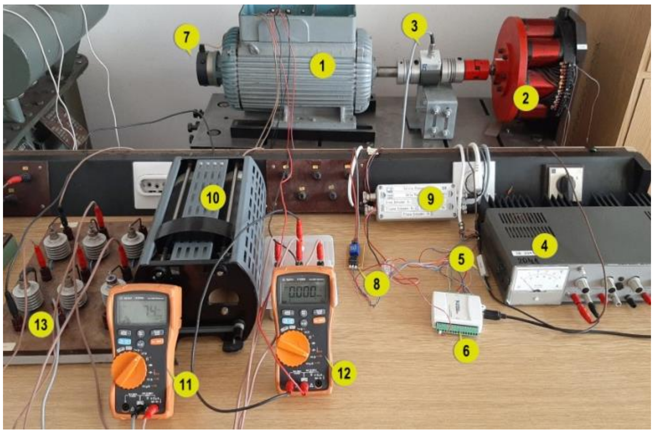

Sl. 7. Oprema korišćena za merenje mehaničke karakteristike motora JSS

Povezivanjem na akvizicionu karticu, izvršeno je podešavanje analognih naponskih ulaza u okviru softvera LabVIEW, nakon čega je kreirana aplikacija za snimanje signala.

Pored direktnog merenja elektromagnetnog momenta pomoću HBM merača momenta iskorišćena je i EMK koja je imala dvostruku funkciju:

- da se pomoću nje kontrolisano opterećuje motor JSS, i
- da se pomoću poznate karakteristike EMK dođe do vrednosti elektromagnetnog momenta motora znajući analitičku zavisnost kočnog momenta u funkciji brzine obrtanja diska i struje kočnice [9]:

$$M_{\mathrm{k}} = \mathrm{f}(n) = A \cdot e^{(B \cdot n)} + C \cdot e^{(D \cdot n)} \tag{7}$$

$$\begin{aligned} A &= A_1 \cdot I_{\mathrm{k}}^3 + A_2 \cdot I_{\mathrm{k}}^2 + A_3 \cdot I_{\mathrm{k}} + A_4 \\ B &= B_1 \cdot I_{\mathrm{k}}^3 + B_2 \cdot I_{\mathrm{k}}^2 + B_3 \cdot I_{\mathrm{k}} + B_4 \\ C &= C_1 \cdot I_{\mathrm{k}}^3 + C_2 \cdot I_{\mathrm{k}}^2 + C_3 \cdot I_{\mathrm{k}} + C_4 \\ D &= D_1 \cdot I_{\mathrm{k}}^3 + D_2 \cdot I_{\mathrm{k}}^2 + D_3 \cdot I_{\mathrm{k}} + D_4 \end{aligned} \tag{8}$$

Izračunate vrednosti koeficijenta polinoma napisane u matričnom obliku za određivanje kočnog momenta kočnice iznose [9]:

$$\begin{bmatrix} A_1 & B_1 & C_1 & D_1 \\ A_2 & B_2 & C_2 & D_2 \\ A_3 & B_3 & C_3 & D_3 \\ A_4 & B_4 & C_4 & D_4 \end{bmatrix} = \begin{bmatrix} -4,741 & -0,003162 & 3,528 & -0,03787 \\ 26,41 & 0,007258 & -24,95 & 0,01937 \\ 2,245 & -0,007258 & -2,747 & 0,004357 \\ -0,2562 & 0,001099 & 0,3187 & -0,0072 \end{bmatrix}$$

Pomoću datih koeficijenata dobijaju se mehaničke karakteristike za bilo koju struju kočenja iz mernog opsega brzine obrtanja kočnice.

Rezultati merenja elektromagnetnog momenta pomoću merača momenta (M_{senzor}) i posredno – preko poznatih parametara EMK ($M_{\text{kočnica}}$) su prikazani na slikama:

a) promeni napona, slika 8
b) dodavanje otpora u kolo indukta, slika 9, i
c) promeni pobudne struje, slika 10.

a) Promena napona, pobudna struja J=0,6 A

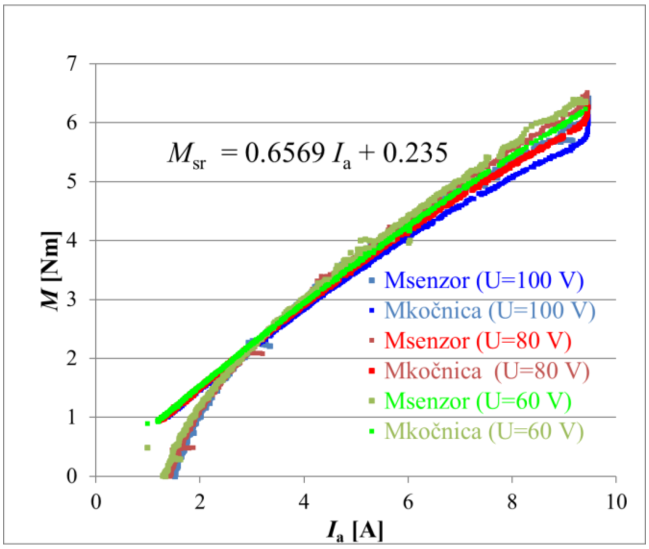

Sl. 8. Zavisnost momenta motora od struje opterećenja pri različitim vrednostima priključnog napona

Na osnovu grafički prikazanih vrednosti momenta (slika 8) za tri različita napona napajanja dobijena je srednja vrednost funkcije mehaničke karakteristike. Iz izraza za moment:

$$M = k_{\mathrm{M}} I_{\mathrm{a}} \Rightarrow k_{\mathrm{M}} = M / I_{\mathrm{a}} \tag{9}$$

Dobijena je srednja vrednost konstante EMS koja iznosi

$$k_{\mathrm{M,\,sr}} = 0{,}6569.$$

Analizirajući prikazane vrednosti izmerenog momenta može se zaključiti sledeće:

- Dobijeni rezultati pokazuju zadovoljavajuća poklapanja između rezultata merenja elektromagnetnog momenta pomoću merača momenta i posredno preko EMK. Time je još jednom potvrđena zadovoljavajuća tačnost posredno izračunate vrednosti momenta preko brzine obrtanja i struje kočnice;

- Vrednost promenljivog priključnog napona nije ni trebala da utiče na oblik dobijenih krivih, kao što i prikazane krive pokazuju;
- Vrednosti momenata dobijenih pomoću EMK za male vrednosti struja odstupaju od linearnog oblika, što se i očekivalo znajući, ranije utvrđen, merni opseg kočnice [9];
- Može se uočiti da krive ne polaze iz koordinatnog početka, već da imaju određenu vrednost momenta za struju indukta I_a=0. Ova vrednost ne može da se dobije merenjem, pošto u režimu praznog hoda, tj. neopterećene mašine, postoji određena struja indukta kojom se pokrivaju gubici usled obrtanja.

Sve su to razlozi zbog kojih postoji neslaganje između, na početku rada izračunate vrednosti konstante momenta motora i izmerenih vrednosti momenta. Zaključak je da se za motor JSS ne može primeniti zavisnost $M=k_mI$ i da naznačene vrednosti važe za naznačene radne režime.

Neslaganja između naznačenih i merenih vrednosti se mogu tumačiti i činjenicom da je mašina bila remontovana, pa se moglo očekivati i da su joj fabrički naznačene vrednosti promenjene.

b) Dodavanjem otpora u kolo indukta, U=100 V, J=0,6 A

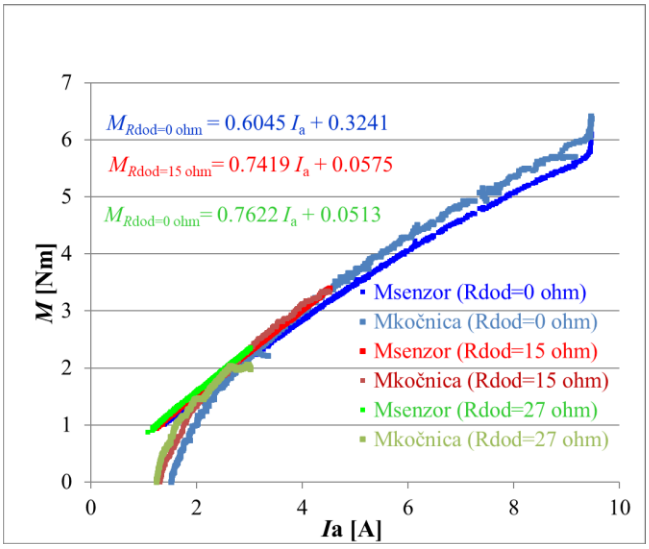

Sl. 9. Zavisnost momenta motora od struje opterećenja pri različitim vrednostima dodane otpornosti u kolu indukta

Dobijene vrednosti konstante momenta motora JSS za dodate vrednosti otpornosti u kolo indukta (slika 9) pokazuju da su koeficijenti za slučaj dodavane otpornosti u kolo indukta približne vrednosti k_M=0,75 Nm/A što se poklapa sa, na početku rada, izračunatom konstantom momenta na osnovu naznačenih vrednosti (0,78 Nm/A). Ovo poklapanje ukazuje da je potrebno posebno obratiti pažnju na otpornost kola indukta i izvršiti dodatna ispitivanja, što će biti tema budućeg rada.

c) Promena pobudne struje, U=100 V

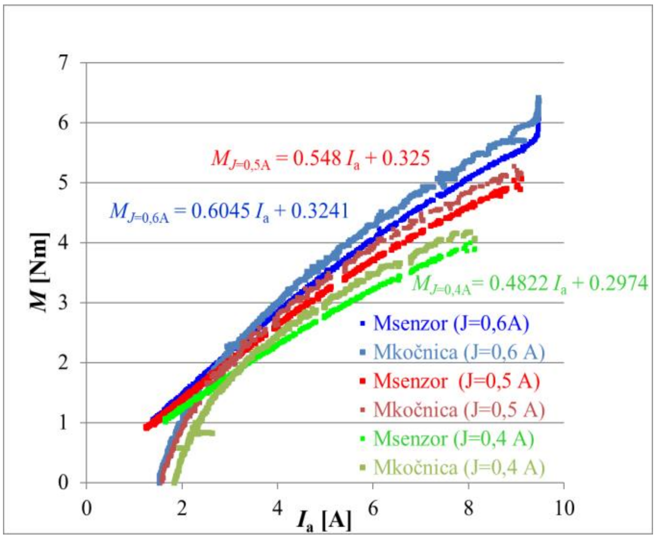

Sl. 10. Zavisnost momenta motora od struje opterećenja pri različitim vrednostima pobudne struje

Sa grafika datih na slici 10 određene su vrednosti koeficijenta pravca mehaničkih karakteristika koje za pojedine pobudne struje iznose:

$$k_{\text{M},\ J=0,6\text{A}} = 0,6045$$
$$k_{\text{M},\ J=0,5\text{A}} = 0,548$$
$$k_{\text{M},\ J=0,4\text{A}} = 0,4822$$

pomoću kojih se može odrediti i induktivnost pobude:

$$L_{\text{p},\ J=0,6\text{A}} \sim k_{\text{M},J=0,6\text{A}}/9,55J = 0,6045/9,55\cdot 0,6 = 0,105$$
$$L_{\text{p},\ J=0,5\text{A}} \sim k_{\text{M},J=0,5\text{A}}/9,55J = 0,548/9,55\cdot 0,5 = 0,116$$
$$L_{\text{p},\ J=0,4\text{A}} \sim k_{\text{M},J=0,4\text{A}}/9,55J = 0,4822/9,55\cdot 0,4 = 0,126.$$

Ovako dobijene induktivnosti potvrđuju činjenicu da je magnetno kolo mašine JSS nelinearno i da sa povećanjem pobude se smanjuje induktivnost (mašina ulazi u zasićenje).

Pošto su dobijene procenjene vrednosti induktivnosti na tri različita načina: preko karakteristike praznog hoda, mehaničke karakteristike n=f(I_a) i n=f(M), sve vrednosti su zajedno prikazane u tabeli I.

TABELA I
INDUKTIVNOSTI POBUDNOG NAMOTAJA

C L_p [H]	J=0,6 A	J=0,5 A	J=0,4 A
K-ka U_0=f(J)	0,14	0,15	0,16
K-ka n=f(I_a)	0,15	0,16	0,17
K-ka M=f(I_a)	0,11	0,12	0,13

Na slici 11 prikazane su zavisnosti gubitaka i momenta usled obrtanja za tri različite vrednosti pobudne struje. Čime je potvrđeno da se zavisnost elektromagnetnog momenta ne može izraziti kao linearna funkcija struje indukta, već ima složeniji oblik.

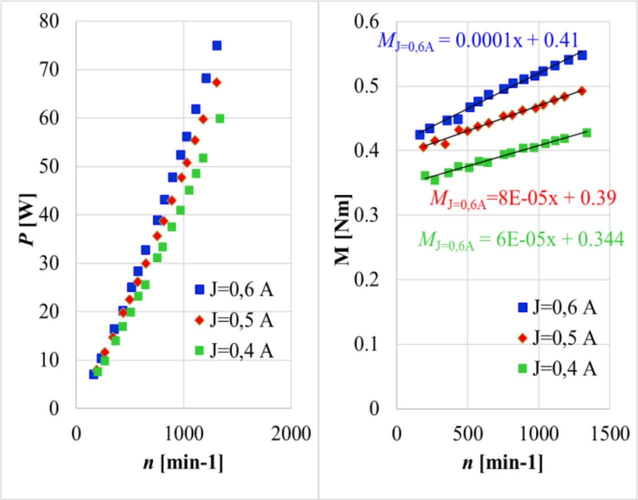

Sl. 11. Snimljene karakteirstike gubitaka usled obrtanja i momenta usled obrtanja za različite vrednosti pobudne struje

V. ZAKLJUČAK

U radu je izvšena identifikacija parametara mašine JSS posle izvšenog remonta. Najznačajniji parametar koji je trebalo eksperimentalnim putem dobiti i proveriti u odnosu na naznačene vrednosti je konstanta EMS i konstanta momenta k_M. Ona su izračunate obrađujući rezultate merenja u ogledu praznog hoda i ogledu snimanja mehaničke karakteristike motora JSS sa nezavisnom pobudom, za 3 načina prilagođenja karakteristike motora (promenom napona, slabljenjem polja i dodavanjem otpornosti.

Utvrđeno je da postoje neslaganja između, na početku rada izračunate vrednosti konstante EMS i konstante momenta motora jednosmerne struje preko naznačenih parametara i izmerenih vrednosti. U radu je potvrđeno da se moment motora ne može za ceo radni opseg predstaviti kao linearna zavisnost struje opterećenja ($M \neq k_M I_a$) i da se preciznija zavisnost dobija uzimanjem u obzir gubitaka usled obrtanja i momenta koji postoji i u režimu praznog hoda.

Takođe, u radu je potvrđena tačnost postupka određivanja momenta motora preko parametara elektromagnetne kočnice (struje i brzine) kojom se kontrolisano opterećuje.

ZAHVALNICA

Istraživanja prezentovana u ovom radu su delimično finansirana sredstvima Ministarstva prosvete, nauke I tehnološkog razvoja RS, ugovor br. 451-03-9/2021-14/200132 čiji je realizator Fakultet tehničkih nauka u Čačku – Univerziteta u Kragujevcu.

LITERATURA

[1] Sajt Laboratorije za električne mašine, pogone i automatiku – FTN u Čačku: www.empa.ftn.kg.ac.rs

[2] Sajt predmeta Ispitivanje električnih mašina – Laboratorija EMPA, FTN u Čačku: http://www.empa.ftn.kg.ac.rs/osnovne-studije/ispitivanje-elektricnih-masina.php

[3] M. Rosić, S. Antić, M. Bjekić, V. Vujičić, "Educational laboratory setup of DC motor cascade control based on dSPACE1104 platform", Proceedings of 5th International Conference on Renewable Electrical Power Sources - ICREPS2017, vol. 5 no. 1, pp. 213-222, DOI:10.24094/mkoiee.017.5.1.213, Belgrade, Serbia, 12-13 October, 2017.

[4] D. T. Liem and K. K. Ahn, "DC motor parameters identification and sensorless torque estimation using Fuzzy PID," 2012 12th International Conference on Control, Automation and Systems, 2012, pp. 76-81.

[5] S. S. Saab, R. Abi Kaed-Bey, "Parameter Identification of a DC Motor: An Experimental Approach", ICECS 2001. 8th IEEE International Conference on Electronics, Circuits and Systems. Malta, 2-5 Sept. 2001.

[6] Spisak autora i programa koji su kreirali softvere u GEOGEBRI iz oblasti Električne mašine i pogoni. Dostupno na: www.empa.ftn.kg.ac.rs/razno/GEOGEBRA_ELEKTRICNE_MASINE.html

[7] M. Bjekic, Kreirani programi u GEOGEBRI. Dostupno na: https://www.geogebra.org/u/mbjekic

[8] DC motor separate exited, https://www.geogebra.org/m/m2mwpeja

M. Bjekić, M. Božić, M. Rosić, M. Šućurović, „Elektromagnetna kočnica sa jednim obrtnim diskom za laboratorijska ispitivanja električnih motora", Tehničko rešenje, Fakultet tehničkih nauka u Čačku, 2015. Dostupno na: http://www.ftn.kg.ac.rs/docs/resenja/EM_kocnica.pdf

ABSTRACT

The paper describes identification process of separately excited DC machine parameters after the machine repair was performed. Mechanical and no load characteristics of DC machine are recorded with different values of armature voltages, excitation current and added resistance in the armature circuit. Rotational and ventilation losses of the machine are determined as well. Experimental results are confirmed in two ways: using torque sensor and using calibrated electromechanical brake. Machine EMF and torque coefficients are compared with previous rated machine values after which a proper discussion of obtained differences was given.

Separately excited DC machine parameters identification after the machine repair

M. Bjekic, V. Vujicic, M. Rosic, and M. Sucurovic

Simulacija histerezisnih petlji interpolacijom harmonijskih komponenti magnetskog polja

Srđan Divac, Branko Koprivica

***Apstrakt*—Cilj ovog rada je prikaz postupka simulacije histerezisnih petlji feromagnetskog uzorka koja je sprovedena simulacijom vremenskih oblika jačine magnetskog polja (u nastavku magnetskog polja) i magnetske indukcije. Podaci za magnetsko polje i indukciju su dobijeni merenjem, pri kontrolisanom obliku magnetske indukcije, za dva razmatrana oblika - sinusni i trougaoni. Na osnovu izmerenih podataka su određeni harmonici magnetskog polja za poznate amplitude magnetske indukcije. Nove vrednosti ovih harmonika se određuju interpolacijom prethodno izračunatih vrednosti, za amplitudu magnetske indukcije od interesa. Na osnovu ovih harmonika se vrši simulacija novog vremenskog oblika magnetskog polja. Nova histerezisna petlja se simulira korišćenjem ovog magnetskog polja i nove simulirane magnetske indukcije odgovarajućeg oblika. U radu je opisan navedeni postupak simulacije, dato je poređenje interpoliranih i izračunatih amplituda harmonika i vremenskih oblika magnetskog polja, kao i histerezisnih petlji. Takođe, u radu je data odgovarajuća analiza i diskusija rezultata.**

***Ključne reči* — Magnetsko polje; Histerezisna petlja; Harmonijska analiza; Interpolacija; Simulacija.**

I. UVOD

Modelovanje ili simulacija procesa magnećenja feromagnetskog uzorka zahteva veliki broj izmerenih podataka od značaja za dati proces [1-8], kako bi se odredili parametri modela (Preisach [1], Jiles-Atherton [2], Tellinen [3], Milovanović-Koprivica [4] i drugi) ili izvršilo treniranje neuronske mreže [6-7]. Proces magnećenja feromagnetskog materijala se može uspešno modelovati pomoću harmonijskih komponenti [9]. Određivanje parametara modela, treniranje neuronske mreže i drugi simulacioni postupci su neretko zahtevni u matematičkom i vremenskom pogledu. Dodatno, njihova tačnost i mogućnosti šire primene su ograničeni. Za prevazilaženje navedenih problema su potrebni alternativni postupci simulacije magnetskih veličina i histerezisa.

U ovom radu izložen je jedan alternativni postupak simulacije histerezisnih petlji baziran na interpolaciji amplituda i faza konačnog broja harmonika izmerenih magnetskih polja za magnetsku indukciju poznatog oblika i amplitude.

Podaci potrebni za proračun dobijeni su merenjem magnetskog polja i indukcije torusnog uzorka, napravljenog od orijentisanog feromagnetskog lima, primenom merne metode bazirane na personalnom računaru [10]. Pri merenjima su korišćena dva oblika magnetske indukcije - sinusni i trougaoni. U kontrolisanom merenju su postignute amplitude u opsegu od 0,2 T do 1,6 T sa korakom od 0,2 T, za oba razmatrana oblika. Merni podaci za verifikaciju rezultata proračuna dobijeni su pri istim oblicima magnetske indukcije za amplitude 0,5 T, 0,9 T i 1,5 T.

U radu su predstavljene izmerene histerezisne petlje za oba razmatrana oblika magnetske indukcije, kao i amplitude i faze harmonika odgovarajućih magnetskih polja. Takođe, prikazana su poređenja interpoliranih i izračunatih amplituda harmonika magnetskih polja, vremenskih oblika magnetskog polja i histerezisnih petlji za sve razmatrane slučajeve. Izvršena je analiza odstupanja amplituda harmonika i površina histerezisnih petlji i mogućnosti primene predloženog simulacionog postupka, uz odgovarajuću diskusiju.

II. SIMULACIONI POSTUPAK

Magnetsko polje $H(t)$ je fizička veličina koja se može predstaviti pomoću neparnih harmonijskih komponenti u obliku sume konačnog broja harmonika [11], i to:

$$H(t) = \sum_{i=1}^{N} \left(H_i \cos\left((2i-1)\omega t + \alpha_i \right) \right), \tag{1}$$

gde su H_i i α_i amplituda i faza i-tog harmonika, respektivno, i je red harmonika, N je najviši red, ω je kružna učestanost osnovnog harmonika i t je vreme.

Simulacija histerezisne petlje od značaja izvodi se kroz postupak sa sledećim koracima:

1. proračun N amplituda i faza neparnih harmonika izmerenih magnetskih polja za odgovarajući opseg amplituda magnetske indukcije,
2. interpolacija novih amplituda i faza harmonika polja za amplitude magnetske indukcije od interesa,
3. proračun vremenskog oblika magnetskog polja primenom (1) i simulacija vremenskog oblika magnetske indukcije i
4. simulacija histerezisnih petlji na osnovu rezultata iz prethodnog koraka.

III. MERNA METODA I APARATURA

Vremenski oblici magnetskog polja i indukcije dobijeni su primenom metode merenja bazirane na personalnom računaru i akviziciji podataka [10]. Merenja su sprovedena sa namotanim torusnim uzorkom od feromagnetskog lima oznake 27PH100, proizvođača POSCO. Blok šema merno-akvizicionog sistema je prikazana na Sl. 1.

Srđan Divac – Fakultet tehničkih nauka u Čačku, Univerzitet u Kragujevcu, Svetog Save 65, 32000 Čačak, Srbija, (e-mail: divacsrdjan@gmail.com) – Student doktorskih studija - Stipendista Ministarstva.

Branko Koprivica – Fakultet tehničkih nauka u Čačku, Univerzitet u Kragujevcu, Svetog Save 65, 32000 Čačak, Srbija, (e-mail: branko.koprivica@ftn.kg.ac.rs).

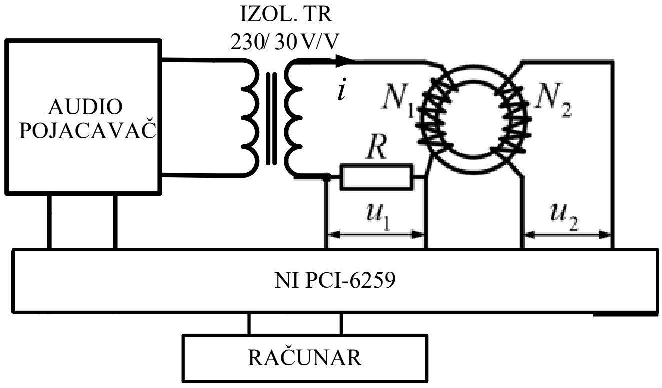

Sl. 1. Blok šema merno-akvizicionog sistema za merenje magnetskih karakteristika.

Merno-akvizicioni sistem se sastoji od naponski kontrolisanog izvora naizmeničnog napona, šant otpornika od R=0,5 Ω, torusnog uzorka, akvizicione kartice i računara.

Naponski kontrolisan izvor čini audio pojačavač CROWN XLi 2500 i izolacioni transformator 230/30 V/V, zajedno sa analognim izlazom akvizicione kartice NI PCI-6259. Ova kartica se koristi i za merenje napona u_1 na šant otporniku i indukovanog napona u_2 na krajevima indukcionog namotaja torusnog uzorka. Za potrebe merenja napravljena je aplikacija u programskom paketu LabVIEW koja vrši obradu i čuvanje izmerenih podataka. Takođe, ova aplikacija se koristi za kontrolu vremenskog oblika magnetske indukcije, određene na osnovu izraza (3) - integrala po vremenu izmerenog napona u_2, prema zadatom vremenskom obliku indukcije. Kontrola amplitude i oblika magnetske indukcije je sprovedena uspostavljanjem digitalne (programske) povratne sprege [12]. Kroz iterativni postupak kontrole se menja napon izvora sve dok se ne ostvari zadati vremenski oblik indukcije.

Merenje napona u_1 i u_2 je realizovano sa 1000 mernih podataka po periodi signala. Sve ostale veličine koje se računaju na osnovu ovih napona takođe sadrže ovaj broj podataka.

Struja $i(t)$ kroz pobudni namotaj meri se indirektno, kao količnik izmerenog napona šant otpornika u_1 i njegove otpornosti R. Ova struja se koristi za proračun trenutne vrednosti magnetskog polja prema Amperovom zakonu [13]:

$$H(t) = \frac{N_1 i(t)}{l} \quad \left[\frac{\mathrm{A}}{\mathrm{m}}\right], \tag{2}$$

gde je N_1 broj navojaka pobudnog namotaja, a l dužina srednje linije jezgra.

Napon u_2 koji se indukuje na indukcionom namotaju torusnog uzorka proporcionalan je brzini promene ukupnog fluksa u jezgru, a magnetska indukcija se može proračunati pomoću izraza:

$$B(t) = \frac{1}{N_2 A}\int_0^t u_2(\tau)\,\mathrm{d}\tau \quad [\mathrm{T}], \tag{3}$$

gde je N_2 broj navojaka indukcionog namotaja i A je površina poprečnog preseka jezgra.

Podaci o broju pobudnih i indukcionih navojaka, dužini srednje linije i površini poprečnog preseka jezgra su dati u Tabeli I.

TABELA I
PODACI O TORUSNOM UZORKU

Veličina	Vrednost
N_1	175
N_2	60
l [m]	0,306
A [mm^2]	102,80

IV. REZULTATI MERENJA

Rezultati merenja su prikazani u obliku histerezisnih petlji. Na Sl. 2 su prikazane histerezisne petlje dobijene merenjima pri kontrolisanoj magnetskoj indukciji sinusnog i trougaonog oblika, respektivno. Merenja su izvršena pri frekvenciji od 50 Hz za opseg magnetskih indukcija amplituda od 0,2 T do 1,6 T sa korakom od 0,2 T. Takođe, isprekidanom linijom su prikazane i histerezisne petlje za verifikaciju simulacije za amplitude magnetske indukcije od 0,5 T, 0,9 T i 1,5 T.

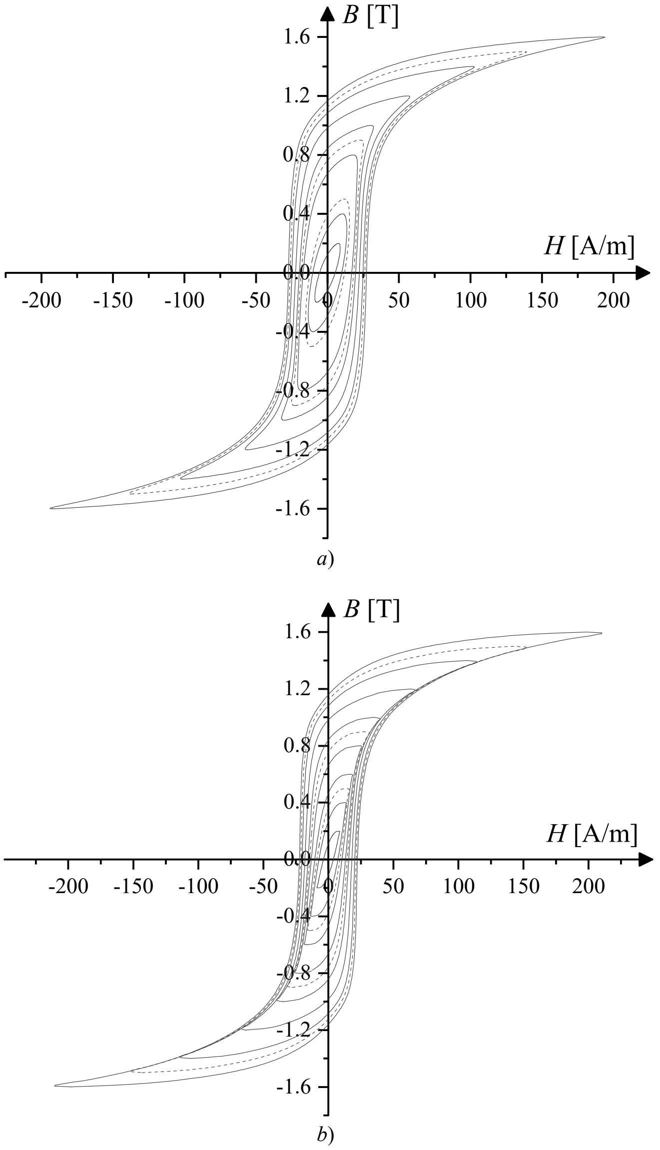

a)

b)

Sl. 2. Izmerene histerezisne petlje pri *a*) sinusnom i *b*) trougaonom obliku magnetske indukcije.

V. REZULTATI PRORAČUNA I ANALIZA

Na Sl. 3 i 4 su prikazani rezultati proračuna harmonijskih komponenti magnetskog polja dobijenih merenjima.

Na Sl. 3 je prikazana promena amplituda i faza harmonika magnetskog polja za magnetsku indukciju oblika sinusoide. Od prikazanih N=9 amplituda, koliko je od značaja za veće amplitude magnetske indukcije, samo 3 do 5 amplituda ima vrednost veću od 1 % od osnovnog harmonika. Shodno tome, radi preglednijeg prikaza, sa Sl. 3*b* su ukonjene faze viših harmonika, koje značajno osciluju, a koje nemaju veći uticaj na konačnu vrednost magnetskog polja.

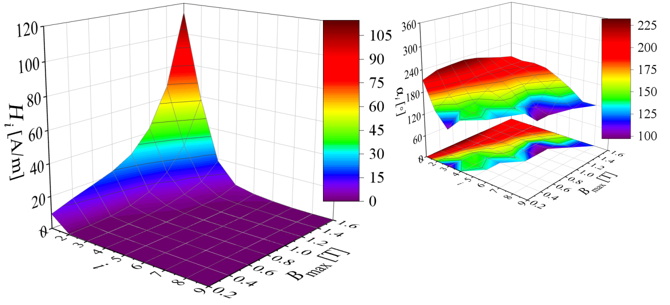

a) *b*)

Sl. 3. Promena *a*) amplituda i *b*) faza harmonika magnetskog polja pri sinusnom obliku magnetske indukcije.

Na Sl. 4 je prikazana promena amplituda i faza harmonika magnetskog polja za magnetsku indukciju trougaonog oblika. Prikazano je N=20 amplituda i redukovani broj faza harmonika.

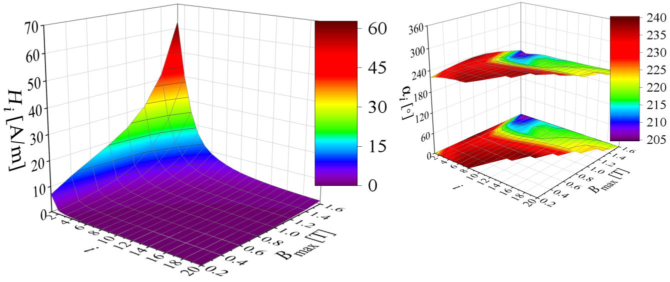

a) *b*)

Sl. 4. Promena *a*) amplituda i *b*) faza harmonika magnetskog polja pri trougaonom obliku magnetske indukcije.

Proračun harmonijskih komponenti magnetskog polja metodom interpolacije izvršen je za amplitude magnetske indukcije od 0,5 T, 0,9 T i 1,5 T. Usvojena vrednost najvišeg reda neparnih harmonika je N=15, za magnetsku indukciju sinusnog, i N=75, za magnetsku indukciju trougaonog oblika. Vrednosti za N usvojene su prema kriterijumu najmanjih oscilacija u vremenskom obliku magnetskog polja izračunatog primenom (1). Povećanje vrednosti N iznad usvojenih ne doprinosi značajnijem poboljšanju rezultata, a zadovoljavajući rezultati (sa minimalnim oscilacijama) se postižu i sa dva puta manjim brojem harmonika. Proračun harmonika je izvršen u programskom paketu *Mathematica* primenom funkcije *Fourier*, a interpolacija primenom funkcije *Interpolation*, čijom primenom se ceo postupak sprovodi bez dodatnog programiranja složenih matematičkih proračuna. Vremenski oblik magnetske indukcije je simuliran u istom programu kao idealna sinusna ili trougaona funkcija. Svaki signal je predstavljen nizom vrednosti sa ukupno 1000 članova niza. Deo korišćenog programskog koda koji pokazuje kako su određeni harmonici polja i kako je izvršena njihova interpolacija je dat u Dodatku.

U Tabelama II i III date su vrednosti prvih N=5 amplituda harmonika magnetskog polja dobijenih interpolacijom $H_{i,\mathrm{i}}$ i njihova odstupanja $\Delta H_{i\text{-}0,5}$, $\Delta H_{i\text{-}0,9}$ i $\Delta H_{i\text{-}1,5}$ od izračunatih amplituda harmonika izmerenih magnetskih polja H_i, gde je $\Delta H_i = H_{i,\mathrm{i}} - H_i$. Amplitude i odstupanja su dati za oba razmatrana oblika magnetske indukcije. Na osnovu rezultata prikazanih u Tabelama II i III je zaključeno da opisani postupak interpolacije harmonika ima zadovoljavajuću tačnost. Shodno tome, moguće je izvršiti simulaciju magnetskog polja korišćenjem izraza (1).

TABELA II

AMPLITUDE HARMONIKA MAGNETSKOG POLJA DOBIJENE INTERPOLACIJOM I NJIHOVA ODSTUPANJA OD AMPLITUDA DOBIJENIH IZRAČUNAVANJEM PRI MAGNETSKOJ INDUKCIJI SINUSNOG OBLIKA

i	$H_{i,\mathrm{i}\text{-}0,5}$ [A/m]	$H_{i,\mathrm{i}\text{-}0,9}$ [A/m]	$H_{i,\mathrm{i}\text{-}1,5}$ [A/m]	$\Delta H_{i\text{-}0,5}$ [A/m]	$\Delta H_{i\text{-}0,9}$ [A/m]	$\Delta H_{i\text{-}1,5}$ [A/m]
1	16,08	25,42	86,78	0,00	−0,07	0,09
2	0,86	4,93	41,51	0,00	−0,05	−0,03
3	0,16	1,29	12,23	0,02	−0,02	−0,07
4	0,03	0,27	2,84	0,01	0,02	−0,08
5	0,02	0,10	1,38	0,01	0,02	−0,03

TABELA III

AMPLITUDE HARMONIKA MAGNETSKOG POLJA DOBIJENE INTERPOLACIJOM I NJIHOVA ODSTUPANJA OD AMPLITUDA DOBIJENIH IZRAČUNAVANJEM PRI MAGNETSKOJ INDUKCIJI TROUGAONOG OBLIKA

i	$H_{i,\mathrm{i}\text{-}0,5}$ [A/m]	$H_{i,\mathrm{i}\text{-}0,9}$ [A/m]	$H_{i,\mathrm{i}\text{-}1,5}$ [A/m]	$\Delta H_{i\text{-}0,5}$ [A/m]	$\Delta H_{i\text{-}0,9}$ [A/m]	$\Delta H_{i\text{-}1,5}$ [A/m]
1	13,36	21,18	50,94	0,13	−0,04	0,01
2	2,95	6,83	30,65	0,02	−0,05	−0,03
3	1,45	3,71	18,95	0,01	−0,04	−0,04
4	0,93	2,37	12,17	0,01	−0,02	−0,04
5	0,67	1,67	8,40	0,01	−0,01	−0,07

Na Sl. 5 i 6 prikazana su poređenja vremenskih oblika simuliranih i izmerenih magnetskih polja za razmatrane amplitude magnetske indukcije sinusnog i trougaonog oblika, respektivno. Mogu se uočiti dobra slaganja simuliranih i izmerenih magnetskih polja za oba razmatrana slučaja. Blaga odstupanja se uočavaju u trenucima kada magnetsko polje menja znak.

Kako je za merenje i proračun magnetskog polja korišćeno ukupno 1000 podataka, a slaganje izmerenih i simuliranih signala je veoma dobro, radi bolje preglednosti rezultata je simulirano polje prikazano punom linijom, a izmereno polje je prikazano tačkama, uz redukovan broj tačaka (jer 1000 tačaka takođe nije pregledno). Smanjenje broja tačaka je izvršeno bez brisanja podataka pomoću ugrađene opcije Skip Points u programu OriginLab. Na ovaj način je postignut željeni vizuelni efekat, bez uticaja na tačnost rezultata. Broj tačaka je odabran u skladu sa amplitudom polja.

Na Sl. 7 i 8 prikazano je poređenje simuliranih i izmerenih histerezisnih petlji (zbog preglednosti rezultata, prikazan je manji broj tačaka za izmerene petlje). Uočava se dobro slaganje svih prikazanih petlji. Minimalna odstupanja simuliranih petlji mogu se pripisati kako odstupanjima kod magnetskih polja tako i odstupanjima izmerenih i simuliranih (idealnih) oblika magnetske indukcije.

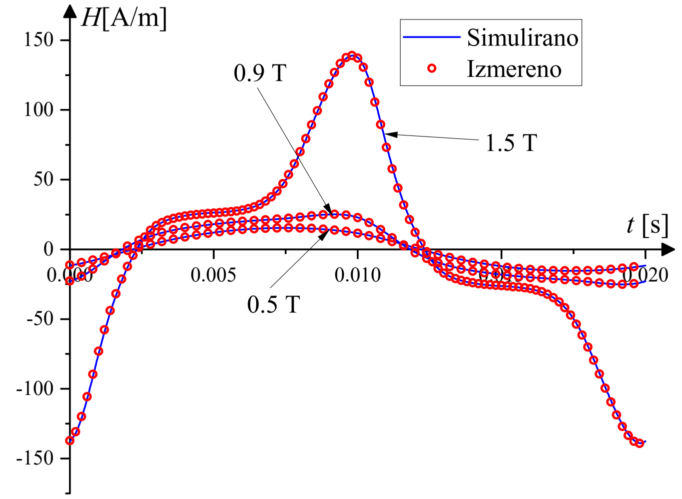

Sl. 5. Poređenje simuliranih i izmerenih trenutnih vrednosti magnetskog polja pri sinusnom obliku magnetske indukcije.

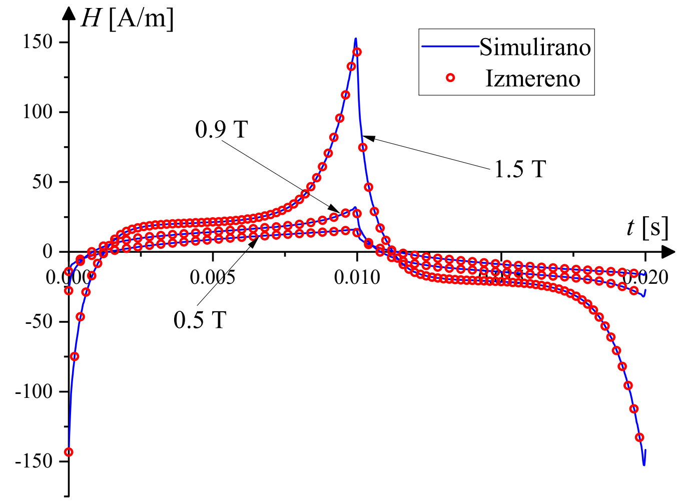

Sl. 6. Poređenje simuliranih i izmerenih trenutnih vrednosti magnetskog polja pri trougaonom obliku magnetske indukcije.

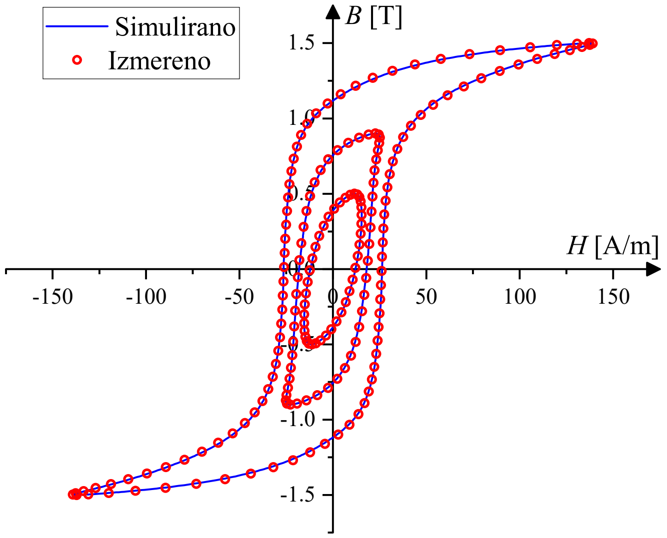

Sl. 7. Poređenje simuliranih i izmerenih histerezisnih petlji pri sinusnom obliku magnetske indukcije.

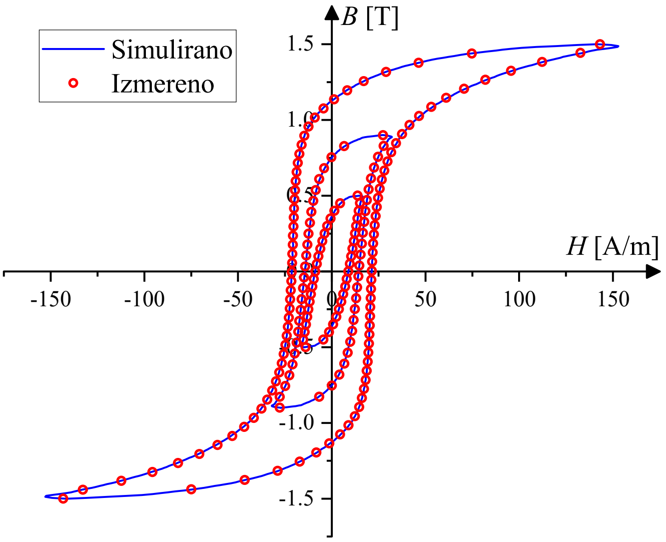

Sl. 8. Poređenje simuliranih i izmerenih histerezisnih petlji pri trougaonom obliku magnetske indukcije.

Dodatno, radi provere tačnosti kompletnog simulacionog postupka izvršeno je izračunavanje površina histerezisnih petlji i njihova analiza. U Tabeli IV je prikazano poređenje relativnih odstupanja površina histerezisnih petlji dobijenih simulacijom S_{sim} i merenjem S_{izm} za sinusni, δS_s, i trougaoni, δS_t, oblik indukcije, gde je $\delta S\,[\%]=100(S_{\mathrm{sim}}-S_{\mathrm{izm}})/S_{\mathrm{izm}}$.

TABELA IV

POREĐENJE RELATIVNIH ODSTUPANJA POVRŠINA HISTEREZISNIH PETLJI

$B_{\max}$ [T]	δS_s [%]	δS_t [%]
0,5	−0,24	0,06
0,9	−1,50	−0,71
1,5	−1,21	0,69

Relativna odstupanja površina petlji su mala – reda veličine procenta i za sinusni i za trougaoni oblik magnetske indukcije.

Može se zaključiti da je tačnost predloženog postupka simulacije histerezisnih petlji zadovoljavajuća u svim razmatranim aspektima, pa se može očekivati i zadovoljavajuća tačnost u primeni istog u složenijim proračunima sa magnetskim kolima. Primenom prikazane harmonijske analize i postupka simulacije pri različitim frekvencijama pobudnog polja može se dobiti kompletnija slika o karakteristikama magnetskog materijala ili jezgra. Dodatno, ovaj postupak omogućava rešavanje i analizu magnetskih problema u vremenskom domenu.

VI. ZAKLJUČAK

U ovom radu je prikazan postupak simulacije histerezisnih petlji za određene amplitude i oblike magnetske indukcije. Postupak se zasniva na interpolaciji amplituda i faza harmonika, a zatim i simulaciji magnetskog polja i magnetske indukcije od interesa.

U radu je ukratko opisana metoda merenja magnetskih karakteristika i predstavljene su izmerene histerezisne petlje za sinusni i trougaoni oblik magnetske indukcije sa amplitudama od 0,2 T do 1,6 T sa korakom od 0,2 T. Rezultati harmonijske analize odgovarajućih magnetskih polja su takođe prikazani i analizirani. Na osnovu tako dobijenih harmonika je izvršena simulacija novih magnetskih polja i histerezisnih petlji. Rezultati simulacije su analizirani kroz poređenje interpoliranih i izračunatih amplituda harmonika, trenutnih vrednosti magnetskog polja, oblika histerezisnih petlji i njihovih površina. Utvrđeno je vrlo dobro slaganje svih simuliranih i izmerenih rezultata.

Na osnovu prikazane analize rezultata je zaključeno da se opisani postupak može primeniti za kvalitetniju karakterizaciju feromagnetskih materijala i za rešavanje problema sa magnetskim kolima u vremenskom domenu.

DODATAK

Deo programskog koda za učitavanje merenih podataka, simulaciju magnetske indukcije, proračun harmonika magnetskog polja i njihovu interpolaciju je prikazan na Sl. 9. Prikazan je najvažniji deo koda u kojem se vidi način primene funkcija *Fourier* i *Interpolation*. Ostatak koda za proračun veličina od interesa i njihov numerički ili grafički prikaz je izostavljen jer prevazilazi obim rada, pri čemu su ti rezultati već prikazani u samom radu.

Unos podataka - Sinus

```
Podaci = Import["F:\\Desktop\\RADOVI\\RADOVI ETRAN 2021\\Divac\\50Hz-Sin-Loops.txt", "Table"];
PodaciProvere = Import["F:\\Desktop\\RADOVI\\RADOVI ETRAN 2021\\Divac\\50Hz-1_5T-Sin.txt", "Table"];

Bzeljeno = 1.5;
Nh = 5; (*Broj neparnih harmonika*)
```

Simulacija B

```
Bvr = Table[Bzeljeno * Sin[2 * 50 * Pi * t + 3 * Pi / 2], {t, 0, (0.02 - 0.02 / 1000), (0.02 / 1000)}];
```

Interpolacija - Pojedinacni Harmonici

```
PodaciPolja = Table[Podaci[[All, i]], {i, 2, Length[Podaci[[1, All]]], 2}];
PodaciIndukcije = Table[Podaci[[All, i]], {i, 3, Length[Podaci[[1, All]]], 2}];
PodaciPolja = Transpose[PodaciPolja];
PodaciIndukcije = Transpose[PodaciIndukcije];

AmplitudeHarmonika = Table[0, {i, Nh}, {j, Length[PodaciPolja[[1, All]]]}];
FazeHarmonika = Table[0, {i, Nh}, {j, Length[PodaciPolja[[1, All]]]}];

For[j = 1, j ≤ Length[PodaciPolja[[1, All]]], j++, HVr = Table[{Podaci[[i, 1]], PodaciPolja[[i, j]]}, {i, 1000}];
 ft = Fourier[HVr[[All, 2]], FourierParameters → {-1, -1}];
 pom1 = 2 * Abs[ft];
 pom2 = Arg[ft] * 180 / Pi;
 FazPolja = Table[pom2[[i]], {i, 2, Nh * 2, 2}];
 APolja = Table[pom1[[i]], {i, 2, Nh * 2, 2}];
 For[i = 1, i < Nh, i++, If[FazPolja[[i]] < 0, FazPolja[[i]] = FazPolja[[i]] + 360, FazPolja[[i]] = FazPolja[[i]]]];
 For[i = 1, i ≤ Nh, i++, AmplitudeHarmonika[[i, j]] = APolja[[i]];
  FazeHarmonika[[i, j]] = FazPolja[[i]]]]

AmplitudeHarmonika = Transpose[AmplitudeHarmonika]
FazeHarmonika = Transpose[FazeHarmonika]

Bmax = Table[Max[PodaciIndukcije[[All, i]]], {i, Length[PodaciIndukcije[[1, All]]]}];

Ampl = Table[0, {i, Nh}];
Faz = Table[0, {i, Nh}];

For[k = 1, k <= Nh, k++, PodaciInterpolacijeAmplituda = Table[{Bmax[[i]], AmplitudeHarmonika[[i, k]]}, {i, 1, Length[Bmax]}];
 PodaciInterpolacijeFaza = Table[{Bmax[[i]], FazeHarmonika[[i, k]]}, {i, 1, Length[Bmax]}];
 FunkcijaA = Interpolation[PodaciInterpolacijeAmplituda, InterpolationOrder → 6];
 FunkcijaF = Interpolation[PodaciInterpolacijeFaza, InterpolationOrder → 1];
 Ampl[[k]] = FunkcijaA[Bzeljeno];
 Faz[[k]] = FunkcijaF[Bzeljeno];]
(*-------------------------------------------------------*)
```

Sl. 9. Deo programskog koda za simulaciju magnetskog polja i indukcije.

ZAHVALNICA

Istraživanja prezentovana u ovom radu su delimično finansirana sredstvima Ministarstva prosvete, nauke i tehnološkog razvoja RS, Ugovor br. 451-03-9/2021-14/200132, čiji je realizator Fakultet tehničkih nauka u Čačku - Univerziteta u Kragujevcu.

LITERATURA

[1] C. Grech, M. Buzio, M. Pentella, M. Sammut, “Dynamic Ferromagnetic Hysteresis Modelling Using a Preisach-Recurrent Neural Network Model”, *Materials.*, vol. *13*, no. *11*, Spec. issue: *Model. and Char. of Magn. Mat.*, June 2020.

[2] S. E. Zirka, Y. I. Moroz, R. G. Harrison, K. Chwastek, “On physical aspects of the Jiles-Atherton hysteresis models”, *J. of Appl. Phys.*, vol. *112*, no. *8*, Aug. 2012.

[3] Y. Li, R. Chen, Z. Cheng, C. Zhang, L. Liu, “Dynamic Hysteresis Lops Modeling of Electrical Steel with Harmonic Components”, *IEEE Trans. on Ind. Appl.*, vol. *56*, no. *5*, pp. 4804-4811, Sept.-Oct. 2020.

[4] A. Milovanović, B. Koprivica, “Mathematical Model of Major Hysteresis Loop and Transient Magnetizations”, *Electromagnetics*, vol. *35*, no. *3*, pp. 155-166, Match 2015.

[5] Y. Hane, K. Nakamura, “Dynamic Hysteresis Modeling for Magnetic Circuit Analysis by Incorporating Play Model and Cauer’s Equivalent Circuit Theory”, *IEEE Trans. on Magn.*, vol. *56*, no. *8*, Aug. 2020.

[6] Q. Antonio, R. Fulginei, H. P. Rimal, A. M. Ghanim, “On the Use of Feedforward Neural Networks to Simulate Magnetic Hysteresis in Electrical Steelsy”, *20th Mediterranean Electrotechnical Conference (MELECON)*, Palermo, Italy, 16th-18th June 2020.

[7] S. Q. Antonio, F. R. Fulginei, K. Nakamura, A. Laudani, A. Faba, E. Cardelli, “An Effective Neural Network Approach to Reproduce Magnetic Hysteresis in Electrical Steel under Arbitrary Excitation Waveforms”, *J. of Magn. and Magn. Mat.*,vol. *528*, June 2021.

[8] G. Bramerdorfer, D. Andessner, “Accurate and Easy to Obtain Iron Loss Model for Electric Machine Designs”, *IEEE Trans. on Indu. Electr.*, vol. *64*, no. *3*, pp. 2530-2537, March 2017.

[9] B. Koprivica, I. Dumitru, A. Milovanović and O. Caltun, “Harmonic Analysis and Modelling of Magnetisation Process in Soft Ferromagnetic Material”, *FACTA Universitatis, Electronics and Energetics*, vol. *30*, no. *1*, pp. 121 – 136, March 2017.

[10] B. Koprivica, A. Milovanović and M. Đekić, “Effects of Wound Toroidal Core Dimensional and Geometrical Parameters on Measured Magnetic Properties of Electrical Steel”, *Serb. J. of Electr. Eng.*, vol. *10*, no. *3*, pp. 459-471, Oct. 2013.

[11] W. Cheng and Y. Saito, “Modeling and Analysis pf Hysteresis by Harmonic Balance Method“, *J. of Appl. Phys.*, vol. *117*, no. *17*, May 2015.

[12] S. Zurek, P. Marketos, T. Meydan, and A.J. Moses, “Use of Novel Adaptive Digital Feedback for Magnetic Measurements Under Controlled Magnetizing Conditions”, *IEEE Trans. on Magn.*, vol. *41*, no. *11*, pp. 4242-4249, Nov. 2005.

[13] J. V. Surutka, “*Elektromagnetika*”*, osmo izdanje*, Akademska misao, Beograd, 2006.

ABSTRACT

The aim of this paper is to present a procedure for simulation of hysteresis loops of a ferromagnetic sample which is performed by simulation of waveforms of the magnetic field strength (further magnetic field) and flux density. The data for magnetic field and flux density are obtained by measurement, under controlled shape of magnetic flux density, for two considered shapes - sinusoidal and triangular. The harmonics of the magnetic field for the known amplitudes of the magnetic flux density were determined according to these data. New values of these harmonics are calculated by interpolating ones previously calculated, for the amplitude of magnetic flux density of interest. Simulation of the new magnetic field waveform is performed using these harmonics. The new hysteresis loop is simulated using this magnetic field and new simulated magnetic flux density. Description of this simulation procedure, comparison of calculated and measured amplitudes of harmonics and magnetic field waveforms, as well as hysteresis loops, is given in this paper. Appropriate analysis and discussion of the results is also given.

Simulation of hysteresis loops by interpolation of harmonic components of magnetic field

Srđan Divac, Branko Koprivica

Analiza uticaja magnetske interakcije faza na karakteristike 8/6 SRM-a

Dragan S. Mihić, *Member, IEEE*, Mladen V. Terzić, *Member, IEEE,* Žarko V. Koprivica, *Student, IEEE,* Bogdan M. Brković, *Member, IEEE*

Apstrakt— **U cilju unapređenja performansi, rad prekidačkog reluktantnog motora (Switched Reluctance Motor-SRM) zahteva jednovremeno pobuđivanje više faza motora. Budući da magnetski polaritet pobuđenih faza motora može biti isti ili različit, u ovom radu je izvršena detaljna analiza uticaja magnetskog polariteta na fluksne obuhvate faza 8/6 SRM-a. Ova analiza je izvršena na osnovu statičkih karakteristika koje su dobijene korišćenjem modela baziranog na metodi konačnih elemenata (Finite Element Method-FEM) u softverskom paketu Ansys Electronics. Pored toga, imajući u vidu da kod 8/6 SRM-a korišćenjem standardnog asimetričnog polumostnog invertora (API) nije moguće ostvariti magnetsku simetriju faza, rezultujući efekti veoma izražene interakcije faza su analizirani na primeru odgovarajućih tranzijentnih talasnih oblika faznih struja i momenta.**

***Ključne reči*—Prekidački reluktantni motor, interakcija faza, metoda konačnih elemenata.**

I. UVOD

Prekidački reluktantni motori zbog svojih istaknutih osobina kao što su jednostavna i jeftina proizvodnja, mehanička i termička robusnost, velika gustina snage, širok opseg brzina i pouzdanost, privlače značajnu pažnju i postaju značajni konkurenti mašinama naizmenične struje pre svega u električnim automobilima, vetrogeneratorima, avio industriji [1-4].

U cilju unapređenja efikasnosti, rad SRM-a zahteva jednovremeno pobuđivanje više faza motora [5]. Na taj način se doprinosi uvećanju momenta i smanjenu njegove valovitosti. To je naročito izraženo za konfiguracije SRM-a sa brojem faza koji je veći od tri. Broj istovremeno pobuđenih faza zavisi od radnog režima i u opštem slučaju taj broj može biti veći od dva. Interakcija faza može biti rezultat istovremene magnetizacije faze i demagnetizacije njoj susedne faze ili istovremene magnetizacije susednih faza motora kada zbog velike širine ugla vođenja dolazi i do značajnije interakcije ortogonalnih faza SRM-a. Kao posledica istovremenog pobuđivanja faza mogu se javiti različite putanje magnetskog fluksa u mašini. Karakter i specifičnosti tih putanja su vezane za magnetski polaritet pobuđenih faza koji zavisi od smera struje u njima. Budući da magnetski polaritet pobuđenih faza može biti isti ili različit, tokom rada motora, raspodela magnetskog fluksa u mašini je direktno određena njihovim trenutnim stanjem. Dakle, međusobni fluks kao i rezultujuće magnetsko zasićenje koje se javlja usled interakcije faza je direktno vezano za magnetski polaritet pobuđenih faza motora čime se direktno utiče na performanse SRM-a.

Da bi se utvrdili efekti interakcije faza na fluksne obuhvate a samim tim i na performanse mašine neophodno je korišćenje tačnog modela koji uzima u obzir efekte međusobne sprege i zasićenja tokom istovremenog vođenja faza. Generalno, poteškoće koje se javljaju tokom modelovanja i analize SRM-a su posledica izrazito nelinearne veze fluksa, struje i položaja rotora budući da je normalan rad SRM-a praćen dubokim zasićenjem. Zbog toga, zahtev za modelovanjem efekata međusobne interakcije faza predstavlja dodatnu poteškoću.

U [6] je analiziran uticaj polariteta sukcesivnih faza motora sa konstantnim strujama na raspodelu fluksa u različitim delovima mašine i generisanje elektromagnetskog momenta. Navedene su neke kvalitativne osobine dugih i kratkih putanja fluksa koje mogu biti osnova za unapređenje tehnika koje se bave smanjenjem valovitosti momenta i gubitaka u gvožđu. Međutim, nisu prikazani rezultati tranzijentnih simulacija koji prikazuje uticaj efekata interakcija faza na fluksne obuhvate, fazne struje i momenat.

Mnogi radovi [7-12] naglašavaju važnost modelovanja međusobne sprege faza i njenog uticaja na tranzijentne karakteristike SRM-a. Međutim, u odgovarajućim razvijenim matematičkim modelima uticaj struje koja postoji u faznom namotaju na odgovarajući fluksni obuhvat tokom interakcije sa drugim pobuđenim fazama se zanemaruje pa zbog toga ovi efekti i nisu analizirani.

Dinamički modeli [13-15] uzimaju u obzir međusobnu spregu faza bazirajući se na karakteristikama magnetostatičkog FEM-a ili eksperimenta. Pri tome, ulazne statičke karakteristike razmatraju uticaj samo dve pobuđene faze što je ograničavajuće u analizi i modelovanju dinamičkih radnih režima kada su istovremeno pobuđene tri ili četiri faze motora, što se uobičajeno ima u slučaju četvorofaznih SRM-a. Nelinearni analitički model [16] uzima u obzir efekte interakcije faza, ali njegove tranzijentne simulacije u opštem slučaju ne pružaju mogućnost da se u potpunosti, na eksplicitan način, analizira uticaj rezultujućeg magnetskog zasićenja na karakteristike motora tokom istovremenog

Dragan S. Mihić – Elektrotehnički fakultet, Univerzitet u Beogradu, Bulevar kralja Aleksandra 73, 11020 Beograd, Srbija (e-mail: dragan84m@etf.bg.ac.rs).

Mladen V. Terzić – Elektrotehnički fakultet, Univerzitet u Beogradu, Bulevar kralja Aleksandra 73, 11020 Beograd, Srbija (e-mail: terzic@etf.bg.ac.rs).

Žarko V. Koprivica – Elektrotehnički fakultet, Univerzitet u Beogradu, Bulevar kralja Aleksandra 73, 11020 Beograd, Srbija (e-mail: kopri@etf.bg.ac.rs).

Bogdan M. Brković – Elektrotehnički fakultet, Univerzitet u Beogradu, Bulevar kralja Aleksandra 73, 11020 Beograd, Srbija (e-mail: brkovic@etf.bg.ac.rs).

vođenja više faza motora.

U ovom radu je izvršena detaljna analiza uticaja magnetskog polariteta na fluksne obuhvate faza 8/6 SRM-a. Ova analiza je izvršena na osnovu statičkih karakteristika koje su dobijene korišćenjem modela baziranog na FEM-u u softverskom paketu Ansys Electronics. Pored toga, imajući u vidu da kod 8/6 SRM-a korišćenjem standardnog asimetričnog polumostnog invertora nije moguće ostvariti magnetsku simetriju faza, rezultujući efekti veoma izražene interakcije faza su prikazani i analizirani na primeru odgovarajućih tranzijentnih talasnih oblika faznih struja i momenta.

U II poglavlju su navedeni glavni koraci u modelovanju 8/6 SRM-a metodom konačnih elemenata u programu Ansys Electronics u cilju dobijanja statičkih i dinamičkih karakteristika. Analiza uticaja magnetskog polariteta na statičke karakteristike fluksnih obuhvata 8/6 SRM-a je data u poglavlju III. Izraženi rezultujući efekti interakcije faza na dinamičke talasne oblike faznih struja i elektromagnetskog momenta su prikazni i analizirani u poglavlju IV. Zaključak je dat u V poglavlju.

II. MODELOVANJE 8/6 SRM-A METODOM KONAČNIH ELEMENATA U PROGRAMSKOM PAKETU ANSYS ELECTRONICS

Na Sl. 1 je prikazan poprečni presek 8/6 SRM-a za koji se određuju statičke i dinamičke karakteristike u cilju utvrđivanja uticaja magnetskog polariteta faza na njegove karakteristike. Glavni parametri i dimenzije 8/6 SRM-a su dati u Tabelama 1 i 2, respektivno. Magnetostatički i tranzijentni FEM model, uključujući 8/6 SRM geometriju, materijale, električno i magnetsko kolo, granične uslove, mrežu konačnih elemenata u programskom paketu Ansys Electronics su definisani saglasno [16]. Pored toga, da bi se dobile statičke karakteristike fluksnih obuhvata, definisan je odgovarajući opseg konstantnih struja posmatranih faza motora na ugaonom intervalu od neusaglašenog do usaglašenog položaja rotora. Sa druge strane, za dobijanje rezultata tranzijentne simulacije definisano je eksterno kolo koje predstavlja API-a. Gore navedeni model je napravljen uzimajući u obzir da znak “×” predstavlja provodnike u kojima postoji struja u smeru od posmatrača, dok oznaka “● ”predstavlja provodnike u kojima struja postoji u smeru ka posmatraču.

U skladu sa ovim, primenom unipolarnog napajanja rezultujuća magnetska sekvenca u pobuđivanju faza A-B-C-D-A-B-C-D je S-S-S-S-N-N-N-N. Kod ove magnetske sekvence tri od četiri kombinacije susednih faza motora su istog, a jedna različitog magnetskog polariteta.

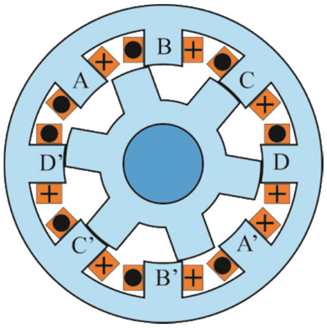

Sl.1. Poprečni presek 8/6 SRM-a

TABELA 1
GLAVNI PARAMETRI 8/6 SRM-A

Parametri	Vrednost
Broj faza	4
Broj statorskih/rotorskih polova	8/6
Nominalni fazni napon [V]	220
Nominalna fazna struja [A]	3.2
Fazna otpornost [Ω]	2.1
Induktivnost u neusaglašenom položaju [mH]	14
Broj navojaka po fazi	284

TABELA 2
GLAVNE DIMENZIJE 8/6 SRM-A

Dimenzije	Vrednost
Spoljašnji poluprečnik statora [mm]	60
Unutrašnji poluprečnik statora [mm]	37.5
Debljina jarma statora [mm]	9
Spoljašnji poluprečnik rotora [mm]	37
Unutrašnji poluprečnik rotora [mm]	24
Debljina jarma rotora [mm]	9
Širina vazdušnog zazora [mm]	0.5
Poluprečnik vratila [mm]	15
Dužina magnetskog kola [mm]	65
Širina statorskog pola [°]	22
Širina rotorskog pola [°]	23

III. ANALIZA UTICAJA INTERAKCIJE FAZA NA STATIČKE Ψ-I KARAKTERISTIKE

Da bi se utvrdio uticaj magnetskog polariteta faza na fluksni obuhvat kada je jaram statora i rotora, usled rezultujućih efekata interakcije faza u dubokom zasićenju, od interesa je analizirati odgovarajuće statičke Ψ-i karakteristike posmatrane faze tokom njene interakcije sa fazom koja joj prethodi, ali i fazom koja je sledi za različite ugaone položaje rotora. U suštini, potpuno je svejedno za koju fazu se analiziraju navedene karakteristike, pa će se u nastavku posmatrati Ψ-i karakteristike faze A kao i rezultujući efekti međusobne interakcije sa fazama D i B za različite ugaone položaje rotora. Od interesa je posmatrati takve ugaone položaje rotora koji će omogućiti da se utvrdi priroda uticaja

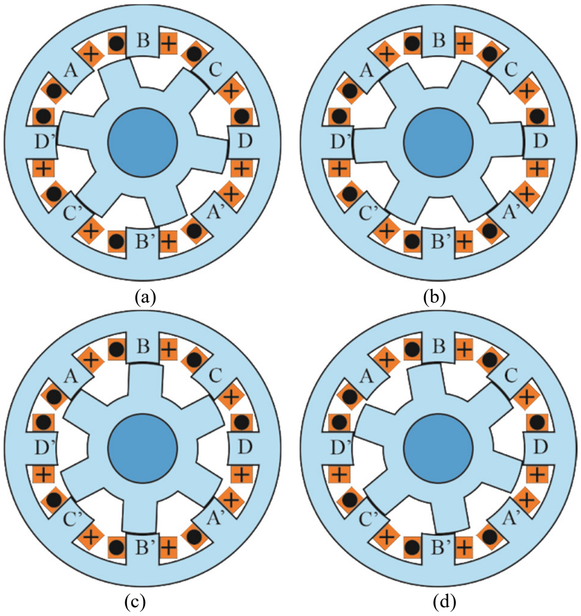

(a) (b)

(c) (d)

Sl. 2. Ugaoni položaji rotora (a) θ_m=5°, (b) θ_m=17.5°, (c) θ_m=42.5° i (d) θ_m=55° u odnosu na neusaglašeni položaj faze A.

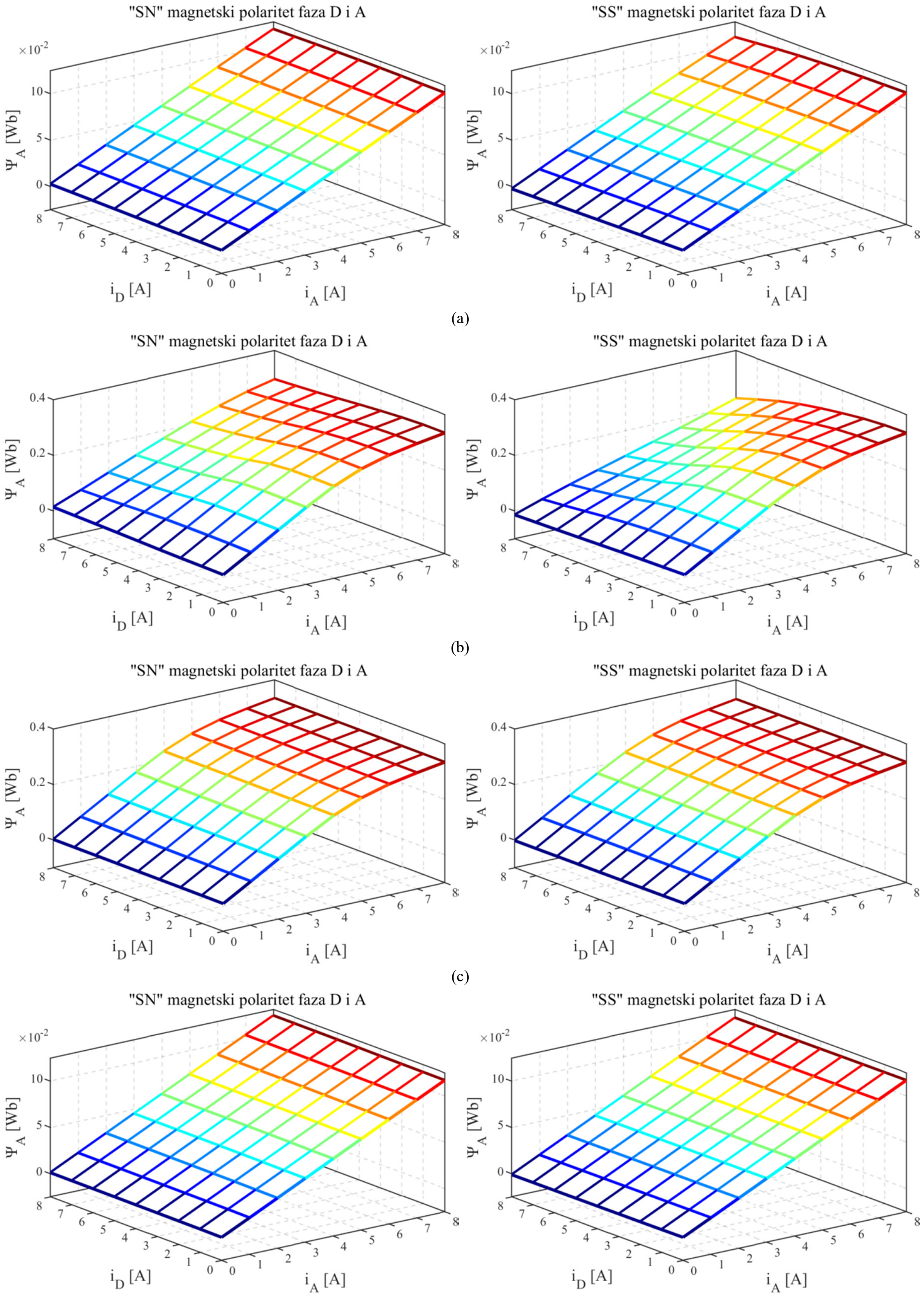

(a)

(b)

(c)

(d)

Sl. 3. *Ψ-i* karakteristike faze A za ugaoni položaj rotora (a) θ_m=5°, (b) θ_m=17.5°, (c) θ_m=42.5° и (d) θ_m=55° kada je magnetski polaritet susednih faza D i A različit (SN) i isti (SS).

međusobne interakcije na *Ψ-i* karakteristiku faze na celom opsegu polnog koraka rotora faze A. Zbog toga, u odnosu na referentni ugaoni položaj rotora koji odgovara neusaglašenom položaju faze A, izabrana su četiri ugaona položaja rotora θ_m

saglasno Sl. 2.

Statičke Ψ-i karakteristike faze A na Sl. 3, koje odgovaraju ugaonim položajima rotora $\theta_m=5^\circ$; $\theta_m=17.5^\circ$; $\theta_m=42.5^\circ$ i $\theta_m=55^\circ$, respektivno, i opsegu struja i_A, $i_D=(0,1,2,\ldots,8)$ A, ukazuju na uticaj struje faze D na fluksni obuhvat faze A kada je njihov magnetski polaritet različit odnosno isti. Pri tome, od interesa je naglasiti da se promena magnetskog polariteta faze D u FEM modelu vrši promenom smera odgovarajuće struje.

Sa povećanjem struje i_D pri konstantnoj vrednosti struje i_A, u slučaju različitog magnetskog polariteta faza A i D, fluksni obuhvat Ψ_A monotono raste do određene vrednosti usled pozitivnog međusobnog fluksa koji postoji između njih. Međutim, nakon određene vrednosti struje i_D on se smanjuje usled dubokog magnetskog zasićenja delova jarma statora i rotora gde postoji preklapanje flukseva ovih faza. Pri istim uslovima, u slučaju istog magnetskog polariteta, usled negativnog međusobnog fluksa, ima se monotono opadanje fluksnog obuhvata Ψ_A sa većom strminom opadanja kada jaram statora i rotora uđe u zasićenje. Dakle, statičke Ψ-i karakteristike jasno ukazuju na uticaj polariteta međusobnog fluksa na ukupni fluksni obuhvat faze.

Efekat opadanja fluksnog obuhvata kada nastupi duboko zasićenje je izraženiji u slučaju istog magnetskog polariteta budući da su tada putanje magnetskog fluksa u opštem slučaju duže. To se može jasno uočiti posmatrajući raspodelu magnetskog polja na Sl. 4 i 5. Na Sl. 4 su date raspodele magnetskog polja u trenucima kada su fluksni obuhvat faze A i D isti i različiti po amplitudi pri istom magnetskom polaritetu. Sa druge strane, Sl. 5 odgovara raspodeli magnetskog polja u istim trenucima, ali u slučaju različitog magnetskog polariteta. Kao posledica gore navedenog, veći pad magnetskog napona, odnosno manji fluksni obuhvat se ima u slučaju istog magnetskog polariteta nego u slučaju kada je on različit.

Dakle, uticaj faze koja prethodi posmatranoj se manifestuje na takav način da se ima veći fluksni obuhvat posmatrane faze kada je njihov magnetski polaritet različit. Pri tome, treba naglasiti da se benefit različitog magnetskog polariteta u odnosu na isti osetnije javlja prilikom veće preklopljenosti statorskih i rotorskih polova posmatrane faze A. Sa druge strane, kada ne postoji njihovo preklapanje ili se ono smanjuje, tada su efekti međusobne interakcije faza manje izraženi. Odnos fluksnih obuhvata, čak i pri dubokom zasićenju, je približno isti u oba slučaja. Međutim, uvek je veći u slučaju različitog magnetskog polariteta. Ove pojave se mogu jasno uočiti na Sl. 6, gde su za posmatrane ugaone položaje rotora izdvojene Ψ-i karakteristike faze A pri vrednosti struje faze D od 2 A i 8 A.

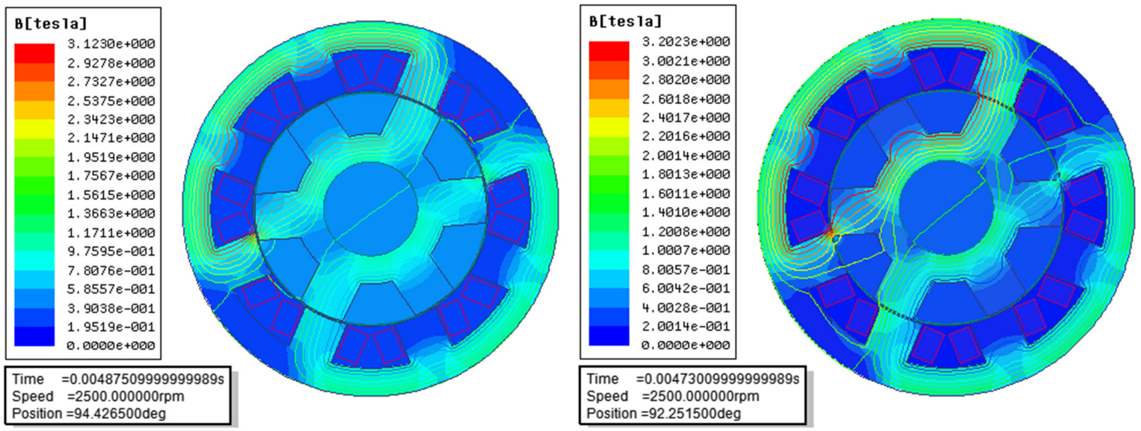

(a) (b)

Sl. 4. Raspodela magnetskog polja u trenutku kada je (a) $\Psi_D=\Psi_A$ i (b) $\Psi_D>\Psi_A$ pri čemu su istovremeno pobuđene faze D i A istog magnetskog polariteta.

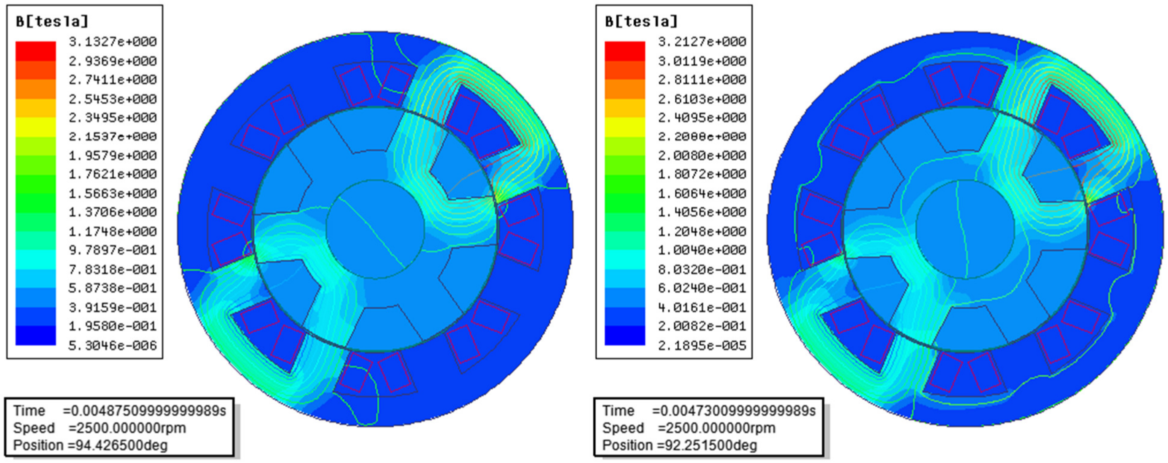

(a) (b)

Sl. 5. Raspodela magnetskog polja u trenutku kada je (a) $\Psi_D=\Psi_A$ i (b) $\Psi_D>\Psi_A$ pri čemu su istovremeno pobuđene faze D i A različitog magnetskog polariteta.

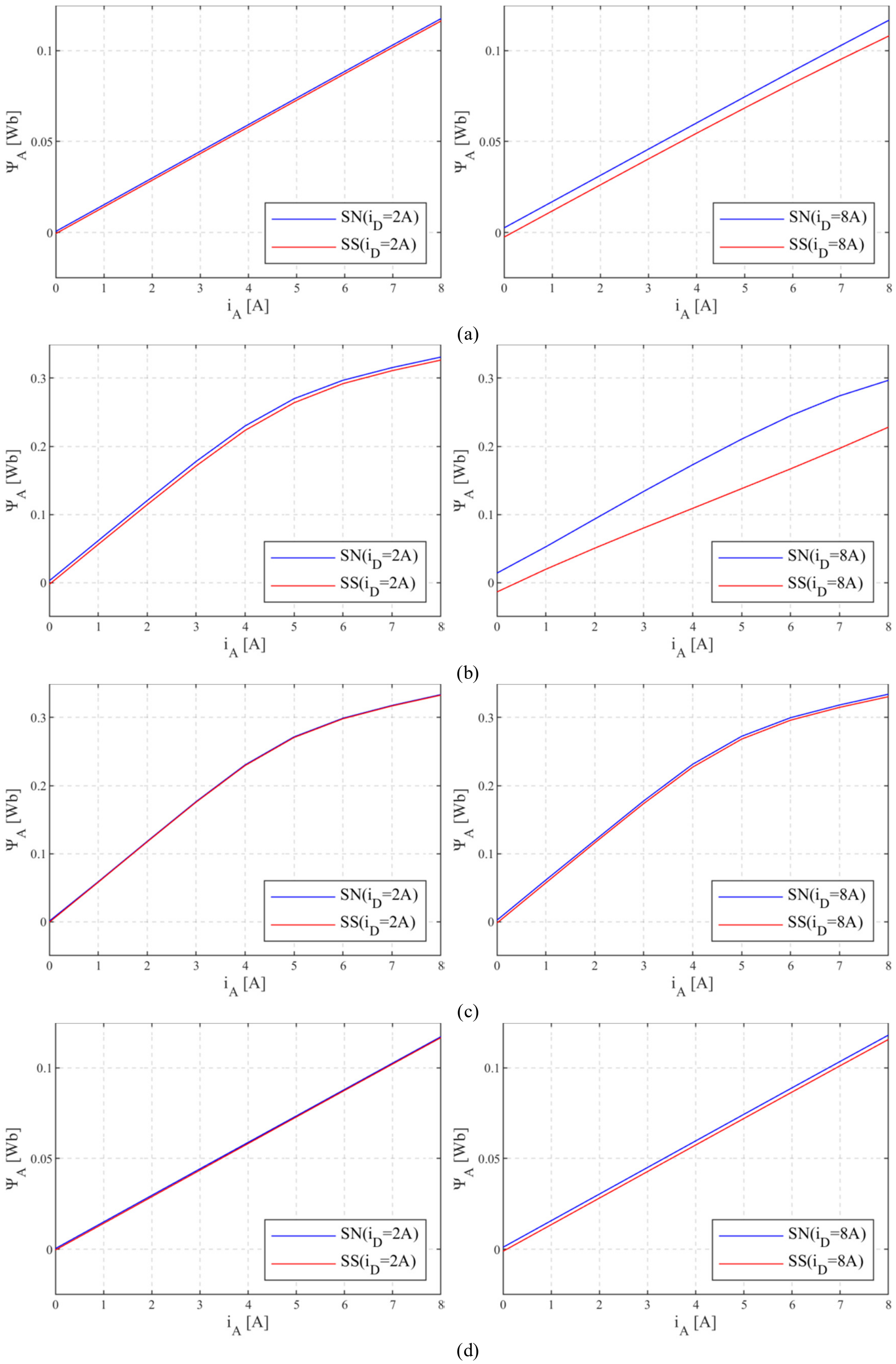

(a)

(b)

(c)

(d)

Sl. 6. Uticaj struje faze D na fluksni obuhvat faze A za ugaoni položaj rotora (a) θ_m=5°, (b) θ_m=17.5°, (c) θ_m=42.5° i (d) θ_m=55° kada je magnetski polaritet susednih faza D i A različit (SN) i isti (SS).

Slično gore sprovedenoj analizi, potrebno je utvrditi i efekte interakcije koji se javljaju kao posledica istovremenog vođenja faza A i B. Do ovih zaključaka se može doći na osnovu rezultata koji prikazuju uticaj struje faze D na fluksni obuhvat faze A. Naime, pažljivom analizom se može zaključiti da raspodeli magnetskog fluksa u mašini, kada su istovremeno pobuđenje faze D i A, za neki ugaoni položaj rotora θ_m, odgovara ista raspodela magnetskog fluksa za ugaoni položaj rotora θ_m'=60-θ_m kada su istovremeno pobuđene faze A i B. Pri tome je od interesa naglasiti da se za definisane kombinacije susednih faza motora posmatra odgovarajući magnetski polaritet. Zbog toga se u položaju rotora θ_m=5° i θ_m'=55° respektivno ima ista Ψ-i karakteristika faze A kada su istovremeno pobuđene faze D i A odnosno A i B, respektivno. Slično važi i za druga dva razmatrana položaja rotora.

IV. ANALIZA UTICAJA INTERKCIJE FAZA NA TRANZIJENTNE KARAKTERISTIKE

Prethodno sprovedena analiza koja se odnosila na statičke Ψ-i karakteristike pruža mogućnost da se analizira i uticaj magnetskog polariteta faza na tranzijentne karakteristike. To će se pokazati na primeru radne tačke koju karakteriše veoma izražena interakcija faza. Ova radna tačka je definisana kontrolnim parametrima: naponom napajanja (V_{DC}), uglom uključenja (θ_{ON}), uglom isključenja (θ_{OFF}) i brzinom obrtanja (n) koji su dati u Tabeli 3. Odgovarajući talasni oblici faznih struja i elektromagnetskog momenta su prikazani na Sl. 7 i 8, respektivno.

Saglasno Sl. 7, posmatranu radnu tačku karakteriše veliko preklapanje u vođenju faza budući da su tokom električnog ciklusa pobuđene tri ili sve četiri faze motora. Kao posledica izraženih efekata interakcije faza dolazi do nesimetrije faznih struja jer sekvencu pobuđivanja faza A-B-C-D-A-B-C-D karakteriše magnetska nesimetrija S-S-S-S-N-N-N-N. Posmatrajući magnetsku sekvencu, može se uočiti da je tokom magnetizacije kod sve tri faze koje prethode fazi D magnetski polaritet isti kao za fazu D. Zbog toga je i vršna vrednost struje i_D najveća. Budući da pobuđivanju faze A prethodi pobuđivanje faze D, saglasno tome i magnetskom polaritetu preostalih faza koje joj prethode, nakon faze D efekti interakcije faza su najizraženiji u fazi A. Sa druge strane, za faze B i C taj efekat je približno isti, ali je u izvesnoj meri izraženiji u fazi C jer se u dve od tri faze koje prethode fazi C ima isti magnetski polaritet kao kod faze C, dok se slučaju faze B to ima u jednoj od tri faze.

U trenutku početka demagetizacije faznog namotaja, efekti interakcije faza su najizraženiji u struji i_A jer je tada magnetski polaritet kod faze A isti kao kod preostalih faza koje je slede. Analogno, za razliku od magnetizacije, sada su ovi efekti izraženiji kod struje i_B u odnosu na struju i_C dok je najmanji uticaj na struju i_D. Pored razmatranih delova talasnih oblika faznih struja, od interesa je uočiti i pojavu koju karakteriše porast struje tokom demagnetizacije. Ova pojava je najviše izražena kod struje i_A a zatim kod i_B, i_D i i_C.

Izražena nesimetrija u talasnim oblicima faznih struja je u direktnoj vezi sa magnetskim polaritetom faza koje se isključuju ili uključuju i njihovim uticajem na preostale aktivne faze jer u trenutku komutacije faza dolazi do nagle promene rezultujućeg magnetskog zasićenja mašine. Pri tome, pojave usled efekata rezultujućeg magnetskog zasićenja su izraženije kada je veći broj pobuđenih faza istog magnetskog polariteta. Pored toga, od interesa je istaći da na talasni oblik struje posmatrane faze, pored dominantnog uticaja susednih faza utiče i njena interakcija sa odgovarajućom ortogonalnom fazom. Taj efekat se manifestuje tokom značajnijeg istovremenog vođenja faza što se ima u ovom primeru, ali i tokom komutacije faza. Nesimetrija koja postoji između talasnih oblika faznih struja se preslikava i na odgovarajuće efektivne vrednosti koje su date u Tabeli 4.

TABELA 3
RADNI REŽIM SA IZRAŽENOM INTERAKCIJOM FAZA

V_{DC} [V]	θ_{ON} [°]	θ_{OFF} [°]	n [ob/min]
220	23	53	3500

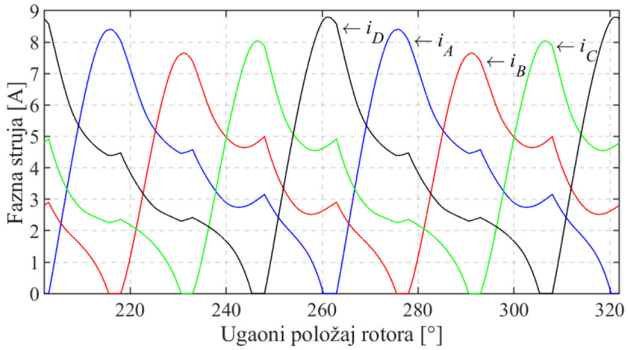

Sl. 7. Fazne struje 8/6 SRM-a za radni režim definisan u Tabeli 3.

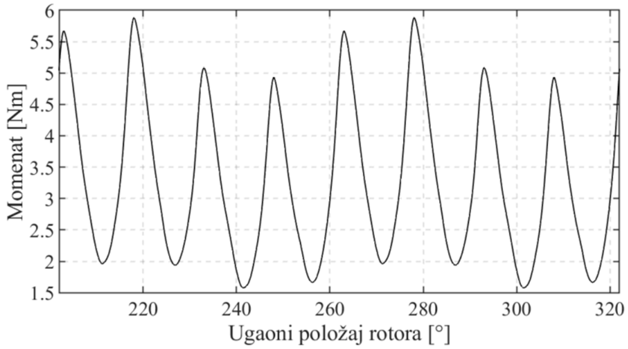

Sl. 8. Elektromagnetski momenat 8/6 SRM-a za radni režim definisan u Tabeli 3.

Kao posledica rezultujućih efekata interakcije faza talasni oblik momenta je takav da su sva četiri impulsa momenta tokom električnog ciklusa različita saglasno Sl. 5. Imajući u vidu analizu uticaja magnetskog polariteta faza na fluksne obuhvate, kao i odgovarajuće talasne oblike faznih struja, u delu električnog ciklusa tokom kojeg se magnetiše faza A impuls momenta ima najveću trenutnu vrednost i to u trenutku demagntizacije faze D koja prethodi fazi A u sekvenci pobuđivanja. Nakon toga, slede vršne vrednosti impulsa momenta tokom magnetizacije faza D, B i C u trenucima demagnetizacije faza koje im prethode u sekvenci pobuđivanja a to su C, A i B respektivno.

Imajući u vidu rezultate sprovedene analize, uobičajena je praksa da se pobuđivanje 8/6 SRM-a vrši magnetskom sekvencom (S-N-S-N-N-S-N-S) kod koje su tri od četiri

TABELA 4
EFEKTIVNE VREDNOSTI FAZNIH STRUJA ZA RADNU TAČKU DEFINISANU U TABELI 3

I_A[A]	I_B[A]	I_C[A]	I_D[A]
4.5711	4.2149	4.2251	4.5572

kombinacije susednih faza motora različite, a jedna ista. Korišćenje ove sekvence pobuđivanja omogućava postizanje boljih performansi pogona sa 8/6 SRM-om u odnosu na analiziranu magnetsku sekvencu. Pri tome, u cilju postizanja najvećeg odnosa srednje vrednosti momenta i efektivne vrednosti struje ili ripla momenta, od suštinske je važnosti optimizacija kontrolnih parametara.

V. ZAKLJUČAK

U ovom radu je izvršena analiza uticaja magnetskog polariteta faza na statičke i tranzijentne karakteristike 8/6 SRM-a koristeći model koji se bazira na metodi konačnih elemenata u programskom paketu Ansys Electronics. Rezultati statičkih karakteristika pokazuju da je fluksni obuhvat posmatrane faze veći ako je ona u interakciji sa fazom različitog magnetskog polariteta u odnosu na nju. Pri tome, benefit od različitog magnetskog polariteta u odnosu na isti se osetnije javlja prilikom veće preklopljenosti statorskih i rotorskih polova. Sa druge strane, kada ne postoji njihovo preklapanje ili se ono smanjuje, tada su efekti međusobne interakcije faza manje izraženi. Odnos fluksnih obuhvata, čak i pri dubokom zasićenju, je približno isti u oba slučaja. Međutim, uvek je veći u slučaju različitog magnetskog polariteta. Pored toga, kada postoji veoma izraženo zasićenje jarma mašine, tada je usled magnetske nesimetrije faza veoma izražena nesimetrija faznih struja kao i impulsa u talasnom obliku momenta. Imajući u vidu gore navedeno, u cilju postizanja boljih performansi 8/6 SRM-a, faze motora se pobuđuju na način da su odgovarajući magnetski polariteti sukcesivnih faza motora dominantno različiti.

LITERATURA

[1] Z. Yang, F. Shang, I. P. Brown, and M. Krishnamurthy, “Comparative study of interior permanent magnet, induction, and switched reluctance motor drives for EV and HEV applications,” *IEEE Trans. Transp. Electrific.*, vol. 1, no. 3, pp. 245-254, Oct. 2015.

[2] R. Cardenas *et al.*, “Control of switched reluctance generator for variable-speed wind energy applications,” *IEEE Trans. Energy Convers.*, 2005, vol. 20, no. 4, pp. 781-791, Dec. 2005.

[3] A. Chiba *et al.*, ‘Development of a rare-earth-free SR motor with high torque density for hybrid vehicles,’ *IEEE Trans. Energy Convers.*, vol. 30, no. 1, pp. 175–182, March 2015.

[4] V. Valdivia *et al.*, “Behavioral modeling of a switched reluctance generator for aircraft power systems,” *IEEE Trans. Ind. Electron.*, vol. 61, no. 6, pp. 2690-2699, June 2014.

[5] A. K. Jain and N. Mohan, “Dynamic modeling, experimental characterization, and verification for SRM operation with simultaneous two-phase excitation,” *IEEE Trans. Ind. Electron.*, vol. 53, no. 4, pp. 1238–1249, Jun. 2006.

[6] P. Pillay, Y. Liu, W. Cai, and T. Sebastian, “Multiphase operation of switched reluctance motor drives,” in *Proc. 32nd IAS Annu. Meeting*, vol. 1, 1997, pp. 310–317.

[7] Qu, B.; Song, J.; Liang, T.; Zhang, H., "Mutual coupling and its effect on torque waveform of even number phase switched reluctance motor," Electrical Machines and Systems, International Conference on, pp.3405-3410, Oct. 2008.

[8] J. C. Moreira and T. A. Lipo, “Simulation of a four phase switched reluctance motor including the effects of mutual coupling,” *Elect. Mach. Power Syst.*, vol. 16, pp. 281–289, 1989.

[9] R. M. Davis and I. H. Al-Bahadly, “Experimental evaluation of mutual inductance in a switched reluctance motor,” in *4th IEEE Int. Conf. Power Electronics and Variable Speed Drives*, London, U.K., 1991, pp. 243–248.

[10] D. Panda, V. Ramanarayanan, “Mutual coupling and its effect on steady-state performance and position estimation of even and odd number phase switched reluctance motor drive,” *IEEE Transactions on Magnetics*, vol. 43, pp. 3445-3456, August 2007.

[11] Essah, D. N.; Sudhoff, S.D., "An improved analytical model for the switched reluctance motor," Energy Conversion, IEEE Transactions on , vol.18, no.3, pp.349,356, Sept. 2003.

[12] M. A. Preston and J. P. Lyons, “A switched reluctance motor model with mutual coupling and multi-phase excitation,” *IEEE Trans. Magn.*, vol. 27, no. 6, pp. 5243–5245, Nov. 1991.

[13] S. Cao and K. J. Tseng, “Evaluation of neighboring phase coupling effects of switched reluctance motor with dynamic modeling approach,” in *Proc. PIEMC 2000*, vol. 2, 2000, pp. 881–886.

[14] A. K. Jain and N. Mohan, “Dynamic modeling, experimental characterization, and verification for SRM operation with simultaneous two-phase excitation,” *IEEE Trans. Ind. Electron.*, vol. 53, no. 4, pp. 1238–1249, Jun. 2006.

[15] R. Mikail, I. Husain, and M. Islam, Finite element based analytical model for controller development of switched reluctance machines, in Proceedings of the Energy Conversion Congress and Exposition (ESSE 2013), Denver, pp. 920-925, September 2013.

[16] D. S. Mihic, M. V. Terzic, and S. N. Vukosavic, “A New Nonlinear Analytical Model of the SRM With Included Multiphase Coupling,” *IEEE Trans. Energy Convers.*, 2017, 32, (4), pp. 1322-1334.

ABSTRACT

To improve performance, the operation of a switched reluctance motor (SRM) requires simultaneous excitation of multiple motor phases. Since the magnetic polarity of excited phases can be the same or different, the influence of magnetic polarity on the flux linkages of 8/6 SRM was analyzed in this paper in detail. The analysis is performed based on static characteristics obtained using a machine model in a Finite Element Method (FEM) software. Furthermore, considering that the magnetic symmetry between phases cannot be achieved in an 8/6 SRM when using an Asymmetrical Half-Bridge Converter (AHBC), the resulting phase interactions are highly pronounced and are studied by analyzing waveforms of phase currents and torque.

Analysis of influence magnetic phase interaction on the characteristics of 8/6 SRM

Dragan S. Mihić,
Mladen V. Terzić,
Žarko V. Koprivica,
Bogdan M. Brković

Skin effect implementation in parameterized winding function model of an induction motor

Aldin Kajević, Mario Mezzarobba, Alberto Tessarolo, *Senior Member, IEEE* and Gojko Joksimović, *Senior Member, IEEE*

***Abstract* — The paper develops a method for skin effect implementation in recently derived parameterized winding function model of cage rotor induction motor. In that model number of rotor bars is free parameter. For any different number of rotor bars, rotor slot dimensions are different in order to preserve the total rotor copper volume but the slot shape is preserved. By defining the function of slot shape and using multilayer approach, rotor bar resistance and slot reactance can be calculated for any actual rotor speed and any number of rotor bars. The results from the model are given for two different number of rotor bars.**

***Index Terms* — Cage rotor induction motor, Winding function, Parameterized winding function, Multilayer approach, Skin effect.**

I. INTRODUCTION

The skin effect is a well-known and well described phenomenon that occurs in all conductors through which alternating current flows. This effect leads to the redistribution of current across the conductor cross section, which has an effect similar to reducing the cross-section area of the conductor. Non-uniform distribution is more and more significant as AC current frequency grows. The skin effect is usually undesirable because it leads to an increase of Joule losses and thus to increased heating of the conductors.

This effect is especially interesting in cage induction motors because it may have a positive effect. As it is well known from the basic principles of operation of an induction motor, the highest frequency in the rotor bars occurs at the motor startup and therefore the greatest bar resistance occurs during the motor starting. This is desirable because it leads to an increase in the value of the starting torque. On the contrary, when the motor rotates at rated speed, the slip frequency is very small and the increase in resistance due to the skin effect is negligible. By other words, rotor bar current distribution is uniform in that case. On the other side, the skin effect leads to a decrease in rotor bar leakage inductance.

Quantitative measures of skin effect are correction factors for resistance and leakage inductance. The resistance correction factor is the ratio of Joule losses in two cases: AC and DC case. Similarly, the leakage inductance correction factor is the ratio of magnetic energy in two cases: AC and DC case.

In a recently developed parameterized winding function (PWF) model, [1], where number of rotor bars and its skewing angle appears as free parameters, skin effect was neglected. The reason for that was in the fact that mentioned model is up to now predominantly used for analysis of rotor slot harmonics appearance in stator current spectrum, in steady state conditions. By other words, PWF model was up to now primarily used for purpose of finding the best possible solution for number of rotor bars from the electromagnetic torque ripple point of view in steady state conditions, [2], [3], [4], [5], [6], [7]. In order to define a more comprehensive model that would be applicable to transient conditions too, this effect should certainly be considered, and this is the real and basic motivation of this paper. The skin effect in this paper is considered by multilayer approach. In both the analyzed cases, rotors with Q_r=22 and Q_r=28 bars, skewed rotor bars are analyzed where the angle of skewing is equal to one stator slot pitch, $\gamma=2\pi/Q_s$, where Q_s is number of stator slots, [7].

II. BASICS OF PWF MODEL

PWF model enables changes of number of rotor bars in cage rotor induction motor by preserving its rated power, main machine dimensions and stator winding design. Additionally, the model enables changes in skewing angle of rotor bars. Both parameters are freely selectable variables in that model, [1].

The main idea is preserving the volume of rotor cooper (more exactly, rotor aluminum) for any different number of rotor bars that have a real sense. Therefore, when changing the number of rotor bars, Q_r, where nothing changes on the stator side, the cross-sectional area of the bar and end-ring must be changed in order to preserve the rated power of the motor, Fig 1. In order for the motor to develop the same power, the following equations must be satisfied, [1]:

$$Q_r R_b I_b^2 = Q_{r\_new} R_{b\_new} I_{b\_new}^2 \tag{1}$$

$$Q_r R_b \left(\xi \frac{2k_{w1} w_1 m_1}{Q_r} I_{1rated} \right)^2 = Q_{r\_new} R_{b\_new} \left(\xi \frac{2k_{w1} w_1 m_1}{Q_{r\_new}} I_{1rated} \right)^2 \tag{2}$$

Gojko Joksimović and Aldin Kajević are with Faculty of Electrical Engineering, University of Montenegro, Cetinjski put b.b., 81000 Podgorica, Montenegro (Gojko.Joksimovic@ucg.ac.me, Aldin.Kajevic@ucg.ac.me).
Alberto Tessarolo and Mario Mezzarobba are with Department of Engineering and Architecture, University of Trieste, Via Alfonso Valerio, 10-34127, Trieste, Italy (atessarolo@units.it, mmezzarobba@units.it).

$$\xi \cong 0.8\cos\varphi_n + 0.2 \tag{3}$$

from which new rotor bar resistance and cross section area result as follows:

$$R_{b\_new} = \frac{Q_{r\_new}}{Q_r} R_b \tag{4}$$

$$A_{b\_new} = \frac{Q_{r\_new}}{Q_r} A_b \tag{5}$$

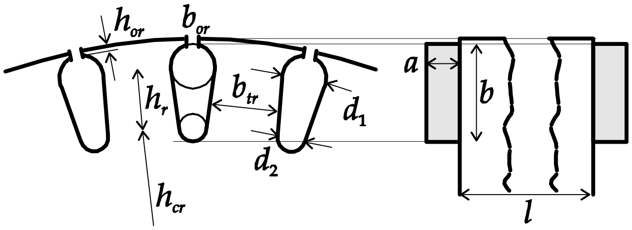

Fig. 1. Shape and dimensions of the rotor bar and the end-ring

In this way, rotor slot dimensions are determined for each new number of bars:

$$d_1 = \frac{\pi\left(D_{er} - 2h_{or}\right) - Q_r b_{tr}}{\pi + Q_r} \tag{6}$$

$$d_2 = \sqrt{\frac{8CA_b - \left(C\pi + 8\right)d_1^2}{C\pi - 8}} \tag{7}$$

$$h_r = \frac{d_1 - d_2}{2\tan\left(\pi/Q_r\right)} \tag{8}$$

$$b_{tr} \cong \frac{B_g \tau_r}{K_{Fe} B_{tr}} = \frac{B_g \pi D_r}{K_{Fe} B_{tr} Q_r} \tag{9}$$

$$C = 4\tan\left(\pi/Q_r\right) \tag{10}$$

III. MULTILAYER APPROACH

There are several ways in which skin effect i.e. correction factors for resistance and leakage inductance can be derived. For some simple shapes of slots there are analytical expressions while for more complicated shapes the bar is divided into several segments along the height of the bar - method known as the multilayer approach, [8]. The skin effect can also be considered using models based on the finite element method [9].

The multilayer approach method and a way of its implementation that is applicable in the PWF model is discussed here. The implementation of this method is usually time consuming and does not allow for a simple change in the dimensions and number of segments being analyzed. Here the previous problem was overcome by defining the function of the slot shape.

One of the possible ways to calculate skin effect in rotor bars of cage induction motor is to divide the bar into N layers, along the bar height. All layers are of the same height, Δh, but, in the general case, as a consequence of the shape of the rotor bar (rotor slot) and the position of the layer, the layers are of different widths, b_j, j=1, 2, 3, ..., N.

Each layer of the rotor bar is considered as a separate conductor of resistance R_j through which the current $\underline{I}_j$ flows. For the n-th layer, according to Faraday's law of electromagnetic induction, the following voltage equation can be written,

$$R_n \underline{I}_n - R_{n+1}\underline{I}_{n+1} = -js\omega_s \Delta\underline{\Phi}_n \tag{11}$$

where R_n, R_{n+1} and $\Delta\Phi_n$ are defined as follows:

$$R_n = \frac{1}{\sigma_{Al}} \frac{l}{b_n \Delta h} \tag{12}$$

$$R_{n+1} = \frac{1}{\sigma_{Al}} \frac{l}{b_{n+1} \Delta h} \tag{13}$$

$$\Delta\underline{\Phi}_n = \frac{\mu_0 l \Delta h}{b_n} \sum_{j=1}^{n} \underline{I}_j \tag{14}$$

Leakage inductance of the n-th layer is:

$$L_n = \frac{\mu_0 l \Delta h}{b_n} \tag{15}$$

Taking into account (14) from (11) we now obtain:

$$\underline{I}_{n+1} = \frac{R_n}{R_{n+1}} \underline{I}_n + j\frac{s\omega_s L_n}{R_{n+1}} \sum_{j=1}^{n} \underline{I}_j \tag{16}$$

Using the previous expression and knowing the current in the first layer, currents in all other layers can be obtained. To the current $\underline{I}_1$ one can assign an arbitrary value as it has no effect on the value of the final resistance and leakage inductance coefficients. These coefficients depend only on the slip frequency, bar shape and its dimensions.

After assigning a value to the current in the first layer, the currents in all other layers can be determined by iterative application of expression (16). When the currents in all layers are known, the value of total Joule losses in the bar can be determined taking into account the distribution of currents in the layers determined in the aforementioned manner, which is a consequence of the alternating current in the bar:

$$P_{AC} = \sum_{j=1}^{N} R_j \left|\underline{I}_j\right|^2 \tag{17}$$

Magnetic energy stored in the rotor slot can be defined in a similar way by taking into account the distribution of currents in the layers:

$$W_{AC} = \frac{1}{2}\sum_{j=1}^{N} L_j \left| \sum_{i=1}^{j} \underline{I}_i \right|^2 \tag{18}$$

If the total rms value of the bar current is defined as follows,

$$I_b = \left| \sum_{j=1}^{N} \underline{I}_j \right| \tag{19}$$

then we can calculate losses and magnetic energy in the bar when a direct current of the same intensity is supposed to flow through it,

$$P_{DC} = \sum_{j=1}^{N} R_j I_{jDC}^2 \tag{20}$$

where:

$$I_{jDC} = \frac{I_b}{A_b} b_j \Delta h \tag{21}$$

$$W_{DC} = \frac{1}{2}\sum_{j=1}^{N} L_j \left(\sum_{i=1}^{j} I_{iDC} \right)^2 \tag{22}$$

Correction coefficients for the resistance and inductance of the rotor bar are finally:

$$K_R = \frac{P_{AC}}{P_{DC}} = \frac{\sum_{j=1}^{N} R_j \left| \underline{I}_j \right|^2}{\sum_{j=1}^{N} R_j I_{jDC}^2} \tag{23}$$

$$K_L = \frac{W_{AC}}{W_{DC}} = \frac{\sum_{j=1}^{N} L_j \left| \sum_{i=1}^{j} \underline{I}_i \right|^2}{\sum_{j=1}^{N} L_j \left(\sum_{i=1}^{j} I_{iDC} \right)^2} \tag{24}$$

IV. METHOD IMPLEMENTATION

The first step in applying the method is to determine the dimensions of each layer i.e. to determine the height Δh and the widths of the layers, b_j. One way to achieve this is by defining the slot shape function. The slot shape function for the slot shape used in this model is obtained using the analytical expressions for a circle and a line through two points. The coordinates of the points and the dimensions of the diameters that appear in the analytical expressions are recalculated for each new number of bars. A similar procedure can be applied to all slot shapes consisting of simple geometric shapes for which there are analytical expressions, which is the most common case. For the shape of the slot used in this model, the following function can be defined,

$$f(x) = \begin{cases} \sqrt{x(d_2 - x)}; \ 0 \le x \le 0.5 d_2 \\ \dfrac{(d_1 - d_2)(2x - d_2) + 2 d_2 h_r}{4 h_r}; \ 0.5 d_2 < x \le 0.5 d_2 + h_r \\ 0.5\sqrt{d_1^2 - (2x - d_2 - 2h_r)^2}; \ 0.5 d_2 + h_r < x \le 0.5(d_1 + d_2) + h_r \end{cases} \tag{25}$$

where x is the position of the layer measured from the bottom of the slot upwards, Fig. 2.

If the height of the layers is Δh, same for all of them, and x is defined as follows,

$$\Delta h = \frac{0.5(d_1 + d_2) + h_r}{N} \tag{26}$$

$$x = 0,\ \Delta h,\ 2\Delta h,\ \ldots\ N\Delta h \tag{27}$$

then the widths of the layers b_j can be obtained by applying (25) for different values of x:

$$b_j = 2 f(x_j) \tag{28}$$

Once the dimensions of all layers have been defined, the procedure for determining the correction coefficients can be applied. For the shape of the bar used in this model, a graph of the dependency of the correction factors upon slip has been obtained, as shown in Fig. 3.

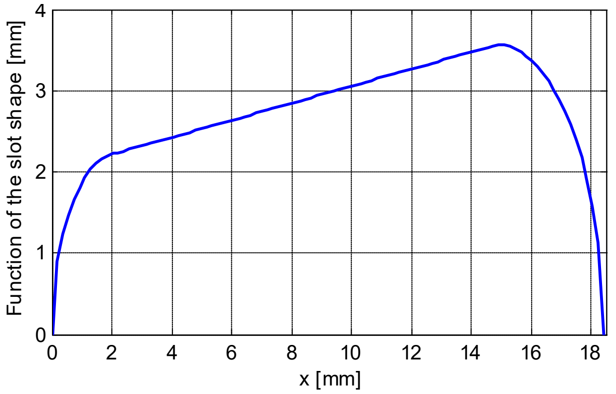

Fig. 2. Rotor slot shape function. Number of rotor bars, Q_r=30.

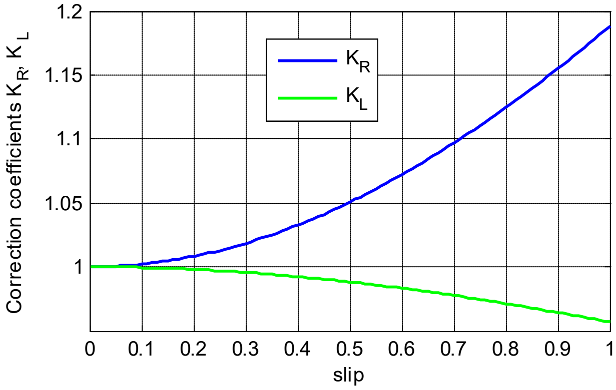

Fig. 3. Correction coefficients as a function of slip. Number of rotor bars Q_r=30.

V. RESULTS

Using the previous expressions, correction coefficients can be determined for different bar numbers. The procedure for determining the correction factors can be incorporated into the parameterized dynamic model based on the winding function theory (PWF model) [4]. Figures below show comparisons of the results obtained from this model without and with the skin effect taken into account, for two different numbers of rotor bars, Q_r=22 and Q_r=28. In both analyzed cases higher electromagnetic torque is an obvious consequence and therefore, the steady-state rotor speed is reached faster.

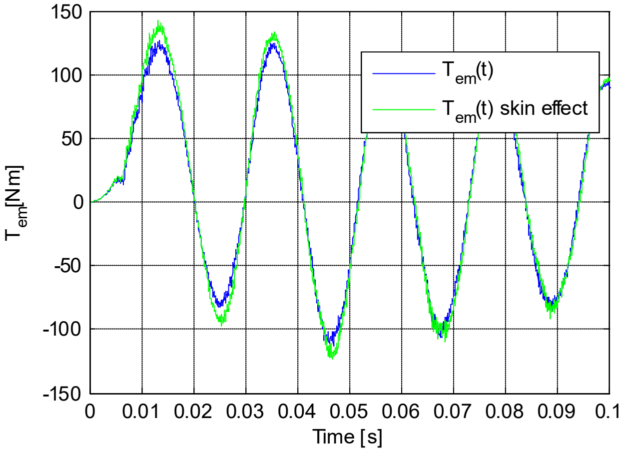

Fig. 4. Electromagnetic torque during the no-load speed-up of the motor, Q_r=22

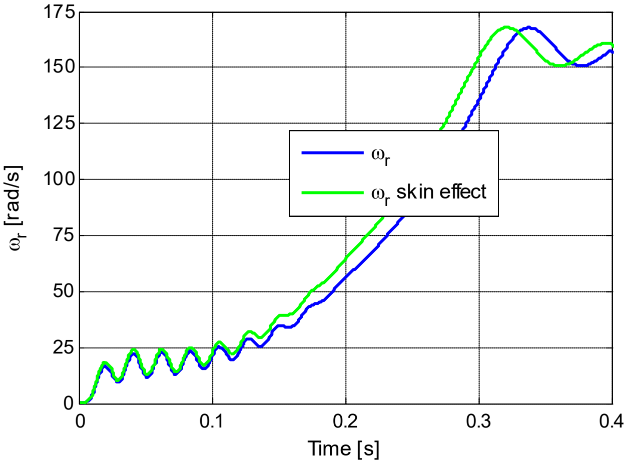

Fig.5. Rotor speed during the no-load, speed-up of the motor, Q_r=22

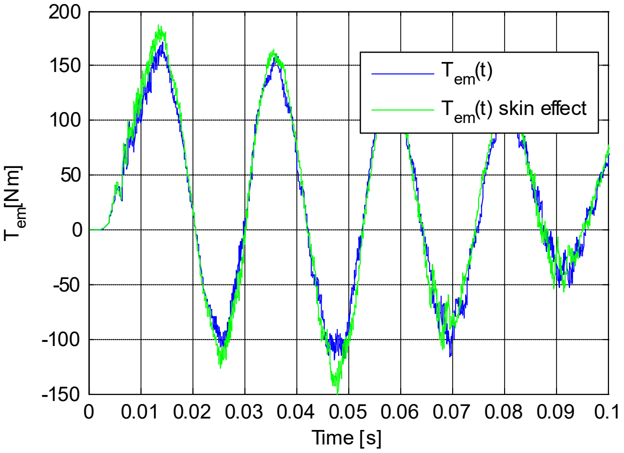

Fig. 6. Electromagnetic torque during the no-load speed-up of the motor, Q_r=28

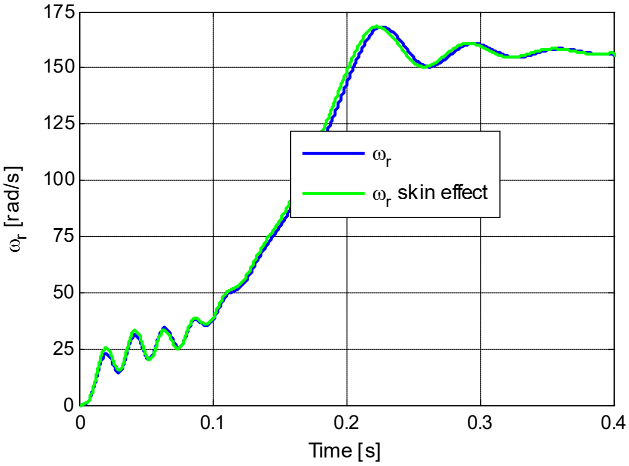

Fig. 7. Rotor speed during the no-load speed-up of the motor, Q_r=28

VI. CONCLUSION

Multilayer approach method and a modified way of its implementation that allows a simple change in the dimensions of the slot as well as the number of segments used in the analysis are presented in this paper. This was realized by defining the function of the slot shape. The method was incorporated in parameterized dynamic model based on the winding function theory. The results from the model are shown and illustrated. The influence of the skin effect on the motor starting torque can be clearly seen from the presented results for two different number of rotor bars.

This model does not consider saturation of ferromagnetic material. Further improvements to the model are planned, one of which is to take into account saturation. It is also planned to compare the results with the results obtained using the FEM model, which can consider the saturation effects.

APPENDIX

TABLE I

MOTOR RATED VALUES, MOTOR AND ROTOR SLOT GEOMETRICAL PARAMETERS

P_r [kW]	11	Q_s	36
U_{LL} [V]	400	Q_r	30
f [Hz]	50	y/τ	7/9
I_r [V]	17.6	q	3
$\cos\varphi_r$	0.83	W_1	108
η_r	0.91	D_{is} [mm]	145.724
p	2	L [mm]	171.677
R_s [Ω]	0.294	g [mm]	0.397
$L_{\sigma s}$ [mH]	2.919	d_1 [mm]	7.132
R_b [μΩ]	64.49	d_2 [mm]	4.480
R_{er} [μΩ]	1.545	h_r [mm]	12.615
L_b [nH]	398.58	A_b [mm^2]	101.092

ACKNOWLEDGMENT

This research was conducted on Faculty of Electrical Engineering, University of Montenegro and was financed by the Ministry of Science of Montenegro through the research project “Induction motor efficiency improvement through optimal electromagnetic design solutions - IMEI”. Partner on the project is Department of Engineering and Architecture, University of Trieste, Italy.

REFERENCES

[1] G. Joksimović, “Dynamic model of cage induction motor with number of rotor bars as parameter,” *J. Eng.*, vol. 2017, no. 6, pp. 205–211, Jun. 2017.

[2] G. Joksimović, J. I. Melecio, P. M. Tuohy, S. Djurović, „Towards the optimal ‘slot combination’ for steady-state torque ripple minimization: an eight-pole cage rotor induction motor case study”, Electrical Engineering, Springer, vol. 102, Issue 1, pp. 293-308, 2020.

[3] G. Joksimović, M. Mezzarobba, A. Tessarolo, E. Levi, „Optimal Selection of Rotor Bar Number in Multiphase Cage Induction Motors”, IEEE Access, vol. 8, pp. 135558-135568, 2020.

[4] G. Joksimović, E. Levi, A. Kajević, M. Mezzarobba, A. Tessarolo, „Optimal Selection of Rotor Bar Number for Minimizing Torque and Current Pulsations Due to Rotor Slot Harmonics in Three-phase Cage Induction Motors”, IEEE Access, vol. 8, pp. 228572-228585, 2020.

[5] G. Joksimović, A. Kajević, M. Mezzarobba, A. Tesarolo, “Optimal rotor bars number in four pole cage induction motor with 36 stator slots - part I: numerical modeling“, ICEM 2020, Gothenburg, Sweden, 2020.

[6] G. Joksimović, A. Kajević, M. Mezzarobba, A. Tesarolo, “Optimal rotor bars number in four pole cage induction motor with 36 stator slots - part II: results“, ICEM 2020, Gothenburg, Sweden, 2020.

[7] G. Joksimović, A. Kajević, S. Mujović, T. Dlabač, V. Ambrožič, A. Tesarolo, “Rotor bars skewing impact on electromagnetic pulsations in cage induction motor“, IcEtran 2019, Srebrno jezero, Srbija, 2019.

[8] I. Boldea, S. A. Nasar, The induction machine handbook, CRC Press, 2010.

[9] S. Williamson and M. J. Robinson, “Calculation of cage induction motor equivalent circuit parameters using finite elements,” IEE Proc. B Electr. Power Appl., vol. 138, no. 5, pp. 264–276, 1991.

Operation Analysis and Determination of Virtual Synchronous Machine Model Parameters

Nikola Krstić, Milutin Petronijević, Filip Filipović

***Abstract* –This paper presents the concept, model and simulation of virtual synchronous machine (VSM) operation and proposes a methodology for its parameter values selection. VSM was synchronized to the grid and its responses to given references of active and reactive powers were obtained, for different values of VSM parameters. Responses of grid-feeding and grid-supporting model of VSM, were considered. Special attention is paid to the formation of control loops for active and reactive power as basic structures in the VSM operation. Based on these control loops, values of VSM parameters are determined by pole adjustment method, which was the basic task of this paper. VSM model and the model of used power grid were made in Matlab/Simulink, in which results presented at the end of the paper, were generated.**

***Keywords* – virtual synchronous machine, power converter, control loop, emulation.**

I. INTRODUCTION

Increased distributed generation, presence of renewable energy sources, as well as the emergence of microgrids in the power system, have led to new ideas and concepts to appear [1]. Many of these concepts include the use of power electronics to increase the flexibility and range of power grids, and one of them is virtual synchronous machine (VSM). This concept arose from the need to bring the operation of three-phase power converters closer to the operation of synchronous machines [2], primarily by introducing virtual inertia. Doing this, the control operation of energy converters has not changed significantly, and it is still based on droop control (which is inherited from synchronous machines), but now a certain inertia is included in it. Addition of inertia, which emulates moment of inertia of the rotor of synchronous machine and the inertia of inductance in excitation circuit, increases stability of the grid and its resistance to various types of disturbances and power imbalances [3]. This is especially important in grids where large proportion of generated power comes from power sources connected via power converters [4].

In this paper, structure and concept of operation of VSM model [3],[5],[6] are presented first, where the equations of mathematical model of synchronous machine, that is going to be emulated with VSM, are written. After that, the methodology for determining the values of VSM parameters was presented. It is clear that values of VSM model parameters will largely determine its response [7] to the given references, which is why their proper selection, in order to meet a particular requirement, is the main task of this paper. In order to make this possible, VSM model was decomposed into two basic structures, one includes active power-frequency regulation, and the other reactive power-voltage regulation [5]. In this way, control loops for active and reactive power are formed in the paper, on the basis of which values of VSM parameters are determined, using pole adjustment method. Number of these parameters differs in the case of grid-feeding and grid-supporting model of VSM, that depends on the role which energy converter have in the grid [8]. Grid-feeding energy converter only meets power requirements regardless of the grid voltage and frequency, while grid-supporting one, in addition to that, supports regulation of voltage and frequency in the grid. That is way, in this paper, two additional coefficients in the grid-supporting model of VSM are used, one for grid voltage and the other for grid frequency control. Three basic parameters, common to both VSM models, are: moment of inertia, damping factor and ratio coefficient of reactive power to change of excitation flux [3]. In this paper, VSM is connected to the grid via LCL filter and the grid is modeled by real voltage generator.

Results presented at the end of the paper contain responses of certain quantities, for different values of parameters [9] in VSM model for grid-feeding and grid-supporting structure.

II. VSM MODEL

Basic idea behind the concept of VSM is to create an emulator which will ensure that three-phase power converter behaves like a synchronous machine towards the grid. That is, it is necessary to equalize voltages at the end of the power converter with electromotive forces that would occur in the operation of a synchronous machine. Since the electromotive forces in synchronous machine are determined by the first derivative of excitation flux, it is clear that VSM model must take into account relations for excitation flux and angular frequency. In this paper, mathematical model of synchronous machine with cylindrical rotor and without losses, is used to form VSM model. Excitation flux through the phase windings of synchronous machine is given by equations:

$$\psi_{fA} = \psi_{fm}\cos(\omega t) \tag{1}$$

$$\psi_{fB} = \psi_{fm}\cos(\omega t - \tfrac{2\pi}{3}) \tag{2}$$

Nikola Krstić is with the Department of Power Engineering, Faculty of Electronic Engineering, University of Niš, Aleksandra Medvedeva 14, 18000 Niš, Serbia, E-mail: nikola.krstic@elfak.ni.ac.rs.

Milutin Petronijević is with the Department of Power Engineering, Faculty of Electronic Engineering, University of Niš, Aleksandra Medvedeva 14, 18000 Niš, Serbia, E-mail: milutin.petronijevic@elfak.ni.ac.rs.

Filip Filipović is with the Department of Power Engineering, Faculty of Electronic Engineering, University of Niš, Aleksandra Medvedeva 14, 18000 Niš, Serbia, E-mail: filip.filipovic@elfak.ni.ac.rs.

$$\psi_{fC} = \psi_{fm}\cos(\omega t + \frac{2\pi}{3}) \tag{3}$$

Based on excitation flux, electromotive forces in phase windings are determined according to the vector equation:

$$\vec{e}_f = -\frac{d\vec{\psi}_f}{dt} \tag{4}$$

Based on (4), electromotive forces in phase windings can be obtain using equations:

$$e_{fA} = \omega\psi_{fm}\sin(\omega t) - \frac{d\psi_{fm}}{dt}\cos(\omega t) \tag{5}$$

$$e_{fB} = \omega\psi_{fm}\sin(\omega t - \frac{2\pi}{3}) - \frac{d\psi_{fm}}{dt}\cos\left(\omega t - \frac{2\pi}{3}\right) \tag{6}$$

$$e_{fC} = \omega\psi_{fm}\sin(\omega t + \frac{2\pi}{3}) - \frac{d\psi_{fm}}{dt}\cos\left(\omega t + \frac{2\pi}{3}\right) \tag{7}$$

Angular frequency of VSM appearing in (1)-(7) is found by motion equation of rotor of VSM:

$$\frac{d\omega}{dt} = \frac{1}{J}(\frac{P_{set}}{\omega} - \frac{P}{\omega} - D_p(\omega - \omega_G)) \tag{8}$$

Where: J −moment of inertia of rotor of VSM, ω −angular frequency of VSM, ω_G −angular frequency of the grid, D_p −damping factor, P_{set} −active power reference (generated mechanical power), P −active power injected into the grid by VSM (active power of consumption).
It must be noted that in (8) generated mechanical power of VSM is identified as active power reference and generated active power is identified as active power injected into the grid. This identifications can be done because model of VSM emulates synchronous machine without losses and active power losses in LCL filter are negligible. In addition to the angular frequency, it is necessery to determine the intensity of excitation flux in VSM. This is done on the basis of excitation regulation in synchronous machine, using reactive power eror:

$$\frac{d\psi_f}{dt} = D_q(Q_{set} - Q) \tag{9}$$

Where: ψ_f −excitation flux in phase windings of VSM, D_q −ratio coefficient of reactive power to change of excitation flux, Q_{set} −reactive power reference, Q −reactive power injected into the grid by VSM.

Based on (5)-(9), grid-feeding model of VSM is formed in Matlab/Simulink. In the case of grid-supporting model, additional links for grid voltage and frequency regulation must be considered. In this paper, grid is modeled with real voltage generator whose equivalent impedance has big *R/X* ratio, that is usually the case in low voltage networks. This would mean that the grid voltage regulation in the point of connection of VSM to the grid is most efficiently achieved using injected active power. On the other hand, the best way to regulate grid frequency in the point of connection is injecting reactive power. This is based on the voltage drop formula between node *i* and node *j* connected with branch containing active resistance *R* and reactance *X*, when active power P_{ij} and reactive power Q_{ij} flows from node *i* to node *j*.

$$U_i - U_j = \frac{P_{ij}R + Q_{ij}X}{U_i} + j\frac{P_{ij}X - Q_{ij}R}{U_i} \tag{10}$$

Considering (10), in *R* dominant type of grids, voltage in connection point (U_i) is increased when injected active power (P_{ij}) is increased, and the phase ange (frequency) is increased when injected reactive power (Q_{ij}) is decresed [1],[8]. Considering this, for grid-supporting model, (8)-(9) become:

$$\frac{d\omega}{dt} = \frac{1}{J}(\frac{P_{set} - P + K_V(V_{ref} - V_G)}{\omega} - D_p(\omega - \omega_G)) \tag{11}$$

$$\frac{d\psi_f}{dt} = D_q(Q_{set} - Q - K_\omega(\omega_{ref} - \omega_G)) \tag{12}$$

Where: V_G −grid voltage, V_{ref} −grid voltage reference, K_ω −control coefficient of grid angular frequency, K_V −control coefficient of grid voltage, ω_{ref} −grid angular frequency reference.
Signals of obtained electromotive forces given by (5)-(7) are used to generate voltage at the end of the energy converter, what can be seen in Fig. 1, where grid-supporting model of VSM is presented, as more general one.

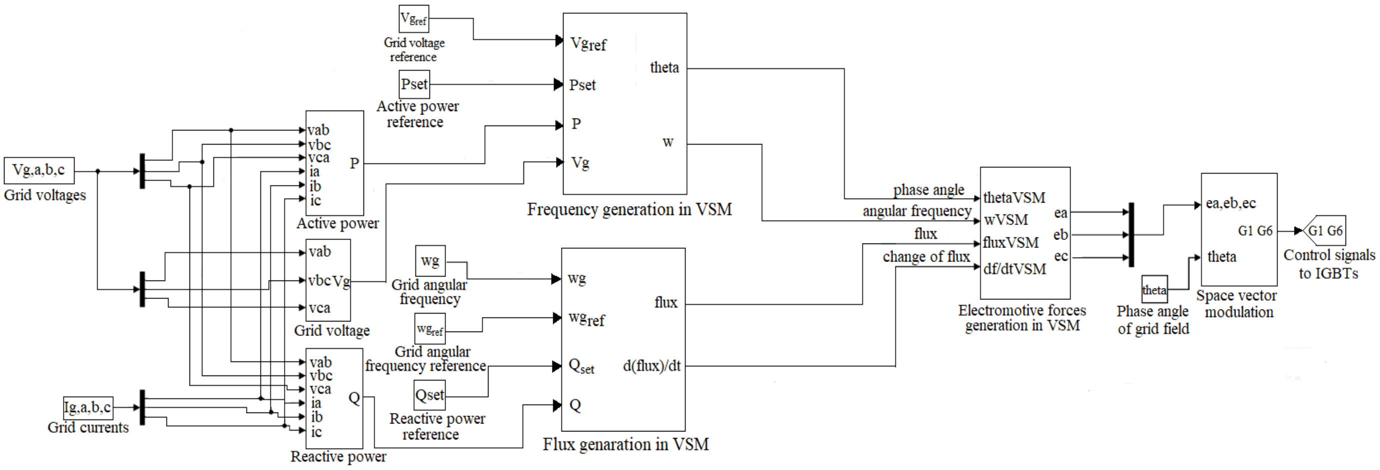

Fig. 1. Block diagram of grid-supporting model of VSM

III. FORMATION OF CONTROL LOOPS AND VSM PARAMETER DETERMINATION

In order to determine the parameters in VSM model, it is necessary to form appropriate control loops. Due to the droop control, this can be most easily and efficiently done by splitting VSM model into two independent units, one related to active power and other to reactive power regulation. Based on these units, control loops for active and reactive power are formed, shown in Figs 2 and 3, respectively. During their formation, certain assumptions were adopted in order to achieve linearization and complete independence between the loops, and thus simplify the calculation of VSM parameters. This refers to the use of indicated values for the grid voltage and angular frequency of VSM instead of their actual values. Also, fixed value of electromotive force in the regulation of active power and fixed load angle in regulation of reactive power is used. Second member in expressions for electromotive force (5)-(7), is neglected.

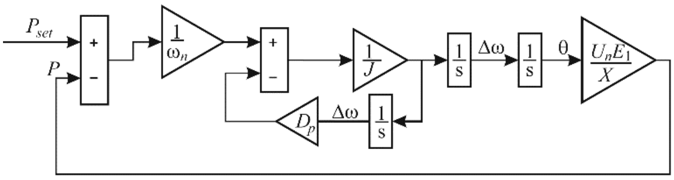

Fig. 2. Active power control loop

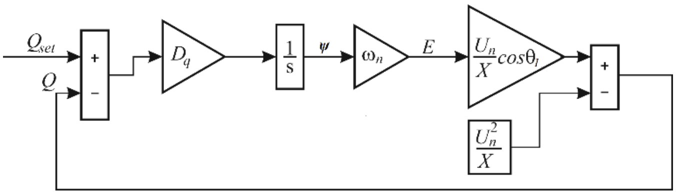

Fig. 3. Rective power control loop

Linearization was also achieved by replacing the sinusoidal function with its argument in expression for active power (13) and using fixed value for cosine function in expression for reactive power (14). These assumptions are justified if deviations of grid operating voltage and VSM frequency from their indicated values are small and if load angle does not take big changes. Also, product of flux and angular frequency of VSM has to be an order of magnitude greater than the change of VSM flux. All of this, to a large extent, should be met if values for active and reactive power are set in normal operating mode. Biger errors can occur by using inadequate fixed values for electromotive force and load angle of VSM in control loops. In order to partially overcome this, mentioned quantities were calculated on the basis of set values for active and reactive power.

In this paper, VSM emulates the operation of synchronous machine without losses and with cylindrical rotor, which active and reactive power can be determined by expressions:

$$P = \frac{U \cdot E}{X} sin\theta \qquad (13)$$

$$Q = \frac{U \cdot E}{X} cos\theta - \frac{U^2}{X} \qquad (14)$$

Where: P −active power that VSM injects into the grid, Q −reactive power that VSM injects into the grid, U −grid voltage, E −electromotive force of VSM, θ −load angle, X −equivalent reactance between electromotive force and voltage.

Taking into account mentioned assumptions while forming control loops for active and reactive power, (13) and (14) become:

$$P = \frac{U_n \cdot E_1}{X} \theta \qquad (15)$$

$$Q = \frac{U_n \cdot E}{X} cos\theta_1 - \frac{U_n^2}{X} \qquad (16)$$

Where E_1 and θ_1 are fixed values for electromotive force and load ange, determined by set values of active and reactive power, using expressions:

$$E_1 = \frac{\frac{Q_{seti}+Q_{seti-1}}{2} \cdot X + U_n^2}{U_n} \qquad (17)$$

$$\theta_1 = sin^{-1}\left(\frac{\frac{P_{seti}+P_{seti-1}}{2} \cdot X}{U_n \cdot E_1}\right) \qquad (18)$$

Where indices i and $i-1$ in active and reactive power references mark current and previous reference, respectively.

Equivalent reactance between electromotive force of VSM and grid voltage, which appears in expressions for active and reactive power, is the equivalent reactance of LCL filter, and can be found as:

$$X = X_1 - \frac{X_2 \cdot X_C}{X_2 - X_C} \qquad (19)$$

Where: X_1 −reactance of the inductance near the VSM ($X_1 = \omega L_1$), X_2 −reactance of the inductance near the grid ($X_2 = \omega L_2$), X_C −reactance of the capacitor ($X_C = 1/C\omega$). Delay due to the change of currents in the network branches is neglected in control loops, because it is much less than what is needed to change flux or frequency and practically does not affect the dinamics of the system. Based on the control loop for active power, transfer function between the set and actual active power injected into the grid by VSM, can be found as:

$$\frac{P}{P_{set}} = F_p(s) = \frac{\frac{U_n E_1}{X \omega_n J}}{S^2 + \frac{D_p}{J} S + \frac{U_n E_1}{X \omega_n J}} \qquad (20)$$

In this paper, pole adjustment method is used, which means that VSM parameters are calculated from desired values of characteristic parameters that determine the response of second order circuit. General expression for second order transfer function is:

$$F_s(s) = \frac{\omega_c^2}{s^2 + 2\xi \omega_C s + \omega_C^2} \qquad (21)$$

Where ω_C is the natural frequency (bandwidth of second order circuit) and ξ is the damping factor of second order circuit. Comparing (20) and (21), moment of inertia and damping factor of VSM can be determined based on the desired damping factor and bandwidth of second order circuit:

$$J = \frac{U_n \cdot E_1}{X \cdot \omega_n \cdot \omega_C^2} \qquad (22)$$

$$D_p = 2 \cdot \xi \cdot \omega_c \cdot J \qquad (23)$$

Same analogy can be used for reactive power control loop, whose transfer function is given by expression:

$$\frac{Q}{Q_{set}} = F_q(s) = \frac{1}{1+\frac{X}{D_q \omega_n U_n \cos\theta_1}s} \qquad (24)$$

General form of the first order transfer function is:

$$F_s(s) = \frac{1}{1+sT} \qquad (25)$$

Where T is the time constant of the first order circuit. Based on the desired value of time constant, ratio coefficient D_q can be found as:

$$D_q = \frac{X}{T \cdot \omega_n \cdot U_n \cdot \cos\theta_1} \qquad (26)$$

Now, values are determined for all required parameters of grid-feeding model of VSM. Values for an additional two parameters in grid-supporting model of VSM are determined based on the desired error between set and actual values of injected powers, during the deviation of grid voltage and frequency from the reference values, in steady state. This is shown in (27) and (28):

$$K_V = -\frac{P-P_{ref}}{V-V_{ref}} \qquad (27)$$

$$K_\omega = \frac{Q-Q_{ref}}{\omega-\omega_{ref}} \qquad (28)$$

Expressions (27) and (28) are obtain using (11) and (12) for steady state. Determined in this way, control coefficients have positive values. It must be taken into account that (27) and (28) are valid only in active resistance dominant grids, like one used in this paper.

IV. PRESENTATION AND ANALYSIS OF RESULTS

In this section, results related to the response of active and reactive power of VSM for different values of its parameters are presented and analyzed. Used active and reactive power references and the rating of VSM (40kVA) are such that they do not cause major voltage deviations in the formed low voltage grid model. All results were obtained for the case where VSM, powered by storage system DC voltage, is connected to the low voltage grid, modeled by real voltage generator, via LCL filter. This is shown in the form of Matlab/Simulink block in Fig. 4. For the *50 Hz* frequency grid resistance and grid reactance used in the model are: $R_g=0.1126\Omega$ and $X_g=0.0233\Omega$. Voltage generator in grid modeling is fixed 400V, 50Hz voltage source. Reactances of LCL filter are: $X_1=0.6283\Omega$, $X_2=0.1571\Omega$ and capacitor reactance $X_C=27.6791\Omega$ (equivalent reactance is $X=0.785\Omega$).

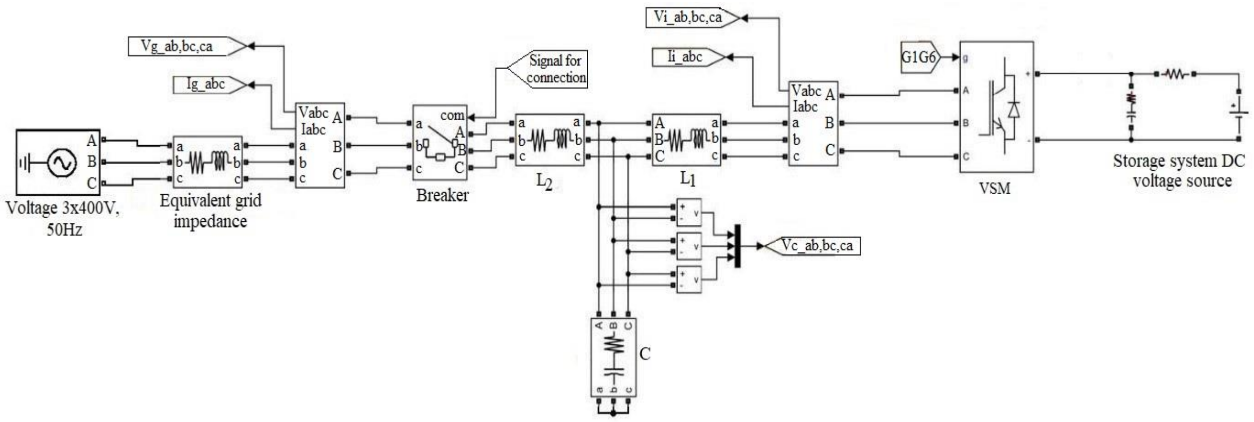

Fig. 4. Block model of power grid to which VSM, powered by storage system DC voltage, is connected via LCL filter

Next six figures show how efficient is the response of active and reactive power of grid-feeding model of VSM and to what extent it matches the desired (expected) responses. Desired response of active and reactive power is determined by chosen values of characteristic parameters ω_C, ξ and T. Based on those three characteristic parameters, using presented methodology, necessary values of parameters in grid-feeding model of VSM are determined, for three different cases, shown in Table I.

TABLE I
CHARACTERISTIC PARAMETERS OF THE DESIRED RESPONSE AND CALCULATED PARAMETERS FOR GRID-FEEDING MODEL OF VSM

Case	Natural frequency ω_C (rad/s)	Damping factor ξ	Time constant T (s)
1	10	0.707	0.15
2	7	1	0.15
3	14	0.5	0.2
Case	Moment of inertia J (kgm^2)	Damping coefficient $D_p(Nms/rad)$	Ratio coefficient $D_q(Wb/sVAr)$
1	6.4458	91.1441	$4.247 \cdot 10^{-5}$
2	13.1548	184.1667	$4.2454 \cdot 10^{-5}$
3	3.2887	46.0417	$3.184 \cdot 10^{-5}$

Figs 5 and 6 show reference, desired and actual response of active and reactive power for the case 1.

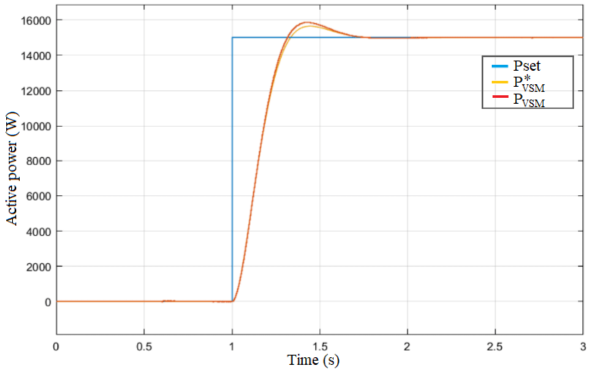

Fig. 5. Reference, desired and actual response of active power in grid-feeding model, case 1

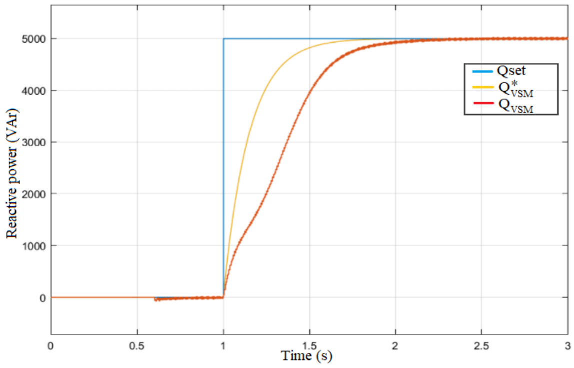

Fig. 6. Reference, desired and actual response of reactive power in grid-feeding model, case 1

Figs 7 and 8 show reference, desired and actual response of active and reactive power for the case 2.

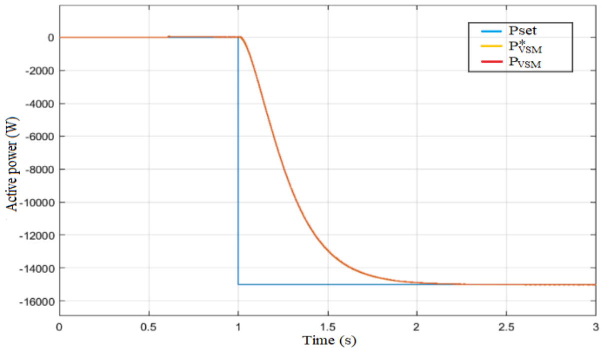

Fig. 7. Reference, desired and actual response of active power in grid-feeding model, case 2

Based on the Figs (5)-(10) it can be concluded that VSM operates efficiently and achieves desired references of active and reactive powers (positive or negative) with high precision. Also, great match between desired (expected) and actual active power response can be seen. In the case of reactive power, matching is not so great when active and reactive power have the same direction, in other cases it is quite good considering the simplicity of the methodology. This can be explained by the fact that voltage and frequency variations, have more affect on the dynamics of reactive than on the active power response, considering (20) and (24). Also, voltage variations are the largest when both powers have the same direction, that is way the worst matching is in the fig. 6.

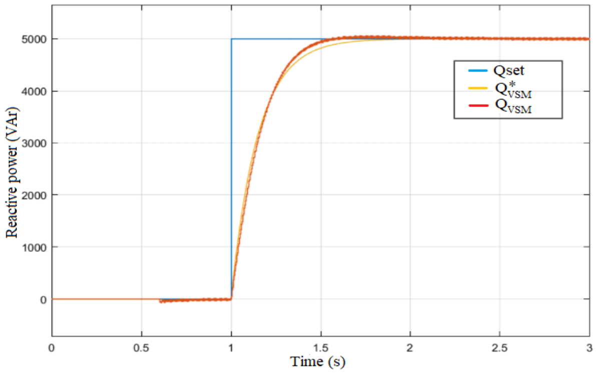

Fig. 8. Reference, desired and actual response of reactive power in grid-feeding model, case 2

Figs 9 and 10 show reference, desired and actual response of active and reactive power for the case 3.

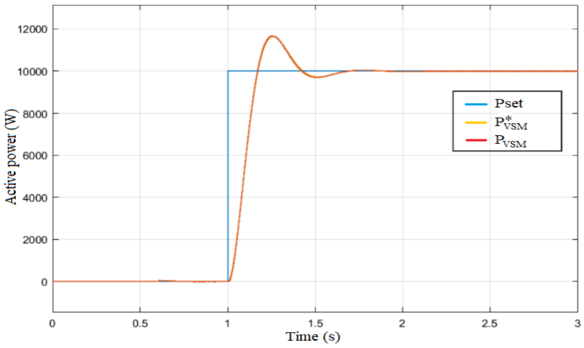

Fig. 9. Reference, desired and actual response of active power in grid-feeding model, case 3

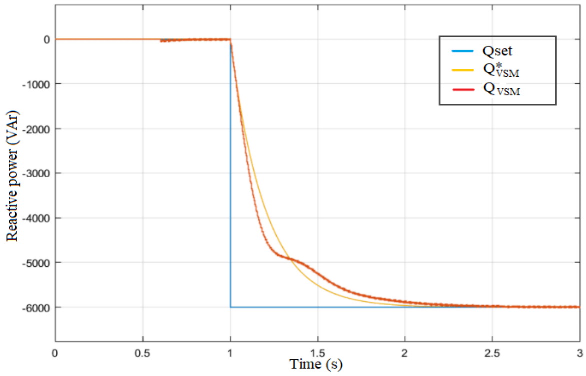

Fig. 10. Reference, desired and actual response of reactive power in grid-feeding model, case 3

In the grid-supporting model, references and actual values of injected powers will not match when there is a deviation in values of grid voltage and frequency compared to their referent values. This is shown in Fig. 11 for reactive and in Fig. 12 for active power.

TABLE II

CHARACTERISTIC PARAMETERS OF THE DESIRED RESPONSE AND CALCULATED PARAMETERS FOR GRID-SUPPORTING MODEL OF VSM

Natural frequency ω_C (rad/s)	Damping factor ξ	Time constant T (s)	Control coefficient $K_V (W/V)$
10	0.707	0.15	10 000
Control coefficient $K_\omega (VArs/rad)$	Moment of inertia $J\,(kgm^2)$	Damping coefficient $D_p (Nms/rad)$	Ratio coefficient $D_q (Wb/sVAr)$
30 000	6.3663	90.0189	$4.24 \cdot 10^{-5}$

Table II contains values of characteristic parameters of the desired response, based on which values of parameters in grid-supporting model of VSM are calculated and also shown in Table II. Figs 11 and 12, are obtained for the case where parameters of grid-supporting model of VSM have values from Table II, and where grid voltage and frequency are below their referent values. High values for control coefficients are used due to fixed voltage source and low network impedance, which do not allow more significant changes in grid voltage and especially in grid angular frequency. There is a noticeable difference in both active and reactive power response shown in Figs 11 and 12, compared with those in Figs 5 and 6, which had the same values for characteristic parameters. This changed dynamics in grid-supporting model is the result of grid voltage and angular frequency errors used as inputs in active and reactive power control loops in which they are not considered in the first place. This means that presented methodology should be primarily used in grid-feeding model of VSM.

Considering the results for grid-feeding VSM model, it can be concluded that grid parameters have negative effect on active and reactive power response and decrease the accuracy of the proposed methodology by changing the voltage and frequency in the point of connection. This also applies to the grid-supporting model of VSM, but in that case voltage and frequency variations, caused by the grid impedance, in addition, enhance voltage and frequency support in the point of connection. Resistive or reactive nature of grid impedance determined which type of power should be used for voltage, and which for frequency support.

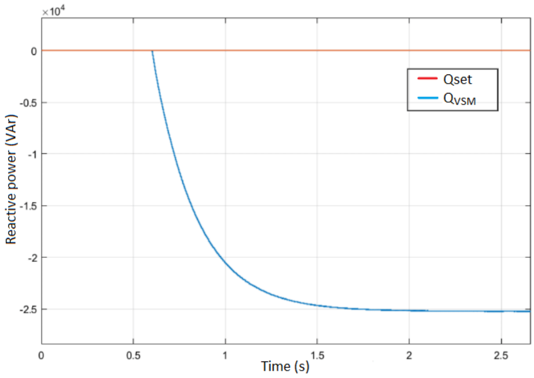

Fig. 11. Referent and actual value of reactive power in grid-supporting model

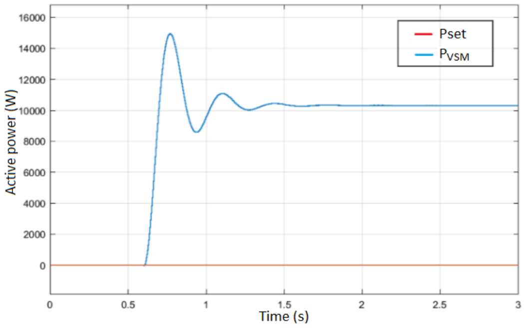

Fig. 12. Referent and actual value of active power in grid-supporting model

V. CONCLUSION

In this paper, model of VSM was made and methodology for determining the values of its parameters is presented and described in detail. Obtained results have shown that VSM is able to efficiently and accurately respond to different requirements of active and reactive powers. Proposed methodology for determining VSM parameter values is simple, and based on obtained results, quite accurate in achieving the desired response, if grid voltage and frequency deviations, due to power injection, are relatively small. Also, results have shown that if more precision in achieving the desired response is needed, proposed methodology should be primarily used in grid-feeding model of VSM. Taking into account the simplicity and efficiency of the presented methodology, its major practical value in real, more complex systems, could be reflected in determining the initial, first step, values of VSM parameters in order to achieve the desired response, which could then be corrected by additional steps, considering the characteristics of a particular system.

REFERENCES

[1] Q. Zhong, T. Hornik, *Control of Power Inverters in Renewable Energy and Smart Grid Integration*, John Wiley & Sons Ltd, Chichester, United Kingdom, 2013, pp. 251-330.

[2] M. Abuagreb, B. Ajao, H. Herbert, B. Johnson, “Evaluation of Virtual Synchronous Generator Compared to Synchronous Generator”, IEEE Power & Energy Society Innovative Smart Grid Technologies Conference (ISGT), pp. 1-5, February 2020.

[3] J. M. Ramirez, E. T. Montalvo, C. I. Nuno, “Modeling, synchronization, and implementation of the virtual synchronous generator: a study of its reactive power handling”, Electrical Engineering, pp. 1605-1619, March 2020.

[4] S. Vukosavić, *Grid-Side Converters Control and Design*, Springer International Publishing, 2018, pp. 211-250.

[5] H. Wu, X. Ruan, D. Yang, X. Chen, W. Zhao, Z. Lv, Q. Zhong, “Small-Signal Modeling and Parameters Design for Virtual Synchronous Generators”, IEEE Transactions on Industrial Electronics, vol. 63, no.7, pp. 4292-4303, July 2016.

[6] Y. Hirase, K. Abe, K. Sugimoto, Y. Shindo, “A Grid Connected Inverter with Virtual Synchronous Generator Model of Algebraic Type”, IEEJ Transactions on Power and Energy, vol. 132, no.4, pp. 371-380, April 2012.

[7] R. Aouini, K. Ben Kilani, B. Marinescu, M. Elleuch “Virtual Synchronous Generator Dynamic Performances”, Internacional Conference on Electrical Science and Technologies in Magreb (CISTEM), pp. 1-6, November 2014.

[8] M. Castilla, L. Garcia de Vicuna, J. Miret, “Control of Power Converters in AC Microgrids”, *Microgrids Desing and Implementation*, Springer Internacional Publishing, pp. 139-170, 2019.

[9] X. Yan, S. Mohamed, D. Li, A. Gadalla, “Parallel Operation of Virtual Synchronous Generators and Synchronous Generators in a Mycrogrid”, Journal of Engineering, vol. 2019, pp. 2635-2642, March 2019.

Design of LLC Resonant Tank in a Low Power DC/DC Power Converter

Katarina Obradović, Emilija Lukić, Jovana Plavšić and Aleksandar Milić

***Abstract*— Photovoltaic power conversion prosperity has put a spotlight on the resonant DC/DC converters. Namely, improved power density and lessened power losses can be achieved due to its soft switching feature. Step by step design procedure of the LLC resonant tank is proposed in this paper. Analysis of the parameters of the tank, capacitor selection and a detailed inductor design are demonstrated thoroughly. Finally, experimental results of the developed 1000 W DC/DC converter with suggested LLC resonant configuration are presented.**

***Index Terms*— DC/DC converter, LLC resonant tank, high frequency, capacitor selection, inductor design**

I. INTRODUCTION

Increased interest in the use of renewable energy sources has inspired the development of new solutions in power electronics. Its unprecedented expansion has resulted in continued advances regarding power conversion's efficiency, safety, as well as the price.

Since photovoltaic (PV) systems represent DC power source, in order to successfully connect them to AC power grid, the use of switching power converters is inevitable. With aspirations to achieve better efficiency of power conversion, Maximum Power Point Tracking (MPPT) algorithm needs to be implemented in a DC/DC stage of the device. Possible topologies include non-isolated converters such as boost, buck, buck-boost or Ćuk topology presented in [1] - [4] and isolated configurations like flyback, push-pull, and resonant converters [5] - [8]. Furthermore, in a MPPT stage soft switching can be achieved and high frequency employed [9].

High frequency resonant converters accommodate great qualities such as improved safety with galvanic isolation, absence of high switching losses thanks to zero current (ZCS) and zero voltage switching (ZVS), along with better power density due to reduced volume of the magnetic components [10] [11].

Numerous resonant tank configurations are possible such as parallel, series or a combination of both resonant phenomenon [12]. The voltage gain of a series resonant configuration (SRC) can take a maximum of 1, while a parallel resonant converter (PRC) can achieve up to 10. Three and four reactive energy storage elements that combine parallel and series resonant phenomenon are more stable for a wide range of loads, and additionally parasitic inductances or capacitances featured in a converter can be employed [13]. Amongst them, LLC is widely used in today's DC/DC converters. Nevertheless, CLLC has its application in bidirectional power conversion systems, while LLC is efficient unidirectional resonant tank that has great efficiency under light load and therefore presents a better option than, for example, LCC for PV microinverter purposes [14].

Resonant converter with LLC tank configuration can be a MPPT stage of a two stage three phase microinverter [15]. The microinverter with galvanic isolation provides improved consumers' safety and can be appropriated for variety of PV systems' realizations [16] - [18]. Additionally, development of a dual input DC/DC converters with LLC resonant tank [19] can be considered because of its abillity to manage wide input voltage rate or it can form a scalable power conversion system as presented in [20].

This paper represents a brief overview of performance of the LLC resonant tank and design of resonant elements for a converter shown at Fig. 1 with 1000 W rated power. Full bridge is considered before resonant tank, while diode rectifier is on transformer's secondary side before DC link.

In the Section II voltage gain and load dependance of the LLC resonant tank is introduced. Following, design procedure of a tank is described with capacitor selection in Section III and inductor design in Section IV. In the last section, experimental results are presented.

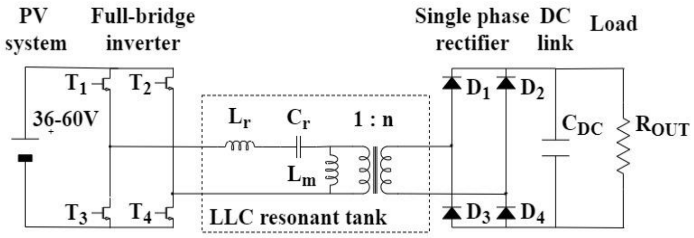

Fig. 1. Resonant LLC topology of a DC/DC converter with a passive load

---

Katarina Obradović is member of Department of Power Converters and Drives, University of Belgrade, 73 Bulevar kralja Aleksandra 73, 11020 Belgrade, Serbia (e-mail: obradovick15@gmail.com).

Emilija Lukić is member of Department of Power Converters and Drives, University of Belgrade, 73 Bulevar kralja Aleksandra 73, 11020 Belgrade, Serbia (e-mail: emilija.lukic505@gmail.com).

Jovana Plavšić is member of Department of Power Converters and Drives, University of Belgrade, 73 Bulevar kralja Aleksandra 73, 11020 Belgrade, Serbia (e-mail: plavsicjovana37@gmail.com).

Aleksandar Milić is with the School of Electrical Engineering, University of Belgrade, 73 Bulevar kralja Aleksandra, 11020 Belgrade, Serbia (e-mail: milic.aleksandar@etf.bg.ac.rs).

II. LLC VOLTAGE GAIN AND LOAD DEPENDENCE

The design of a resonant tank requires input quantities' information including aforementioned rated power with 48 VDC input voltage as well as other parameters listed in Table I. While designing the presented system, the assumption was adopted that the output voltage of the converter will be maintained at a constant value by a proper control system.

Quality factor Q is of a great influence for the analysis of the tank. It represents the change in a converter's voltage gain curve at a different load conditions [21] and is characterized by equation (1)

$$Q = n^2 \cdot \frac{\pi^2}{8} \cdot \frac{P_{out}}{V_{out}^{\;2}} \cdot \sqrt{\frac{L_r}{C_r}} \tag{1}$$

where P_{out} [W] is rated power, V_{out} [V] is an output voltage and n the ratio of secondary and primary number of turns. As it can be seen, Q factor is greater as the load approaches to the nominal value. Additionally, resonant frequency of the LLC resonant tank is described by

$$f_r = \frac{1}{2 \cdot \pi \cdot \sqrt{(L_r + L_m) \cdot C_r}} \tag{2}$$

L_r being series resonant inductor, C_r series resonant capacitor and L_m the magnetizing inductance of the transformer.

Voltage gain of the tank is determined by the ratio of the switching and resonant frequency, load conditions (Q factor) and inductor ratio (m) as can be seen in the following equation

$$M = \frac{1}{\sqrt{\left[1 + \frac{1}{m} - \frac{1}{m} \cdot \left(\frac{f_s}{f_r}\right)^2\right]^2 + Q^2 \cdot \left(\frac{f_s}{f_r} - \frac{f_r}{f_s}\right)^2}} . \tag{3}$$

Inductor ratio m is a constant that defines a ratio of a magnetizing inductance of a transformer L_m and series resonant inductance L_r. Increasing m value, voltage gain characteristics are more flattened thus more stable in wide frequency range, with reduced voltage peak on very light load. This effect can be seen on Fig. 2 where voltage gain characteristics are shown for a number of different Q factors and two different m values – high on the right and low one on the left.

In case m factor is high, LLC resonant tank condenses to a two-element circuit, meaning only L_r and C_r are utilized in a resonant occurrence and current through L_m is reduced. Alternating charging and discharging of the resonant capacitor and inductor leads to a reactive power exchange within these two reactive elements in the circuit which minimizes the apparent power of the tank. With reduced apparent power, the rms value of the current through the series resonant components is lowered and therefore the voltage drops, and Joule's power losses are lessened. High L_m is easily achievable and justified since transformer is there to provide galvanic isolation.

To make sure that larger deviation from the resonant frequency, due to switching frequency change, does not mitigate the voltage gain, the minimum Q factor must be established since that state could jeopardize elements bringing attenuation larger than one as seen in Fig. 2. This is because in case of light load, high values of the equivalent R_{out} could approach to similar value to $X_m = 2 \cdot \pi \cdot f \cdot L_m$ and parallel phenomena comes to the fore. The appropriate minimum Q value for the calculations must be determined knowing the expected load conditions. With all the requirements said, quality factor is taken to be 0.4.

TABLE I
INPUT PARAMETERS FOR THE DESIGN OF REACTIVE ELEMENTS

Parameter	**Symbol**	**Value**
Quality factor	Q	0.4
Turns ratio	n	11
Inductor ratio	m	100
Rated power [W]	P_{out}	1000
Input voltage range [V]	V_{in}	36 - 60
Output voltage [V]	V_{out}	450
Duty cycle	D	0.5

III. CAPACITOR SELECTION

In attempt to achieve high power density it is necessary to minimize volume of resonant elements by operating on high frequencies. However, it should be noted that working with

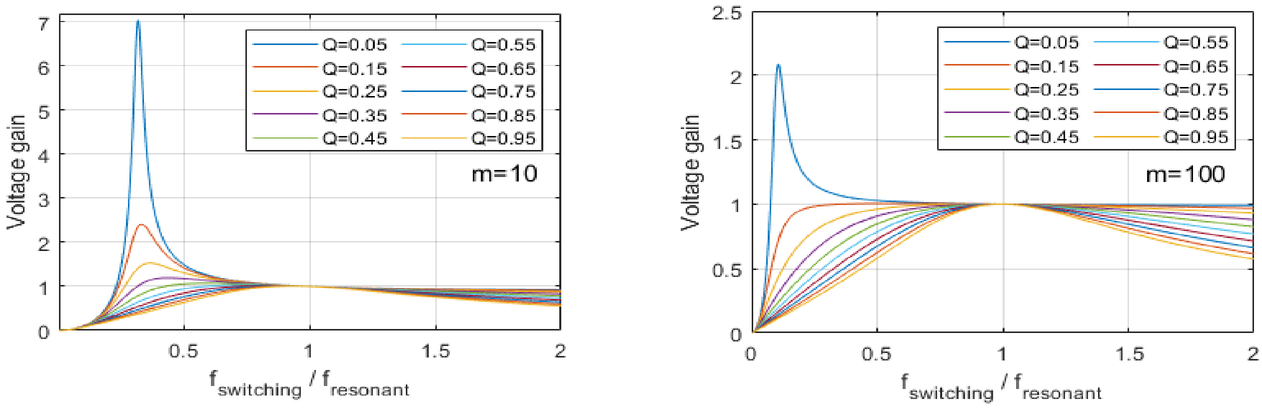

Fig. 2. LLC resonant tank voltage gain dependance on load conditions (Q) and switching frequency for two different values of m – 10 (left) and 100 (right)

too high frequencies brings other problems, for example higher switching losses on semiconductor devices. These losses are significantly lowered in LLC resonant topology due to zero voltage and zero current switching [22].

Values of resonant inductances and capacitance are related through resonant frequency f_r as show in equation (2). Capacitance as a function of frequency for agreed quality factor Q calculated using (1) and (2) is presented on Fig. 3.

An important step in the process of choosing resonant elements is to determinate frequency range in which the value of resonant capacitance stays unchanged. It has been noticed that after 150 kHz the curve portraited in Fig. 3 approximately stays in the flat region. After profound analysis of the transformer's power density, it is established that working with the frequency of 200 kHz with the chosen core material N87, volume of the transformer is sufficiently reduced.

Software simulations in LTspice were conducted applying switching frequency of 200 kHz, nominal input voltage 48 VDC, nominal active power 1 kW, capacitance value determined according to results based on Fig. 3, inductance value calculated by (2) for designated C and input parameters mentioned before. Based on simulation results in rated conditions, resonant current takes absolute value of 24 A.

From the manufacturer's documentation the one can find that an increase in resonant frequency leads to decreases in the maximum rated capacitor voltage as well as maximum rated current. Hence, further frequency rise would result in lowering capacitor's maximum rated current. It means usage of more parallel connected capacitors would be required in order not to pass maximum rated current of a single unit.

Based on the Fig. 3 for the frequency of 200 kHz, needed capacitance equals 1.327 µF. To maintain value of the capacitance for which the resonant current has the minimum value, LTspice simulations were performed. Capacitance value was changed in the range between 1 µF and 2 µF. It was necessary to secure that the current value in that range of capacitances does not fluctuate intensively for the input voltages. Minimum resonant absolute current value was 24 A, achieved in case of the capacitance value of 1.2 µF and inductance of 0.528 µH.

Since inductor will be designed according to the needs and considering the presented evaluation, selection criteria for capacitor are:

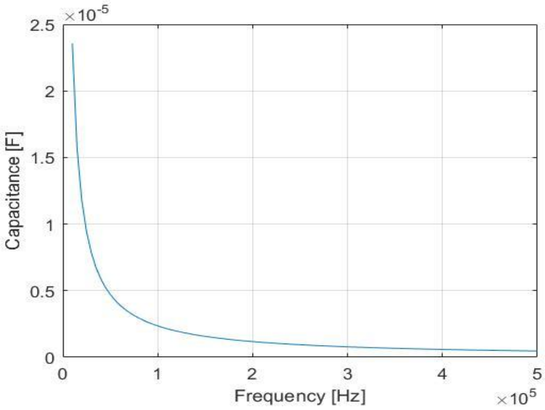

Fig. 3. Value of the resonant capacitance as a function of a resonant switching frequency

- absolute maximum current higher than 24 A on 200 kHz in case of using only one capacitor,
- low equivalent series resistance (ESR),
- capacitance value 1.2 µF,
- flat curve capacitance in a function of frequency,
- flat curve ESR in a function of frequency.

In case capacitor with these parameters is not available, possible solution would be to use more than one, i.e. x units with x times smaller capacitance rated for at least $1/x$ times of the mentioned current. However, suitable component was successfully found, so one unit can be used, and it is KEMET's film capacitor C4BSPBX4120ZB0J.

IV. INDUCTOR DESIGN

After established inductance value of 0.528 µH, resonant inductor can be designed. Transformer's leakage inductance is not taken into consideration as a part of the equivalent inductance since it depends on various factors such as the tightness of the windings and windings' layout. Additionally, it is expected to have very low value.

Knowing the operating frequency, appropriate material can be selected according to manufacturer's suggestion. Inductor core's shape is taken to be E due to simplicity of winding and higher availability on the market. For 200 kHz suggested materials available for E cores are N87, N95 and N97.

A. Determining the core size

Firstly, according to [23], the core's dimensional parameter, S_wS_c, which represents product of the core's cross section (S_c) and the core's window area (S_w), should be above the value calculated using the following formula

$$S_w S_c = \sqrt[7]{\left(\frac{\sqrt{1+k_\gamma} \cdot K_i \cdot L \cdot I_{peak}^2}{B_{\max} \cdot K_t \cdot \sqrt{k_u \cdot \Delta T}} \right)^8} \cdot 10^{12} \qquad (4)$$

where:

- k_γ is the ratio between core and copper losses taken to be 1,
- K_i is the current waveform constant,
- L is the needed inductance value,
- I_{peak} is the maximum current intensity,
- B_{max} is the maximum value of flux density limited by the saturating flux density,
- K_t is the constant suggested by [23] to be 48200 as the core shape is not pot type; considering this constant acknowledges the copper resistivity on 20°C, it should be scaled so that the specific electrical resistivity is the one on 100°C which is $2.3 \cdot 10^{-8}$ Ωm,
- k_u is window utilization factor and
- ΔT is the core temperature rise.

Resulting S_wS_c values for each material are in Table II as well as the values of each listed parameter.

Inductance value for any core can be calculated as:

$$L = A_L \cdot N^2 \qquad (5)$$

where N is the number of turns. After selecting core that has S_wS_c value higher than the one from the Table II, A_L value can be read from the core's datasheet and L calculated using (5).

However, due to high current application, it is very important to take into consideration the fact that the diameter of the conductor will be relatively big. Therefore, prior to selecting the smallest possible core in order to achieve high power density, it is important to check if the window area is large enough for the turns.

B. *Determining the size of the conductor*

Current density should be below 4 A/mm^2 as a good practice, and as suggested by [24]. As current will not exceed 24 A, the diameter of the conductor should be at least 2.8 mm.

Owning to high frequency, it is advisable to use litz wires. This is due to small skin depth of the high frequency current which can be calculated based on the following equation [25]

$$\delta = \sqrt{\frac{\rho_{Cu}}{\pi \cdot f \cdot \mu}} \tag{6}$$

ρ_{Cu} being the specific electrical resistance of the copper, f operating frequency in Hz and μ material's permeability. Based on (6), for 200 kHz the strand of the conductor should be below 292 µm. Due to proximity effect, it appeared that smaller strands result in better efficiency, which has also been a suggestion by litz wires' manufacturer. Finally, based on the market available wires in required quantity, selected conductor has 2800 strands of the diameter 0.072 mm.

Taking the conductor's size into consideration besides the minimum S_wS_c value from the Table II, smallest available core that has large enough window area is the core E 25/13/7. It is produced in materials N87 and N97 and it has approximate A_L value 1850 nH and 1950 nH respectfully. Still, the inductance value computed using (5) even with only one turn is too high. This can be solved by adding a gap to the core.

TABLE II
INPUT PARAMETERS AND NEEDED S_wS_c VALUES

Symbol	**Parameter**	**N97**	**N87**	**N95**
B_{sat}	Saturating flux density [T]	0.41	0.39	0.41
L	Inductance [µH]	0.52		
K_i	RMS and peak current ratio	0.707		
K_t	Core shape constant	41703		
I_{peak}	Current peak value [A]	42.43		
k_u	Window utilization factor	0.8		
ΔT	Temperature rise [°C]	70		
B_{max}	Maximum flux density [T]	0.4	0.38	0.4
S_wS_c	Core size [mm^4]	529.3	561.2	529.3

C. *Determining the gap size*

Inductance of the gapped core can be calculated as

$$L = \frac{N^2}{\frac{1}{\mu_0} \cdot \left(\frac{l_g}{S_c} + \frac{1}{\mu_r} \cdot \frac{l_c - l_g}{S_c} \right)} = \frac{N^2}{\frac{1}{\mu_0 \cdot \mu_{eff}} \cdot \frac{l_c}{S_c}} \tag{7}$$

where l_g [mm] is the gap length, l_c [mm] the length of the flux path corresponding to the chosen core, μ_r is the material's relative permeability, μ_0 [H/mm] magnetic permeability of the air and S_c [mm^2] core's cross section. Thus, adding the air gap μ_{eff} is being shrunk and therefore N has achievable value. Additionally, air gap contributes to stability of the magnetic properties of the core [26].

The core E 25/13/7 in material N97 cannot be gapped by the manufacturer, so the chosen material is N87. The manufacturer has predefined values for air gaps: 0.1 mm, 0.16 mm, 0.25 mm, 0.5 mm, and 1 mm. In Table III it is listed how many turns is needed in case of different gap lengths. Also, the A_L value in case fringing effect is taken into consideration is given by the manufacturer and presented in Table III.

For the 0.5 mm air gap the difference in desirable and resulting A_L and μ_{eff} is the least as seen from Table III. Hence, the chosen core is E 25/13/7 in material N87 with the air gap of 0.5 mm having two turns of litz wire consisting of 2800 strands of the diameter 0.072 mm. Resulting inductance is expected to be 0.5976 µH.

TABLE III
GAPPED E 25/13/7 CORE ANALYSIS

Air gap length [mm]		0.1	0.5	1
Number of turns		1	2	3
Desired μ_{eff} value		462	115	51
Desired A_L value [nH]		530	132.5	58.9
μ_{eff}	No fringing effect	456	109	56
	With fringing effect	422	130	78
A_L [nH]	No fringing effect	523.2	125.4	64.3
	With fringing effect	484.4	149.4	90.0

D. *Finite Elements Method Analysis*

Using software tool FEMM 4.2 finite elements method analysis is conducted. The graphical result is shown in Fig. 4. It should be noted that the flux density in the fringes passes the saturating point.

Inductance value calculated by the software is 0.086 µH. However, this value should be scaled since FEMM 4.2, while calculating equivalent inductance, considers only the part of the turn that is inside the core window. Thus, the value given by the program should be multiplied with the ratio of the turn length in millimeters and doubled core depth, i.e. 14 mm. Corrected value equals to 0.307 µH.

V. EXPERIMENTAL RESULTS

The main intent of testing is to observe the behavior of the resonant topology. Prototype of LLC resonant DC/DC

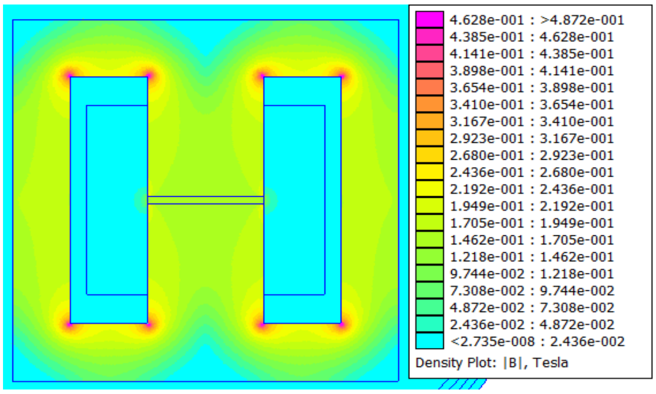

Fig. 4. Flux density in the core done in the software tool FEMM 4.2

converter for 1 kW was developed in Digital Drive Control Laboratory in School of Electrical Engineering, University of Belgrade.

Designed prototype with testing circuit is presented in Fig. 5. Prototype was realized with gallium nitrite transistors as input DC to AC converter in a full bridge configuration using two EPC1022 development boards. However, since these transistors could work with even higher frequencies and remain satisfactorily efficient, it is advisable to, but not limited to, consider them in 500 kHz or higher application. Nevertheless, they can function properly on 200 kHz as well, so they had been taken as a part of the prototype, since accent is on the resonant tank rather than full-bridge parameters.

The measured parameters of the designed and selected resonant tank elements are 0.648 µH for resonant inductance, 49.55 µH for transformer's magnetization inductance, and capacitances of 100 µF and 1.2 µF for DC link and resonant capacitor respectively with load resistance of 650 Ω. Transformer's magnetization inductance, series inductance and capacitance were measured using LRC meter, with 200 kHz excitation signals. For driving transistors in full-bridge configuration, Texas Instruments launch pad 28379D was used employing Power Width Modulation (PWM) signals with adjustable dead time duration. Soft start was necessary to implement in order to avoid unwanted impulsive changes of resonant current. It was realized by phase shift modulation of driving signals. During 3.6 s, one of PWM signal's duty cycle was changed in the range of 0 – 50 %.

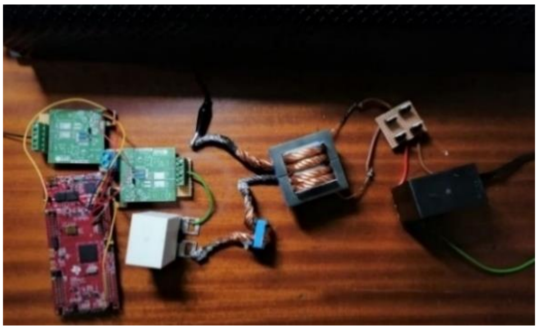

Fig. 5. Experimental setup of LLC resonant DC/DC converter

According to theoretical calculations for resonant tank parameters, switching frequency was set to 200 kHz. The voltage waveforms on primary and secondary transformer side with switching frequency of 200 kHz and 15 VDC at the input converter terminals are shown in Fig. 6. It can be noticed that the transformer's low side voltage is multiplied by the turns' ratio. Also, voltage gain of resonant tank is equal to one, as expected.

Waveform of resonant current is presented in Fig. 7 where input parameters were the same as mentioned before. Based on measurements, resonant inductance takes value of 0.648 µH instead of theoretical 0.528 µH due to imperfections of the inductor's development process. Resonant frequency was now estimated using (2) once again and set to 187 kHz.

Capacitances on the output of the diodes of the rectifier along with output capacitances of the transistors from full-bridge are not being fully discharged during the dead time. As a result, these parasitic capacitances and the circuit inductance had started to resonate, and flinches appeared. In Fig 8. these oscillations on the resonant current waveform can be noticed.

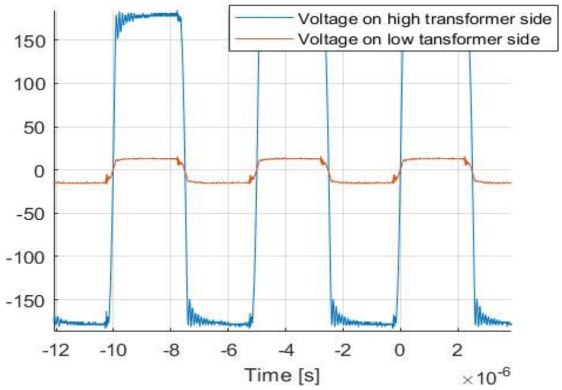

Fig. 6. Voltages on low and high transformer side with 15VDC input voltage and switching frequency of 200kHz.

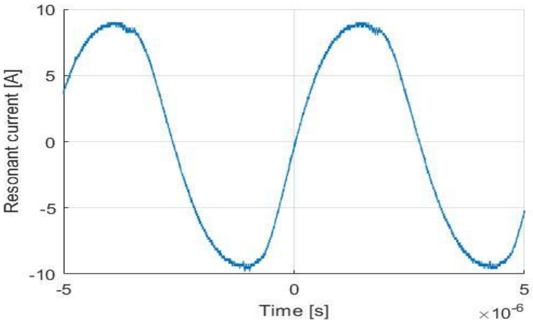

Fig. 7. Waveform of resonant current for 15 VDC input voltage and 200 kHz switching frequency

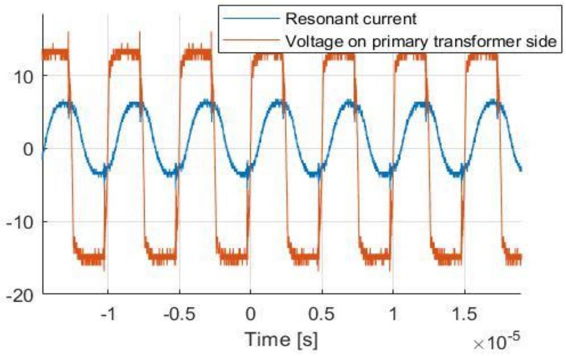

Fig. 8. Waveforms of resonant current and voltage on primary transformer side for 187 kHz as a switching frequency

VI. CONCLUSION

Having the advantage of reduced switching losses due to zero current and zero voltage switching, resonant DC/DC topologies are worth considering in the high frequency high current application in PV inverters. Numerous resonant tank topologies are possible, where LLC is the most common one in the terms of voltage gain stability and design simplicity.

In this paper the process of determining needed series capacitance and inductance's values from LLC resonant tank is presented. Transformer's magnetization inductance has 100 times larger value, so its impact has been neglected.

Thereafter, the procedure of choosing capacitor and inductor design is elaborated in detail.

On the developed prototype, waveforms of relevant variables were observed in a resonant circuit in order to verify the presented design procedure. Experimental tests have shown that the presented method gives satisfactory results in terms of the system's behavior. The resonant LLC converter, in addition to the possibility of working in MPPT mode and galvanic isolation, provides high efficiency and power density, thus reducing the volume and increasing the total efficiency of the conversion system. Due to aforesaid advantages, the presented resonant tank topology is a good choice for the needs of microinverter PV applications.

Further research could take into consideration other core shapes for inductor, include transformer's leakage inductance into calculations, as well as the analysis of higher working frequencies suitable for wide-bandgap devices.

ACKNOWLEDGMENT

We would like to express special gratitude to Efficient Power Conversion (EPC) company. Their generous donation of EPC1022 development boards has helped us to undertake this project and present experimental research that we have accomplished in the Laboratory.

REFERENCES

[1] R. W. Erickson, D. Maksimović in "Principles of Steady State Converter Analysis" *Fundamentals of Power Electronics*, New York, United States of America: Soringer, 2001, ch. 2, sec 3. pp. 22-27

[2] R. W. Erickson, D. Maksimović in "Steady-State Equivalent Circuit Modeling, Losses, and Efficiency" *Fundamentals of Power Electronics*, New York, United States of America: Soringer, 2001, ch. 3, sec 4. pp. 50-52

[3] S. N. Soheli, G. Sarowar, M. A. Hoque and M. S. Hasan, "Design and Analysis of a DC -DC Buck Boost Converter to Achieve High Efficiency and Low Voltage Gain by using Buck Boost Topology into Buck Topology," *2018 International Conference on Advancement in Electrical and Electronic Engineering (ICAEEE)*, 2018, pp. 1-4

[4] S. Cuk, R. D. Middlebrook, "A new optimum topology switching DC-to-DC converter" in *IEEE Power Electronics Specialist Conference*, Palo Altro, CA., USA, 1977.

[5] Y. Konishi, Y.-F. Huang, M.-J. Hseih, "Utility-interactive high-frequency flyback transformer link three-phase inverter fir photovoltaic AC module" in *35th Annual Conference of IEEE Industrial Electronics*, Porto, Portugal, 2009.

[6] Z. Chen, Q. Wu and Y. Yuan, "A Novel Zero-Voltage-Switching Push–Pull High-Frequency-Link Single-Phase Inverter," in *IEEE Journal of Emerging and Selected Topics in Power Electronics*, vol. 4, no. 2, pp. 421-434, June 2016.

[7] A. Hillers, D. Christen and J. Biela, "Design of a Highly efficient bidirectional isolated LLC resonant converter," 2012 15th International Power Electronics and Motion Control Conference (EPE/PEMC*)*, 2012.

[8] K. Siebke and R. Mallwitz, "Operation Mode Analysis of the CLLC Resonant Converter," *2019 IEEE 13th International Conference on Compatibility, Power Electronics and Power Engineering (CPE-POWERENG)*, 2019, pp. 1-6

[9] Y. Zhuang, F. Liu, X. Zyang, X. Diao, J. Jiang and J. Sun, "Direct Frequency Control Based MPPT Algorithm of LLC Resonant Converter for Photovoltaic System" in *2019 IEEE Energy Conversion Congress and Exposition (ECCE)*, Baltimore, Maryland, USA, 2019.

[10] Hillers, A., Christen, D., & Biela, J. (2012). *Design of a Highly efficient bidirectional isolated LLC resonant converter. 2012 15th International Power Electronics and Motion Control Conference (EPE/PEMC)*, 2012.

[11] F. Musavi, M. Craciun, M. Edington, W. Eberle, and W. G. Dunford, "Practical design considerations for a LLC multi-resonant DC-DC converter in battery charging applications," in Proc. 27th Annu IEEE APEC Expo., 2012, pp. 2596–2602

[12] R. L. Steigerwald, "A comparison of half-bridge resonant converter topologies," in *IEEE Transactions on Power Electronics*, vol. 3, no. 2, pp. 174-182, April 1988.

[13] R. Severns, "Topologies for three element resonant converters," Fifth Annual Proceedings on Applied Power Electronics Conference and Exposition, 1990, pp. 712-722

[14] S. Mao, J. Popovic, R. Ramabhadran and J. A. Ferreira, "Comparative study of half-bridge LCC and LLC resonant DC-DC converters for ultra-wide output power range applications" *2015 17th European Conference on Power Electronics and Applications (EPE'15 ECCE-Europe)*, 2015, pp. 1-10

[15] Alamir, O. Abdel-Rahim, M. Orabi and M. Ismeil, "Two-Stage Resonant Three-Phase Micro-inverter for Grid-Tie PV Application," *2019 IEEE Conference on Power Electronics and Renewable Energy (CPERE)*, 2019, pp. 459-464

[16] G. Rubino, L. Rubino, N. Serbia, P. Ladoux and P. Marino, "LLC resonant converters in PV applications comparison of topologies considering the transformer design," *2013 International Conference on Clean Electrical Power (ICCEP)*, 2013, pp. 37-41

[17] C. Buccella, C. Cecati, H. Latafat and K. Razi, "A grid-connected PV system with LLC resonant DC-DC converter," *2013 International Conference on Clean Electrical Power (ICCEP)*, 2013, pp. 777-782

[18] A. Bousselham and A. Elrayyah, "Control and efficient operation of low cost multi PV-based LLC resonant microinverters," *2016 IEEE 43rd Photovoltaic Specialists Conference (PVSC)*, 2016, pp. 3457-3462

[19] S. M. Tayebi, H. Hu, O. Abdel-Rahman and I. Batarseh, "Design and analysis of a dual-input single-resonant tank LLC converter for PV applications," *2018 IEEE Applied Power Electronics Conference and Exposition (APEC)*, 2018, pp. 476-483

[20] C. Schaef and J. T. Stauth, "Multilevel Power Point Tracking for Partial Power Processing Photovoltaic Converters," in *IEEE Journal of Emerging and Selected Topics in Power Electronics*, Dec. 2014, vol. 2, no. 4, pp. 859-869

[21] G. Hsieh, C. Tsai and S. Hsieh, "Design Considerations for LLC Series-Resonant Converter in Two-Resonant Regions," *2007 IEEE Power Electronics Specialists Conference*, 2007, pp. 731-736

[22] X. Zhou, Z. Liang and A. Huang, "A High-Dynamic Range Current Source Gate Driver for Switching-Loss Reduction of High-Side Switch in Buck Converter," in IEEE Transactions on Power Electronics, June 2010. vol. 25, no. 6, pp. 1439-1443

[23] W. G. Hurley, W. H. Wölfle, "Inductor Design," in *Transformers and Inductors for Power Electronics,* Chichester, United Kingdom: John Wiley & Sons Ltd., 2013, ch. *3*, sec. *1-2*, pp. *61-64*

[24] A. I. Pressman, K. Billings, T. Morey, "Transformers and Magnetics Design," in Switching Power Supply (3th Edtion), New York, United States of America: McGraw Hill Education, 2013, ch. *7*, sec. 3, p. *313*.

[25] A. V. Bossche, V. C. Valchev, "Soft Magnetic Materials" in *Inductors and Transformers for Power Electronics,* Boca Raton, United States of America: CRC Press Taylor & Francis Group, 2005, ch. *3*, sec. *3*, pp. *136–137*

[26] W. G. Hurley, W. H. Wölfle, "Inductance," in *Transformers and Inductors for Power Electronics,* Chichester, United Kingdom: John Wiley & Sons Ltd., 2013, ch. *2*, sec. *1*, pp. *25–38*

Implementation and testing of basic algorithms in PV systems with batteries on a common DC link

Katarina Ćeranić, Mila Gligorijević, Lazar Stojanović and Aleksandar Milić

***Abstract*—Photo-voltaic systems with batteries on a common DC link, i.e. the concept of the Point of Common Coupling (PCC), is increasingly in use. In such systems, it is necessary to achieve the basic system functionalities, such as bidirectional battery operation, efficient Maximum Power Point Tracking (MPPT) regimes on the PV panels, as well as constant voltage on the common DC link for the consumer needs. In this paper, the basic algorithms for battery and panel operation in the MPPT mode are provided. The analysis was first verified in software packages and later by implementing algorithms on the developed low-power prototype of the system, where the basic functionalities were presented. Additionally, the robustness of the algorithms to power transients and disturbances which are common in the PCC systems was tested.**

***Index Terms*—DC link, Point of Common Coupling, battery, MPPT, battery charging strategy.**

I. INTRODUCTION

One of the leading causes of global warming is production of the electrical energy. Commonly used energy sources are non-renewable, such as coal, oil and natural gas, where their usage directly results in the pollution of air, water and land. In the past few decades, the use of renewable energy sources, especially wind and solar power, has become more common [1][2]. Further, a stand-alone PV system whose application context is specific to the countryside or isolated locations for self-feeding, is seen as a substitute for the utility grid connection [3]. In such applications, photo-voltaic systems (PV) almost always imply the use of batteries in their continuous operation. Namely, this application enables the consumer to be independent from the electrical grid, as well as, to simultaneously act as a consumer and a producer of electrical energy. Thus, there is a need for a scaled down energy storage system which interacts with the clean energy source.

The main disadvantage of PV panel employment is the fluctuating output power induced by the variable solar irradiance. This introduces difficulty into fully capitalizing on the panel production, hence creating a need for a control algorithm which would track the maximum power point – MPPT algorithm [4], such as Perturb and Observe (P&O), Incremental Conductance (IC), Current Sweep (CS) technique [5][6], or Open Circuit Voltage (OCV) technique [7][8], along with the Particle Swarm Optimisation (PSO) based algorithms [9]. The main goal of these algorithms is circumventing the practical issues which arise with the PV panel implementation - variable irradiance or damaged cells. Comparison of these algorithms has shown that each has its advantages and disadvantages – where P&O and IC implementation is straightforward, their robustness to disturbance is not a strong point. These two algorithms are also incapable of locating the global maximum on the P-V curve, which usually occurs when the PV string has multiple bypass diodes i.e. multiple power peaks. PSO, in particular, has found its implementation in large string operations, where multiple bypass diodes are unavoidable. However, more advanced algorithms, PSO and CS, are much more complex with their benefits being insignificantly greater than those of P&O and IC in terms of microcontroller implementation. The main shortcoming of the VOC technique is the fact that it requires the power delivery to be halted every time the open circuit voltage of the PV string is needed for further calculation.

Although the development of MPPT algorithms as well as controlled battery charging and discharging algorithms have progressed, there are applications where basic algorithms, reliably implemented, can achieve acceptable results. There, fast high-performance processors are redundant and, thus, avoided, which immediately reduces the overall cost of the product. For this reason, this paper deals with the implementation and testing of basic algorithms in the system presented in Fig. 1, which contains PV panels and a battery connected to a common point. The paper is organized as follows – in Section II an overview of the analyzed system is presented, section III provides basic analysis of the implemented control algorithms. Further, the results of the comparison of the applied algorithms obtained in the simulations and in the experimental setup are presented in Sections IV and V, respectively. Finally, a brief conclusion of the comparison is given.

Katarina Ćeranić is a student at Power Converters and Drives Department, University of Belgrade, 73 Bulevar kralja Aleksandra, 11020 Belgrade, Serbia (e-mail: ceranic.katarina@gmail.com).

Mila Gligorijević is a student at Power Converters and Drives Department, University of Belgrade, 73 Bulevar kralja Aleksandra, 11020 Belgrade, Serbia (e-mail: mila.gligorijevic7@gmail.com).

Lazar Stojanović is a student at Signals and Systems Department, University of Belgrade, 73 Bulevar kralja Aleksandra, 11020 Belgrade, Serbia (e-mail: lazastojanovic99@gmail.com).

Aleksandar Milić is with the School of Electrical Engineering, University of Belgrade, 73 Bulevar kralja Aleksandra, 11020 Belgrade, Serbia (e-mail: milic.aleksandar@etf.bg.ac.rs).

II. SYSTEM OVERVIEW

The system, on which the control has been implemented, falls in line with the streamlined topology – it is composed of a buck converter as the input stage and a four-switch synchronous buck-boost converter connected to the battery [10]. The point of common coupling (PCC) for these two converters is the DC link, which is also the connection point for the consumer. The prototype parameters are provided in Tables I and II, and the entire power stage schematic is shown in Fig. 1.

TABLE I
SYSTEM PARAMETERS

	L[μH]	C[μF]	$R_{DSon}[\Omega]$
Buck	11.3	22	0.01
Buck-Boost	4.7	100	0.008
DC Link	/	450	/

TABLE II
PV PANEL PARAMETERS

V_{OC}[V]	I_{SC}[A]	V_{MPP}[V]	I_{MPP}[A]
21.9	1.84	17.6	1.7

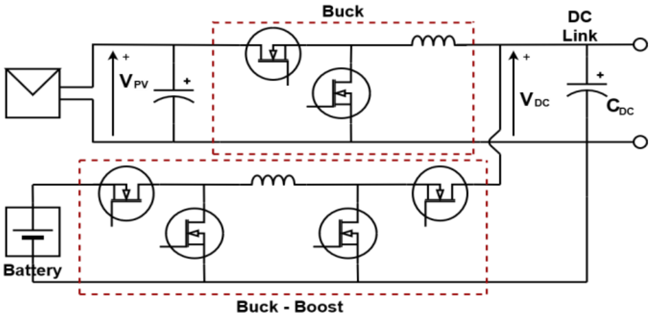

Fig 1. System overview

The hardware design which is increasingly represented in the industry comprises of an input stage communicating with the PV panels and a battery power stage where the common point is the DC link. The DC link voltage is kept consistently within the desired margins, either by generating the power from the PV panels or by discharging the battery [11]. Li-ion battery cells have become the mainstream portable power source due to their exceptional characteristics, such as high specific power density, high cell voltage, low self-discharging rate, high charging current and long life cycle [12]. Hereof, the developed prototype, which will be discussed in more detail in Section V, uses two identical Li-ion batteries connected in series and PV panels whose characteristics are shown in Fig. 2.

In general applications pertaining to higher power derivation, the input step would have been a boost converter, due to its continuous input current [13]. This paper is considering low-voltage low-power applications, so a buck converter as the input stage was chosen, despite the discontinuous input current, which ought to render the MPPT mode inoperable. The desired MPPT operation regime is feasible if a capacitor is connected in parallel to the panels, as it enables the continuous power necessary for the MPPT algorithms. Thus, the input buck converter lowers the panel voltage to the DC link voltage and the MPPT algorithm governs the duty cycles of the input buck. The battery buck-boost keeps the DC link voltage constant and charges or discharges the battery in accordance with the system state [10].

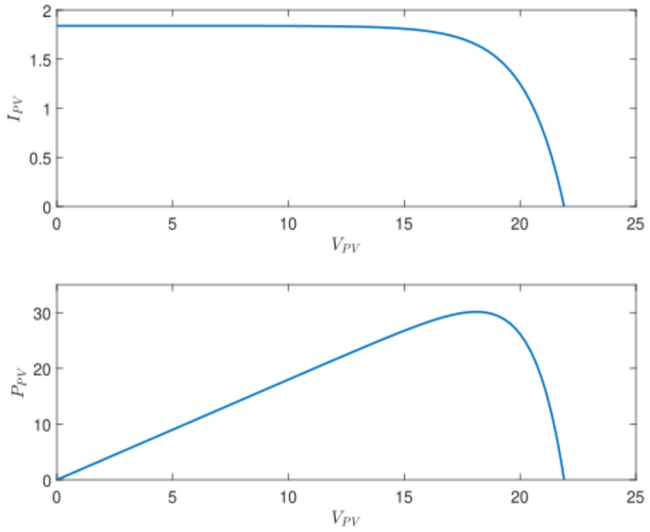

Fig. 2. Current to Voltage and Power to Voltage Characteristics

Various converters which allow the battery management i.e. bidirectional power flow have been devised. Some of them are: buck-boost, SEPIC, Cuk, synchronous four-switch buck-boost and multi-level bidirectional converters [14]. The chosen converter here is the synchronous four-switch buck-boost due to its ease of implementation.

III. ANALYSIS OF CONTROL ALGORITHMS

A. *MPPT algorithms analysis*

In this Section, the two employed MPPT algorithms are the "hill climbing" algorithms P&O and IC – shown in Fig. 4 and Fig. 5. P-V characteristics of the panels, which are used in both algorithm designs, are shown in Fig. 2. These two algorithms have been chosen for their ease of implementation and low computational power they expend. P&O and IC both slide the operating point along the P-V characteristic of the panels so that the string produces the maximum power available at any given point in time [15]. When using P&O, the controller incrementally adjusts the harvested power by measuring the panel voltage and panel current, and then either takes a step forward or backward along the P-V curve depending on the needs of the system, as shown in Fig. 3. The main issue with this method is that even when the input power is stable, the derived power oscillates in the vicinity of the MPP.

IC does not produce output power oscillations. It relies on the slope of the P-V curve and, as such, upon reaching the MPP, remains there due to zero inclination. The controller maintains these working states until the irradiation changes.

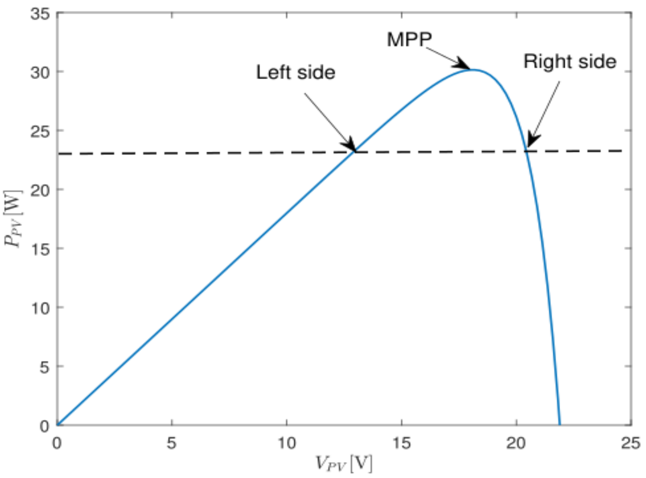

Fig 3. P-V operating point positions

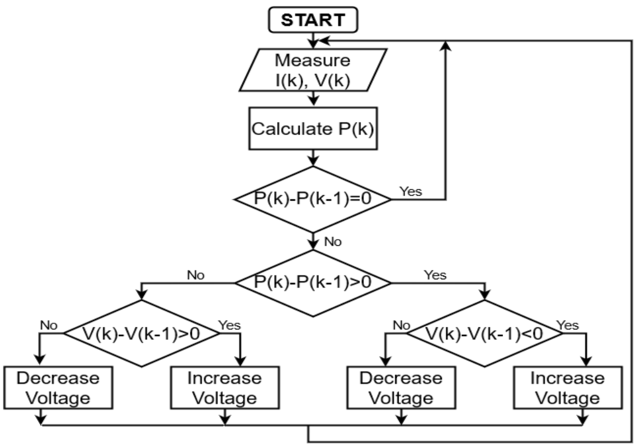

Fig 4. Perturb and Observe Algorithm

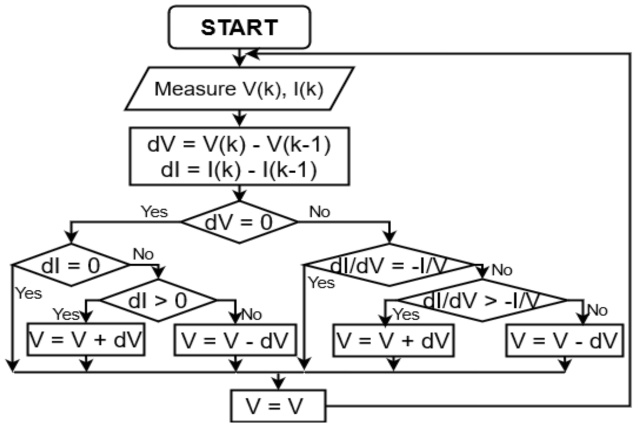

Fig 5. Incremental Conductance Algorithm

B. *Battery charging*

Another topic of importance is the battery charging strategy. In order to charge, the battery needs to be connected to a power supply. This triggers an oxido-reduction reaction – oxidation occurs on the positive electrode, the one releasing electrons, while reduction manifests on the negative, attracting the released electrons and charging the battery. Discharge happens when the battery is connected to a load – the process of discharging is directly opposite to charging [16]. The battery charging process is done by a combination of Constant Current (CC), typically no greater than 1C or 2C, and Constant Voltage (CV) operating modes, as show in Fig. 6 [12].

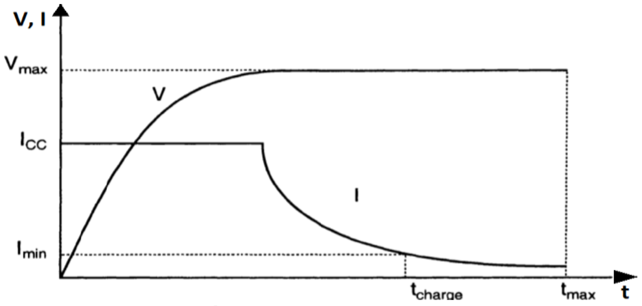

Fig 6. CC-CV Battery Charging

In practice, the values of voltage and charging current are dictated so as to preserve the cell lifespans – high values of maximum voltage and their application for extended periods of time should be avoided [17][18]. Since the prototype operates with the above-mentioned batteries, which are Li-ion based, the best charging method is Constant Current – Constant Voltage (CC-CV). Constant Current (CC) entails charging with a constant current value. This is maintained until the battery reaches the designated voltage value. So as to not overcharge the battery, the voltage value at which CC is stopped has to be less than 100% - usually the cut-off voltage is around 80-90%. In the developed prototype, the charge rate is limited to 1C. This process is then followed by Constant Voltage (CV) charging mode – it charges the battery to full capacity while the current exponentially reduces.

C. *CC-CV and the stability of operating points*

The CC-CV method charges a battery with a constant current until the battery voltage increases to the constant voltage limit. Then the voltage is kept at said limit while the charging current gradually decreases. In the CC-CV charging method, the CV regime typically lasts longer, prolonging the total charging time [19]. By employing the optimal constant values of current and voltage for the used battery, one is able to achieve the most efficient battery charging process.

Another important operational mode pertains to the situation where the load power consumption is low and the battery is already full. Therefore, it is necessary to move from the MPP in order to not overcharge the battery or jeopardize the DC link voltage. Assuming that the eventual load and the battery combined are able to consume less power than what the panel can generate, in these cases, it is necessary to move the operating point to the part of the curve where less power is generated. This is done by controlling the input power via the input buck converter and is the main idea behind the CC-CV algorithm implemented in this paper.

Bearing in mind the topology of the panel converter, the peak in power production is going to firstly be reflected in the DC link voltage V_{DC} – which is going to start increasing. Each power demand corresponds to two operating points – one to the left of the MPP, and another one to the right, refer to Fig. 3. The criteria for the operating mode choice is the system stability, which is ascertained through a system model. Assuming that the converter is in equilibrium, the operating point is tested to small perturbation. In (1) and (2) U_{CDC} represents the DC link capacitor energy. P_{PV} is the panel power and P_0 is the sum of all losses, load and battery consumption. The equation (3) is valid due to the nature of the converter – here, D refers to the duty cycle.

$$\frac{dU_{C_{DC}}}{dt} = P_{PV} - P_0 \tag{1}$$

$$U_{C_{DC}} = \frac{C_{DC}\cdot V_{DC}{}^2}{2} \tag{2}$$

$$V_{PV} = \frac{V_{DC}}{D} \tag{3}$$

Combining equations (3) and (2) and inserting that into (1) results in the following model:

$$\dot{V}_{PV} = \frac{1}{C_{DC}\cdot D^2 \cdot V_{PV}}\cdot (P_{PV} - P_0) \tag{4}$$

$$V_{PV} = f(V_{PV}) \tag{5}$$

To apply indirect Lyapunov method [20], the model (4) has to be linearized first:

$$\frac{\partial \dot{V}_{PV}}{\partial V_{PV}} = \frac{1}{C_{DC}\cdot D^2}\cdot\left(\frac{\partial P_{PV}}{\partial V_{PV}}\cdot\frac{1}{V_{PV}} - \frac{P_{PV}-P_0}{V_{PV}{}^2}\right) \tag{6}$$

In order for the equilibrium point $P_{PV}=P_0$ to be stable:

$$\frac{1}{C_{DC}\cdot D^2}\cdot\frac{\partial P_{PV}}{\partial V_{PV}}\cdot\frac{1}{V_{PV}} < 0. \tag{7}$$

Since $C_{DC}>0$, $V_{PV}>0$, (7) is equal to:

$$\frac{\partial P_{PV}}{\partial V_{PV}} < 0 \tag{8}$$

This is true only for the part of the P-V curve that is on the right side of the MPP, as seen in Fig. 3. A detailed overview of the employed CC-CV algorithm is provided in Fig. 7.

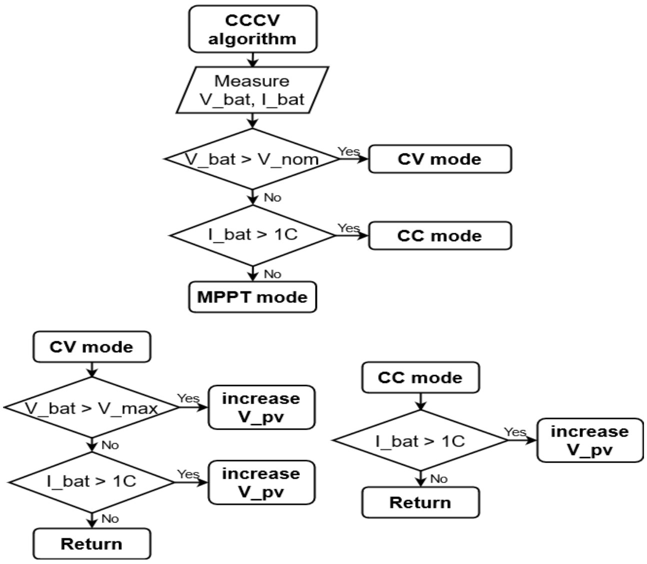

Fig. 7. CC-CV algorithm

IV. SIMULATION RESULTS

For the purpose of this paper, the analyzed system presented in Fig. 1 was simulated in a MATLAB - Simulink software package. In the simulations, it was adopted that the maximum output power of the system is 80 W, which corresponds to the developed prototype of the system. This is going to be discussed in more detail in the next chapter. The simulation conditions include irradiance which changes throughout the duration of the simulation and a load that can be optionally connected or disconnected. The MPPT algorithm adapting to variable irradiance is shown in Fig. 8. During the test, it was adopted that there is a consumer of constant power on the common DC link, which is at constant voltage. For this reason, from the presented results, one can identify a change in battery current depending on the power delivered from the panels. That is, depending on the generated power, the battery switches from the discharge mode into charging mode and vice versa. Also, it can be concluded that the implemented algorithm has a fast response with no switching upon varying the input irradiance.

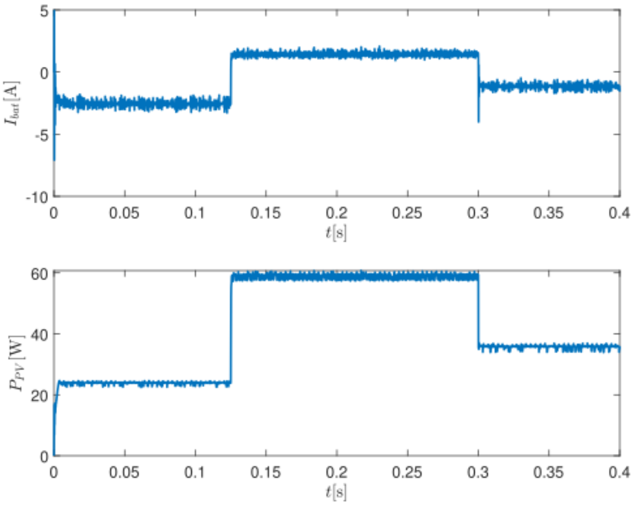

Fig. 8. MPPT mode with variable irradiance

Further, Fig. 9 depicts the battery charging current and the power derived from the panels when the load is suddenly disconnected during the CC charging mode. The current peaks, at the moment of disconnection, however, the controller quickly limits it to the maximum allowed value. The derived panel power is appropriately lowered, showcasing the controller's ability to adapt to disturbances. However, oscillations can be observed in the generated power of the panel, which in this mode, is delivered directly to the battery.

Similarly, the controller adjusts to the load disconnection during CV mode - Fig 10. The battery voltage is swiftly returned to the designated voltage value and the power is correspondingly reduced which is achieved by changing the active pulse width when controlling the switches on the panel converter. Similar oscillations can be observed in the output power of the panel as in the previous test.

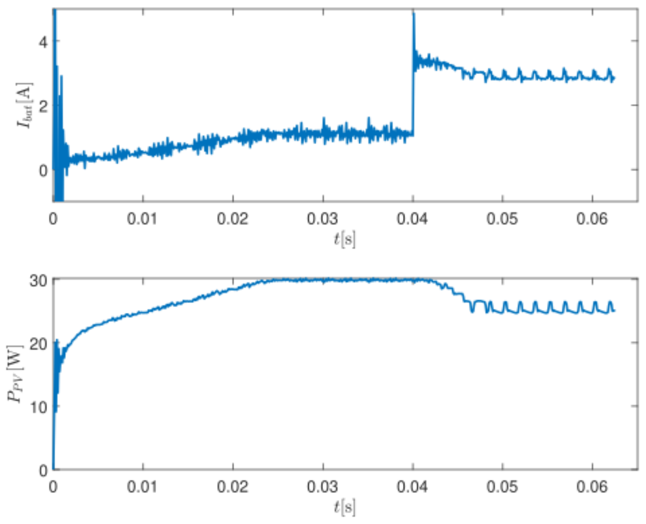

Fig. 9. CC mode with sudden load disconnection

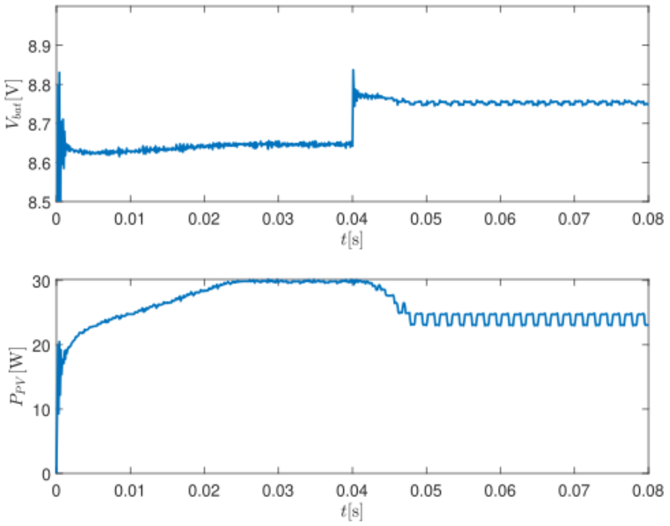

Fig. 10. CV mode with sudden load disconnection

V. EXPERIMENTAL RESULTS

For the required testing of the presented algorithms in actual working conditions, a prototype of the analyzed system was developed in the Digital Drive Laboratory, University of Belgrade. The experimental setup and the prototype can be seen in Fig. 11 and Fig. 12, respectively. The setup consists of two PV panels mounted on the wall. Four halogen lights supplied through two autotransformers simulate variable irradiation. The setup also includes the prototype, an oscilloscope and current probe monitoring the battery current. A resistive load is connected to the DC link. The presented algorithms were implemented on a low-power STM32l4r5qi processor with a code execution time of 10 µs.

Regarding the MPPT stage, tests of the two presented algorithms were performed. The results are presented in Fig. 13, where the MPPT rise time can be observed to be around 180 ms, as well as the power oscillation when the MPP is located. Theoretically, IC is supposed to be more stable once in the MPP, however, in this application, IC operates less effectively due to the induced noise on the prototype.

Fig. 11. Testing experimental setup

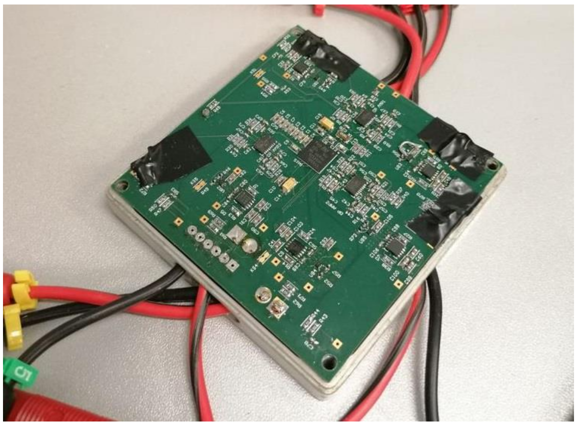

Fig. 12. Developed prototype

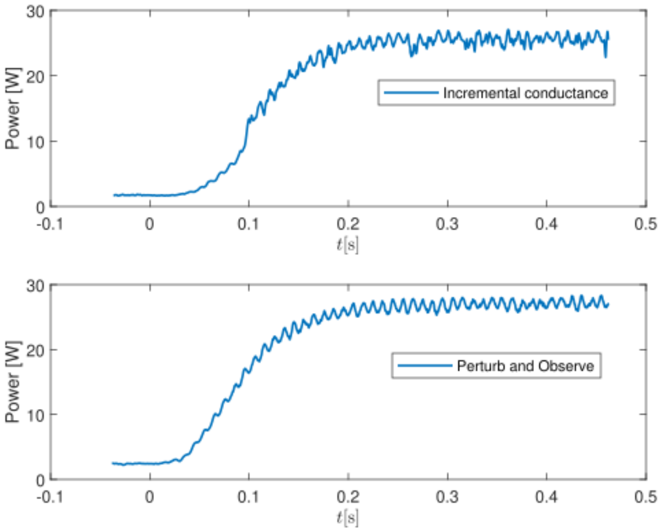

Fig. 13. MPPT methods comparison

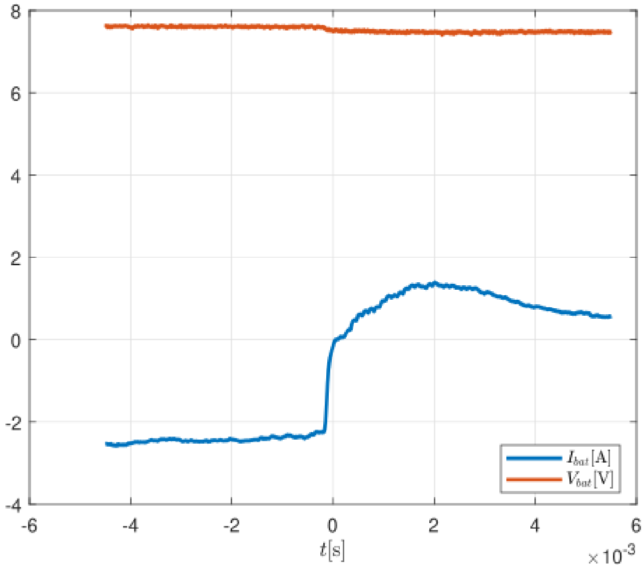

Fig. 14. Transition from charge to discharge

As for the battery, Fig. 14 shows the transition between charging and discharging modes as well as the DC link voltage. From the presented results, it can be concluded that the DC link voltage does not experience too many disturbances during this transient. This is achieved by an external voltage control loop of the converter on a battery that maintains the DC link voltage at a constant value of 7.8 V. An internal current control loop maintains the battery charging and discharging current. The switching frequency of 300 kHz has resulted in the low values of the charge and discharge current ripple. Also, it can be seen that both battery modes are successfully achieved – charging when the current takes a positive value and discharging when the current becomes negative. Insufficient input power is simulated by lowering the irradiance, which results in triggering the change from charge to discharge.

VI. CONCLUSION

This paper presents a simple design of an algorithm for controlling a low-power PV system supported by batteries. The logistics of the algorithms that are often encountered in practice are presented as they have been implemented on the developed prototype of the system. The simulation results were expanded upon by the experimental results. Furthermore, the three basic system requirements were met, bidirectional battery operation, panel operation in the MPPT mode as well as constant DC link voltage for the needs of powering an arbitrary consumer. The presented algorithms are quickly and easily implemented on low-power and low-cost processors. Of course, the presented solution has an extensive space for improvement when considering system performance, algorithm execution speed as well as robustness to disturbances.

REFERENCES

[1] S. Krauter, "Greenhouse gas reduction by PV," 3rd World Conference onPhotovoltaic Energy Conversion, 2003. Proceedings of, 2003, pp. 2610-2613 Vol.3

[2] Contribution of Working Group III to the Fourth Assessment Report of the Intergovernmental Panel on Climate Change [B. Metz, O.R. Davidson, P.R. Bosch, R. Dave, L.A. Meyer (eds)], Cambridge University Press, Cambridge, United Kingdom and New York, NY, USA

[3] F. Locment, M. Sechilariu and I. Houssamo, "Batteries and DC charge control of stand-alone photovoltaic system. Experimental validation," Proceedings of 14th International Power Electronics and Motion Control Conference EPE-PEMC 2010, 2010, pp. T12-43-T12-48

[4] Patil S.N. and R. C. Prasad, "Design and development of MPPT algorithm for high efficient DC-DC converter for solar energy system connected to grid," 2015 International Conference on Energy Systems and Applications, 2015, pp. 228-233

[5] T. Esram and P. L. Chapman, "Comparison of Photovoltaic Array Maximum Power Point Tracking Techniques," in IEEE Transactions on Energy Conversion, vol. 22, no. 2, pp. 439-449, June 2007

[6] Bodur, Mehmet; Ermis, M. (1994). "Maximum power point tracking for low power photovoltaic solar panels". Proceedings of the 7th Mediterranean Electrotechnical Conference: 758–761

[7] Ferdous, S.M.; Mohammad, Mahir Asif; Nasrullah, Farhan; Saleque, Ahmed Mortuza; Muttalib, A.Z.M.Shahriar (2012). 2012 7th International Conference on Electrical and Computer Engineering. ieee.org. pp. 908–911

[8] Hlaili, M., \& Mechergui, H. (2016). Comparison of Different MPPT Algorithms with a Proposed One Using a Power Estimator for Grid Connected PV Systems. International Journal of Photoenergy, 2016, 1–10

[9] Y. Liu, D. Xia and Z. He, "MPPT of a PV system based on the particle swarm optimization," 2011 4th International Conference on Electric Utility Deregulation and Restructuring and Power Technologies (DRPT), 2011, pp. 1094-1096

[10] M. Orellana, S. Petibon, B. Estibals and C. Alonso, "Four Switch Buck-Boost Converter for Photovoltaic DC-DC power applications," IECON 2010 - 36th Annual Conference on IEEE Industrial Electronics Society, 2010, pp. 469-474

[11] H. Soleimani, A. Dastfan and A. Hajizade, "DC bus voltage control by using a multi input/output system of photovoltaic/battery," 2012 IEEE International Conference on Power Electronics, Drives and Energy Systems (PEDES), 2012, pp. 1-5

[12] H. J. Bergveld, W. S. Kruijt, and P. H. L. Notten, “Basic information on batteries,” in Battery Management Systems Design by Modelling, Kluwer Academic Publishers, 2002, vol. 1, pp. 31–53

[13] R. W. Erickson and D. Maksimovic, Fundamentals of Power Electronics, Nowell, MA: Kluwer, 2001

[14] Slobodan N. Vukosavić, Grid-Side Converters Control and Design, Springer International Publishing, 2018

[15] A. S. Ahmed, B. A. Abdullah and W. G. A. Abdelaal, "MPPT algorithms: Performance and evaluation," 2016 11th International Conference on Computer Engineering & Systems (ICCES), 2016, pp. 461-467

[16] Y. -s. Bai and C. -n. Zhang, "Experiments study on fast charge technology for Lithium-ion electric vehicle batteries," 2014 IEEE Conference and Expo Transportation Electrification Asia-Pacific (ITEC Asia-Pacific), 2014, pp. 1-6

[17] C. Lin, C. Hsieh and K. Chen, "A Li-Ion Battery Charger With Smooth Control Circuit and Built-In Resistance Compensator for Achieving Stable and Fast Charging," in IEEE Transactions on Circuits and Systems I: Regular Papers, vol. 57, no. 2, pp. 506-517, Feb. 2010

[18] M. Chen and G. Rincon-Mora, “Accurate, compact, and power-efficient Li-ion battery charger circuit,” IEEE Trans. Circuits Syst. II, Exp. Briefs, vol. 53, no. 11, pp. 1180–1184, Nov. 2006

[19] Y.-H. Liu, J.-H. Teng, and Y.-C. Lin, “Search for an optimal rapid charging pattern for lithium-ion batteries using ant colony system algorithm,” IEEE Trans. Ind. Electron., vol. 52, no. 5, pp. 1328–1336, Oct. 2005

[20] M. Vidyasagar, Nonlinear Systems Analysis, Society for Industrial and Applied Mathematics, 2002